GEORG-AUGUST-UNIVERSITÄT
GÖTTINGEN

Fakultät für
Physik

Master's Thesis

Studien zu theoretischen Unsicherheiten in einer Top-Quark-Zerfallsbreitenmessung mit Hilfe von Ereignisgeneratoren nächstführender Ordnung

Studies of Theoretical Uncertainties for the Measurement of the Top-Quark Width using Next-to-leading-Order (NLO) Generators

prepared by

Marcel Niemeyer

from Lingen

at the II. Physikalischen Institut

Thesis number:	II.Physik-UniGö-MSc-2018/03
Thesis period:	4th September 2017 until 3rd September 2018
First referee:	Prof. Dr. Arnulf Quadt
Second referee:	Prof. Dr. Stan Lai

Zusammenfassung

In dieser Arbeit werden Schritte zur Validierung und des Tunings des $b\bar{b}4\ell$ Monte-Carlo-Ereignisgenerators innerhalb des ATLAS-Frameworks vorgestellt. $b\bar{b}4\ell$ ist ein neuartiger Generator, der Ereignisse mit einem $\ell^+ \nu_\ell l^- \bar{\nu}_l b\bar{b}$-Endzustand unter Berücksichtigung aller möglichen Feynman-Diagramme in nächstführender Ordnung der QCD generiert. Zum ersten Mal sind in ihm exakte Spin-Korrelationen, $t\bar{t}$-Off-Shell-Effekte und tW-Interferenz-Effekte implementiert. Aus diesen Gründen bietet $b\bar{b}4\ell$ die genauesten theoretischen Vorhersagen dieses Prozesses, die aktuell verfügbar sind, was die Validierung des Generators für die Nutzung in ATLAS unverzichtbar macht.

Außerdem wird der Einfluss des Generators auf ausgewählte Messungen diskutiert, namentlich eine direkte Messung der Top-Quark-Zerfallsbreite, eine Messung der Spin-Korrelationen und einer Single-Top-Quark-Messung im Interferenzbereich von $t\bar{t}$ und tW.

Stichwörter: NLO Ereignisgenerator, $b\bar{b}4\ell$, Top-Quark, Top-Breite

Abstract

In this thesis, the validation and tuning of the $b\bar{b}4\ell$ Monte Carlo generator in the ATLAS framework will be presented. $b\bar{b}4\ell$ is a novel generator that produces events with an $\ell^+ \nu_\ell l^- \bar{\nu}_l b\bar{b}$ final state, incorporating all possible Feynman diagrams at NLO QCD. It implements for the first time exact spin-correlations, off-shell $t\bar{t}$ effects, and tW interference effects. Thus, it provides the most precise theoretical prediction of this process so far, which is why the validation of $b\bar{b}4\ell$ in ATLAS is important.

The impact of the generator on selected measurements will also be discussed, namely a direct top-quark decay width measurement, spin-correlation measurements and single top-quark measurements in the interference region of $t\bar{t}$ and tW.

Keywords: NLO Monte Carlo generator, $b\bar{b}4\ell$, top-quark, top-width

Contents

List of Figures

1. Introduction

To "*understand whatever binds the world's innermost core together*"[1] has always been the purpose of particle physics. Starting with the discovery of the first elementary particle at the end of the 19th century, particle physicists started building particle accelerators to collide particles. In a collision, the primary particles can be destroyed, while hundreds of new particles emerge, allowing the properties of the collided particles and the particles they transform into to be inferred. The energies used in collider experiments kept growing in order to provide access to smaller and smaller structures, coining the term *high energy physics*. The provisional highlight of that development was in the year 2008 with the first successful collisions of the Large Hadron Collider (LHC), the most powerful particle accelerator today with a design centre-of-mass energy of 14 TeV, currently operating at 13 TeV. The LHC is most notably known for the discovery of the long predicted Higgs boson in 2012. All particles and principles of particle physics, like conservation laws, were combined into one theory, the Standard Model (SM). It is the most precise theory to describe the fundamental particles and their interactions today, at energy scales currently feasible for particle accelerators.

The top-quark is the heaviest known elementary particle, already as massive as a Rhenium nucleus, the 75th element in the periodic table. This high mass is the reason for many interesting properties of the top-quark. It causes its exceptionally short lifetime, which allows for the properties of the top-quark to be measured directly through its decay products. This is not possible for other quarks, as they are usually bound to other quarks and do not appear individually. It can also play a special role in electroweak symmetry breaking, the mechanism explaining the masses of elementary particles.

In collider physics, it is not possible to measure just a single particle. A measurement always consists of the data from many particles, resulting in distributions of certain properties of the particles, e.g. momentum or angular distributions. The theoretical predictions of those distributions are computed by so-called Monte Carlo (MC) generators. Thus, they are crucial for testing theories and have to be constantly developed, to achieve higher precision and numerical stability.

In this master's thesis, the effect of a new MC generator on a direct top-quark decay width

[1] J. W. von Goethe, Faust

measurement will be studied. The new MC generator, called $b\bar{b}4\ell$, includes next-to-leading order precision decay matrix elements for the process $pp \to \ell^+ \nu_\ell l^- \bar{\nu}_l b\bar{b}$. Thus it is supposed to achieve a more precise description of the underlying theory and higher numerical stability.

A general overview of the SM will be provided in Ch. 2. This will include an introduction of the elementary particles present in the SM and a description of the fundamental interactions between them. The limitations of the SM will also be briefly explained. Additionally, a more detailed description of the top-quark will follow, including its general properties, the production mechanisms at the LHC and also the TEVATRON and its decay channels. In Ch. 3, the LHC and the ATLAS experiment will be introduced. This includes a description of the ATLAS detector and of computing resources provided by the collaboration. The general mechanics of MC generators are explained in Ch. 4, followed by a more detailed description of the $b\bar{b}4\ell$ generator and the computations done by MC generators. All results of the analysis will be provided in Ch. 5, divided into the work for tuning and validating the $b\bar{b}4\ell$ generator and the actual measurement of the impact on the top-quark decay width measurement. Also, a selection of observables relevant for other analyses will be discussed. A discussion of the results will follow in Ch. 6, including an outlook on prospective studies on this topic.

2. The Standard Model

In this chapter, the theoretical foundation of the Standard Model (SM) that is needed for this master's thesis will be provided. Sec. 2.1 is about the general structure of the SM, including the description of elementary particles and interactions, and also its limitations. In Sec. 2.2 the top-quark and its properties are presented.

2.1. General Aspects

With its development starting in the 1960's and 1970's, the SM is the most precise description of elementary particles and the fundamental interactions, namely the electromagnetic interaction, the weak interaction, and the strong interaction. Although it dominates phenomenology on cosmological scales, gravitation is not included, despite multiple attempts. The SM consists of two types of particles, fermions, which make up matter, and (gauge) bosons, which mediate the interactions. The following sections will discuss the Quantum Chromo Dynamics (QCD) [1–3] describing the strong interaction, the Glashow-Weinberg-Salam (GWS) [4–6] model describing the electroweak interaction, a combination of the electromagnetic and the weak interaction, and the Brout-Englert-Higgs mechanism [7, 8] that gives rise to the masses of the gauge bosons. Besides the already mentioned absence of a description of gravitation, the SM has further limitations, for example a missing description of dark matter and dark energy. A more complete and detailed list of limitations can be found in Sec. 2.1.6. Mathematically, the SM is described as a quantum field theory with an underlying symmetry group

$$SU(3)_C \times SU(2)_L \times U(1)_Y, \tag{2.1}$$

where C refers to colour charges, L to left-handed particles, and Y to hypercharge. These concepts will be introduced in the following sections. This group is the product of the symmetry groups of the QCD and the GWS models.

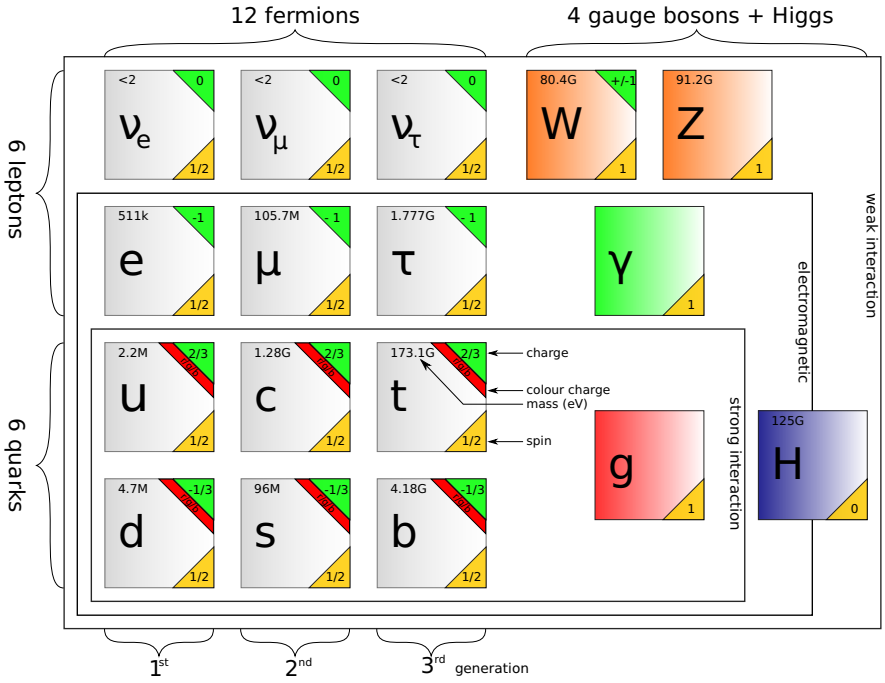

Figure 2.1.: All particles described by the SM. The left-hand side shows the 12 fermions, split into leptons and quarks. The right-hand side shows the 5 gauge bosons, including the Higgs boson. The Higgs boson is drawn in the electromagnetic and the weak rectangle, because it originates from the combination of these theories. All particles are labelled with their mass, charge, colour charge, and spin. The figure also shows the interactions in which the particles participate.

2.1.1. Elementary Particles of the Standard Model

Particles are generally divided into two groups, fermions and bosons, according to their spin. All particles with half-integer spin are fermions and all particles with integer spin are bosons. The elementary bosons are the mediators of the interactions and formally introduced via local gauge transformations of the corresponding Lagrangians (see Ch. 2.1.2), which is the reason why they are called gauge bosons. All particles have an antiparticle with the same mass but an inverse electric charge Q. The elementary fermions are divided into two classes, so-called quarks and leptons, according to the interactions in which they take part. Each of these classes consist of six particles, equally divided into three generations or families. All particles included in the SM can be found in Fig. 2.1. Both quarks and leptons will be discussed in further detail in the following.

Quarks The six quarks, also called six flavours[1], are the up-quark u, the down-quark d, the charm-quark c, the strange-quark s, the top-quark t and the bottom-quark b. Under a charged weak current, quarks undergo certain transitions, which are used to group them into weak isospin doublets χ_L:

$$\chi_u = \begin{pmatrix} u \\ d' \end{pmatrix}_L \quad \chi_c = \begin{pmatrix} c \\ s' \end{pmatrix}_L \quad \chi_t = \begin{pmatrix} t \\ b' \end{pmatrix}_L . \tag{2.2}$$

Right-handed chiral quarks are sorted into singlets, since the charged weak current does not couple to right-handed particles. According to their position in the isospin doublet, the quantum number I^3, which is the third component of the weak isospin, is assigned. All quarks in the upper row (up-type quarks) have $I^3 = +1/2$ and the quarks in the lower row (down-type quarks) have $I^3 = -1/2$. Also, all up-type quarks have $Q = +2/3e$ and all down-type quarks have $Q = -1/3e$, with the elementary electric charge e. The mass eigenstates d, s and b of the down-type quarks differ from their weak eigenstates d', s' and b'. They are connected through the Cabibbo-Kobayashi-Maskawa (CKM) matrix V_{CKM} [10, 11]:

$$\begin{pmatrix} d' \\ s' \\ b' \end{pmatrix} = \begin{pmatrix} V_{ud} & V_{us} & V_{ub} \\ V_{cd} & V_{cs} & V_{cb} \\ V_{td} & V_{ts} & V_{tb} \end{pmatrix} \begin{pmatrix} d \\ s \\ b \end{pmatrix} \tag{2.3}$$

$$= \begin{pmatrix} 1-\lambda^2/2 & \lambda & A\lambda^3(\rho - \imath\eta) \\ -\lambda & 1-\lambda^2/2 & A\lambda^2 \\ A\lambda^3(1-\rho-\imath\eta) & -A\lambda^2 & 1 \end{pmatrix} \begin{pmatrix} d \\ s \\ b \end{pmatrix} . \tag{2.4}$$

Eq. (2.4) shows the Wolfenstein-parametrisation [12] of the CKM matrix. Out of the four parameters A, λ, ρ and η, the complex term $(\rho - \imath\eta)$ is the only known reason for CP-violation[2].

Due to their participation in the strong interaction, they cannot be observed as free particles, but only in states made up of three quarks (baryons) or one quark and one antiquark (mesons). Moreover, bound states consisting of two quarks and two antiquarks (Tetraquarks), as well as bound states consisting of four quarks and one antiquark or vice versa (Pentaquarks), are possible. This property is called confinement and will be further discussed in Sec. 2.1.3.

The first three quarks u, d and s were first proposed by Murray Gell-Mann [13] and George Zweig [14] in 1964 to explain the steadily increasing number of known particles at that time

[1] After proposing the existence of originally three quarks, Murray Gell-Mann coined the term quarks following James Joyce's "Finnegans Wake" [9], which has the line "Three quarks for Muster Mark". A common assumption, also shared by Gell-Mann, is that the "quarks" in Finnegans Wake are drinks, which might make sense of the term flavour.

[2] In a CP-symmetric system, the physics does not change if all particles charges and parities are inversed.

with a substructure of those particles. First evidence for this model was found in deep inelastic scattering experiments at SLAC. Later, Glashow, Iliopoulos and Maiani (GIM) [15] proposed the so-called GIM mechanism to explain the rareness ($\Gamma_i/\Gamma = (6.84 \pm 0.11) \cdot 10^{-9}$) of the decay $K_L \to \mu^+\mu^-$. This was done by introducing a fourth quark c. The box diagram involving c has approximately the sign inverse amplitude as the box diagram involving u, thus the interference results in a nearly zero amplitude. The total amplitude would have been exactly zero, if both quarks had the same mass. The c-quark was discovered in 1974 by Burton Richter [16] at SLAC and simultaneously by Samuel Ting [17] at the Brookhaven National Laboratory. The third generation of quarks, including b and t, was proposed by Kobayashi and Maskawa to explain CP-violation by expanding the Cabbibo matrix from 2×2 to 3×3, which made the four already mentioned parameters necessary instead of just one real parameter in the Cabbibo matrix. The b-quark was discovered in 1977 at FERMILAB [18] and the t-quark was discovered in 1995, also at FERMILAB [19, 20].

Leptons Like quarks, the six leptons are also divided into three generations. Each generation includes a charged lepton ℓ, namely the electron $e^\pm$ (1), the muon $\mu^\pm$ (2) and the tauon $\tau^\pm$ (3), with the corresponding generation in parentheses. All have the electric charge $\pm e$. Every charged lepton has a neutral weak isospin partner in its generation, called neutrino ν_ℓ. With this, the left-handed isospin doublets are:

$$\chi_e = \begin{pmatrix} \nu_e \\ e \end{pmatrix}_L \quad \chi_\mu = \begin{pmatrix} \nu_\mu \\ \mu \end{pmatrix}_L \quad \chi_\tau = \begin{pmatrix} \nu_\tau \\ \tau \end{pmatrix}_L . \tag{2.5}$$

Here, the neutrinos have $I^3 = +1/2$ and the charged leptons have $I^3 = -1/2$. All right-handed leptons form isospin singlets. Each generation has its own quantum number, called electron number L_e for the first generation, muon number L_μ for the second generation and tau number L_τ for the third generation. These quantum numbers are conserved in production. In contrast to other conserved quantities, like charge or energy, this conservation law is purely empirical with no underlying symmetry in the quantum field theory. However, those quantum numbers are not conserved in general, as neutrinos were found to oscillate, i.e. changing their flavour as they propagate. This is a direct consequence from neutrinos being massive particles, so the observation of neutrino oscillation is considered to be the proof of non-zero neutrino masses. Analogous to the CKM matrix, the Pontecorvo-Maki-Nakagawa-Sakata (PMNS) matrix [21, 22]

$$U_{PMNS} = \begin{pmatrix} U_{e1} & U_{e2} & U_{e3} \\ U_{\mu 1} & U_{\mu 2} & U_{\mu 3} \\ U_{\tau 1} & U_{\tau 2} & U_{\tau 3} \end{pmatrix} \tag{2.6}$$

was introduced to relate the mass eigenstates of the neutrinos to their flavour eigenstates.

The electron was discovered in 1897 by Joseph John Thomson using cathode rays [23]. The corresponding neutrino was proposed by Wolfgang Pauli in 1930 [24]. At that time, β-decays seemed to violate energy and momentum conservation, as the energy and the momentum carried by the neutrino could not be measured. To solve this problem, Pauli proposed an undetectable particle, which was later named neutrino. The first detection of electron neutrinos succeeded in 1956 in the Cowan-Reines neutrino experiment [25]. Electron neutrinos produced in a nuclear reactor were captured by a proton, which created a positron. This positron annihilates with an electron, producing two photons that could be detected. Muons were discovered 1936 by Anderson and Neddermayer [26], studying cosmic radiation. The muon neutrinos were discovered in 1962 by Leon Lederman, Melvin Schwartz and Jack Steinberger at the Brookhaven National Laboratory [27]. Tauons were discovered in 1975 by Martin Perl at SLAC [28] and the corresponding tau neutrino was discovered in the year 2000 at the DONUT experiment [29].

2.1.2. Local Gauge Invariance and Gauge Bosons

In this section, the concept of local gauge invariance in quantum field theories on the basis of quantum electrodynamics (QED), the quantum field theory describing the electromagnetic interaction, is presented. Gauge invariance is an essential property of quantum field theories, as most gauge invariant theories are also renormalisable. QED is based on the Dirac Lagrangian

$$\mathscr{L} = \imath\bar{\psi}\gamma^{\mu}\partial_{\mu}\psi - m\bar{\psi}\psi, \tag{2.7}$$

using the Einstein summation convention. This Lagrangian describes the dynamics of free fermions with spinor ψ and adjoint spinor $\bar{\psi} = \psi^{\dagger}\gamma^{0}$. Applying the local $U(1)$ phase transformation

$$\psi \to e^{\imath\theta(x^{\mu})}\psi \tag{2.8}$$

on Eq. (2.7), it becomes the transformed Lagrangian

$$\mathscr{L}' = \mathscr{L} - \bar{\psi}\gamma^{\mu}\psi\partial_{\mu}\theta = \mathscr{L} + q\bar{\psi}\gamma^{\mu}\psi\partial_{\mu}\lambda, \tag{2.9}$$

with $\theta(x^{\mu}) = -q\lambda(x^{\mu})$. Thus, the Lagrangian is not invariant under $U(1)$ transformation. To restore the invariance, a gauge field A_{μ} can be added to the Lagrangian like

$$-q\bar{\psi}\gamma^{\mu}\psi A_{\mu}, \tag{2.10}$$

where A_μ transforms as

$$A_\mu \to A_\mu + \partial\lambda. \tag{2.11}$$

This field is described by the kinetic term

$$-\frac{1}{4}F^{\mu\nu}F_{\mu\nu} \tag{2.12}$$

in the Lagrangian, with $F^{\mu\nu} = \partial^\mu A^\nu - \partial^\nu A^\mu$. A mass term, typically of the form

$$\frac{1}{2}m_A^2 A^\mu A_\mu \tag{2.13}$$

cannot be added, as the product $A^\mu A_\mu$ transforms like

$$A^\mu A_\mu \to A^\mu A_\mu + 2A^\mu \partial_\mu\lambda + \partial^\mu\lambda\,\partial_\mu\lambda \tag{2.14}$$

under the transformation of A given in Eq. 2.11, which is evidently not equal. Using this, the Lagrangian $\mathscr{L}_{\text{QED}}$ can be written as

$$\mathscr{L}_{\text{QED}} = \imath\bar{\psi}\gamma^\mu D_\mu\psi - m\bar{\psi}\psi - \frac{1}{4}F^{\mu\nu}F_{\mu\nu}, \tag{2.15}$$

where the covariant derivative $D_\mu = \partial_\mu + \imath qA_\mu$ implements the interaction between the fermions and the gauge field. This Lagrangian is fully invariant under any local $U(1)$ transformation. The introduced massless gauge field is interpreted as the photon, coupling to fermions with electric charge q, which can be seen in the definition of the covariant derivative and the QED Lagrangian, see Eq. 2.15.

It was shown that gauge fields, interpreted as gauge bosons, are a direct and necessary consequence of local gauge invariance. Those gauge bosons have to be massless, because explicit mass terms would violate the local gauge invariance. The masses of the gauge bosons will be introduced using the Brout-Englert-Higgs (BEH) mechanism in Sec. 2.1.5. In general, the number of gauge bosons required to preserve local gauge invariance under a certain symmetry group equals the number of generators of that group. It should be noted that in case of non-Abelian gauge groups, like $SU(2)$ or $SU(3)$, the emerging gauge bosons also interact with each other.

2.1.3. Quantum Chromodynamics

Quantum chromodynamics (QCD) is the quantum field theory describing the strong interaction. As the name suggests, the corresponding charge, i.e. quantum number, is the colour charge, which is only carried by quarks and gluons, the gauge bosons of the QCD. The colour charge can have three different values; red r, green g and blue b, whereas antiquarks carry the corresponding anticolours; antired $\bar{r}$, antigreen $\bar{g}$ and antiblue $\bar{b}$.

The Lagrangian of the QCD is

$$\mathscr{L}_{\mathrm{QCD}} = -\frac{1}{4} G_{a\mu\nu} G_a^{\mu\nu} + \sum_i \bar{q}_i (\imath \gamma^\mu D_\mu - m_i) q_i, \tag{2.16}$$

with an underlying symmetry group $SU(3)$. Here, $G_a^{\mu\nu} = \partial^\mu G_a^\nu - \partial^\nu G_a^\mu - g_s f^{abc} G_b^\mu G_c^\nu$ with gluon fields G_a^μ. The indices a, b and c denote the colour combination of the gluon. To conserve the colour charge, gluons always carry a colour and an anticolour. As $SU(3)$ has 8 generators, there are eight combinations of colour and anticolour that do not result in a colourless singlet, but in an octet. The factors f^{abc} are the so-called structure constants of QCD that are caused by $SU(3)$ being a non-Abelian group. They represent the self-interaction of gluons. The constant g_s is the strong coupling constant. The second term in Eq. (2.16) describes the interaction between the gluons and quarks q_i of any flavour i. Analogously to Sec. 2.1.2, the covariant derivative is defined as $D_\mu = \partial_\mu + \imath g_s \frac{\lambda_a}{2} G_{a\mu}$, with the Gell-Mann matrices λ_a.

Due to the non-Abelian structure of $SU(3)$, the coupling strength α_s of the strong interaction increases with the distance between two colour charged objects, or decreases with increasing momentum transfer Q^2:

$$\alpha_s(Q^2) = \frac{12\pi}{(33 - 2n_f)\log(Q^2/\Lambda^2)}, \tag{2.17}$$

where n_f is the number of flavours relevant at the corresponding energy scale, and Λ^2 is the pole. It should be noted that this expression is not correct for small Q^2, as the perturbative calculations become invalid. The energy needed to separate two quarks is larger than the energy needed to produce a new pair of quarks. This causes a phenomenon called confinement. Quarks can never be observed as free particles, because whenever there is enough energy to separate two quarks a new pair is produced out of the vacuum, so that both quarks end up being bound to newly produced quarks. This effect is schematically shown in Fig. 2.2. Because the coupling strength approaches zero for high energies, quarks are usually denoted as asymptotically free.

Particles consisting of three quarks or three antiquarks are called baryons, particles consisting of a quark and an antiquark are called mesons. There are also less strongly bound particles consisting of two quarks and two antiquarks, called Tetraquark [30], and four quarks and one antiquark or vice versa, called Pentaquarks [31]. In general, particles made of quarks are called

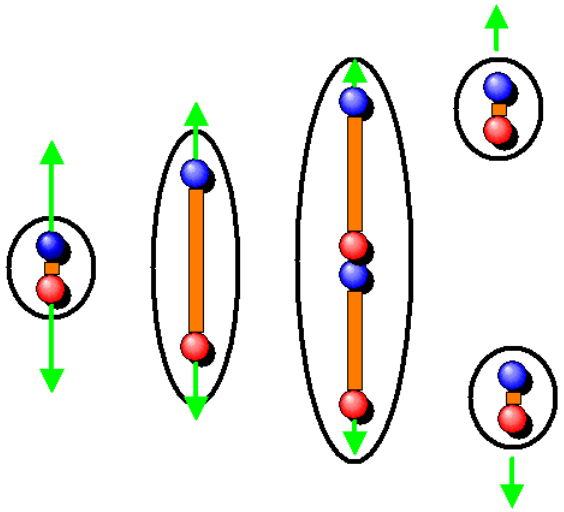

Figure 2.2.: A schematic depiction of confined quarks. The energy stored in the potential between the two quarks gets larger as the distance between them increases. At a certain point, the energy is large enough to create a new pair of quarks. With the new pair of quarks, two hadrons are formed.

hadrons.

2.1.4. Electroweak Unification

As already mentioned in Sec. 2.1.1, the weak interaction is sensitive to the chirality of particles. The chiral spinors $\psi_{L/R}$ of any fermion state can be obtained by applying the corresponding projector $P_{L/R}$:

$$\psi_{L/R} = \underbrace{\frac{1 \mp \gamma^5}{2}}_{P_{L/R}} \psi, \tag{2.18}$$

with $\gamma^5 = \imath\gamma^0\gamma^1\gamma^2\gamma^3$. Using this, the charged weak current $j_\mu^\pm$ can be defined as

$$j_\mu^\pm = \bar{\chi}_L \gamma_\mu \tau^\pm \chi_L \tag{2.19}$$

and the neutral weak current j_μ^3 can be defined as

$$j_\mu^3 = \bar{\chi}_L \gamma_\mu \frac{1}{2} \tau^3 \chi_L, \tag{2.20}$$

with $\tau^{\pm} = (1/2)(\tau^1 \pm \imath\tau^2)$ and τ^i the i-th Pauli matrix and the isospin doublets defined in Eq. (2.2) and Eq. (2.5). The neutral electromagnetic current can be written as

$$j_\mu^{EM} = -\bar{\ell}_L \gamma_\mu \ell_L - \bar{\ell}_R \gamma_\mu \ell_R \tag{2.21}$$

for any charged lepton spinor $\ell_{L/R}$. To combine both neutral currents, the weak hypercharge $Y = 2(I^3 - Q)$ is introduced. Consequently the hypercharge current is

$$j_\mu^Y = 2(j_\mu^3 - j_\mu^{em}). \tag{2.22}$$

The symmetry group describing this interaction is the $SU(2)_L \times U(1)_Y$. This is a product of the group $SU(2)_L$ originating from the charged weak currents acting only on left-handed particles and the group $U(1)_Y$ originating from the neutral currents acting on hypercharges.

The electroweak Lagrangian is

$$\mathscr{L}_{\text{EW}} = -\frac{1}{4} W_{i\mu\nu} W_i^{\mu\nu} - \frac{1}{4} B_{\mu\nu} B^{\mu\nu} + \imath \sum_{\text{gen.}} [\bar{L} \not{D} L + \bar{Q} \not{D} Q + \bar{u}_R \not{D} u_R + \bar{d}_R \not{D} d_R + \bar{e}_R \not{D} e_R], \tag{2.23}$$

with $B_{\mu\nu} = \partial_\mu B_\nu - \partial_\nu B_\mu$ for the photon field B_μ and $W_i^{\mu\nu} = \partial^\mu W_i^\nu - \partial^\nu W_i^\mu - g\varepsilon^{ijk} W_j^\mu W_k^\nu$ for the three weak bosons W_i^μ. The sum runs over all three generations and Q and L are the isospin doublets from Eq. (2.2) and Eq. (2.5), respectively. The right-handed isospin singlets are denoted with an R. The covariant derivative for this symmetry group is defined as

$$D_\mu = \partial_\mu + \frac{\imath g}{2} \vec{\tau} \vec{W} + \frac{\imath g'}{2} Y B_\mu, \tag{2.24}$$

where g and g' are coupling constants and $\vec{\tau}$ and $\vec{W}$ are vectors with the Pauli matrices τ^i and three weak gauge fields as components. Also, the Dirac slash notation $\not{D} = \gamma^\mu D_\mu$ is used.

In nature, the fields in the Lagrangian are not observed, but mixtures of them. This is because of the BEH mechanism discussed in the following Sec. 2.1.5. The first two weak gauge fields are mixed to the physical $W^\pm$ fields and the third weak field is mixed with the electromagnetic field giving the Z boson and the photon. The mixing angle for the neutral fields is the so-called Weinberg angle θ_W. The couplings are related according to

$$g_W \sin\theta_W = g' \cos\theta_W = g_e. \tag{2.25}$$

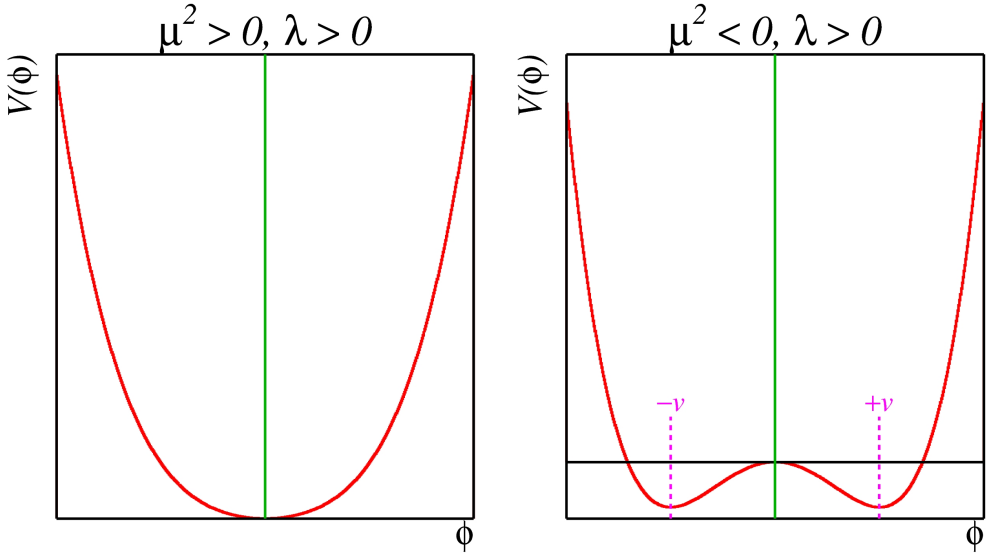

Figure 2.3.: A plot of the potential $V(\phi) = \mu^2\phi^2 + \lambda\phi^4$ for positive λ and positive μ^2 on the left-hand side and negative μ^2 on the right-hand side. If μ^2 is positive, the curve shows a single minimum at $\phi = 0$. For negative values of μ^2, the curve has two minima at $v^2 = -(\mu^2/\lambda)$.

2.1.5. Brout-Englert-Higgs Mechanism

According to the Lagrangian shown in Eq. (2.23), all gauge bosons are massless to conserve the local gauge invariance. This contradicts the observation of W bosons having a mass $m_W = 80.385 \pm 0.015$ GeV [32] and the Z boson having a mass $m_Z = 91.1876 \pm 0.0021$ GeV [32]. To introduce the boson masses into the Lagrangian, while preserving the local gauge invariance, the BEH mechanism was proposed. In the BEH mechanism, the mass terms are introduced via electroweak symmetry breaking. For that, a potential of the form $V(\phi) = \mu^2\phi^2 + \lambda\phi^4$ is introduced to the Lagrangian, where ϕ is a scalar field. The potential is plotted in Fig. 2.3 for two different choices of the parameters. In both cases λ is positive, whereas μ^2 can be positive or negative. If it is positive, the curve has one minimum at $\phi = 0$. But if μ is negative, the curve has two minima at $v^2 = -(\mu^2/\lambda)$, where v is the so-called vacuum expectation value[3] (VEV).

The electroweak theory includes three massive bosons. For all of them, one degree of freedom (DOF) must be present in the theory. Additionally, one DOF is needed for the scalar boson of the BEH mechanism, the so-called Higgs boson. Therefore, a complex scalar doublet

$$\phi = \begin{pmatrix} \phi^+ \\ \phi^0 \end{pmatrix} = \frac{1}{\sqrt{2}} \begin{pmatrix} \phi_1 + \imath\phi_2 \\ \phi_3 + \imath\phi_4 \end{pmatrix} \tag{2.26}$$

[3]The VEV is not predicted by the BEH mechanism. Measurements give a value of approximately 246 GeV.

with overall four DOF is needed. Thus, the potential has the form

$$V(\phi) = \mu^2 \phi^\dagger \phi + \lambda (\phi^\dagger \phi)^2. \tag{2.27}$$

As it is a function in the two-dimensional complex plane, it has degenerate minima when $\sum_{i=1}^{4} \phi_i^2 = v^2/2$, for $\mu^2 < 0$. In consequence, the minimal state is chosen as

$$\langle \phi \rangle_v = \frac{1}{\sqrt{2}} \begin{pmatrix} 0 \\ v \end{pmatrix}. \tag{2.28}$$

Then, the field can be expanded around the minimum giving the expression

$$\phi(x) = \frac{1}{\sqrt{2}} \begin{pmatrix} 0 \\ v + h(x) \end{pmatrix}. \tag{2.29}$$

The Lagrangian of the introduced complex scalar doublet is

$$\mathscr{L} = (\partial_\mu \phi)^\dagger (\partial^\mu \phi) - \mu^2 \phi^\dagger \phi - \lambda (\phi^\dagger \phi)^2. \tag{2.30}$$

Replacing the partial derivative with the covariant derivative defined in Eq. (2.24) and evaluating the kinetic term of the Lagrangian gives

$$\begin{aligned} (D_\mu \phi)^\dagger (D^\mu \phi) =& \frac{1}{2} (\partial_\mu h)(\partial^\mu h) + \frac{1}{8} g_W^2 \overbrace{(W_\mu^1 + \imath W_\mu^2)}^{\sqrt{2} W_\mu^-} \overbrace{(W^{1\mu} - \imath W^{2\mu})}^{\sqrt{2} W_\mu^+} (v+h)^2 \\ &+ \frac{1}{8} (g_W W_\mu^3 - g' B_\mu)(g_W W^{3\mu} - g' B^\mu)(v+h)^2. \end{aligned} \tag{2.31}$$

It can already be seen how the first two weak gauge fields mix. Expanding the products and looking only at the terms quadratic in the first two weak gauge fields, one obtains

$$\frac{1}{8} v^2 g_W^2 (W_\mu^1 W^{1\mu} + W_\mu^2 W^{2\mu}). \tag{2.32}$$

This is a Lagrangian mass term, corresponding to the mass $m_W = (1/2) g_W v$. The same can be done for the neutral gauge fields, yielding

$$\frac{v^2}{8} \begin{pmatrix} W_\mu^3 & B_\mu \end{pmatrix} \begin{pmatrix} g_W^2 & -g_W g' \\ -g_W g' & g'^2 \end{pmatrix} \begin{pmatrix} W^{3\mu} \\ B^\mu \end{pmatrix}, \tag{2.33}$$

where a non-diagonal mass matrix was introduced. Diagonalising this matrix yields the eigenvalues $\alpha_1 = 0$ and $\alpha_2 = g_W^2 + g'^2$. This translates into the photon mass $m_A = 0$ and the Z mass

$m_Z = (1/2)v\sqrt{g_W^2 + g'^2}$. Using the definition of the Weinberg angle $\tan\theta_W = g'/g_W$, the mixing is

$$A_\mu = \cos\theta_W B_\mu + \sin\theta_W W_\mu^3 \tag{2.34}$$

$$Z_\mu = -\sin\theta_W B_\mu + \cos\theta_W W_\mu^3 \tag{2.35}$$

It was shown how the BEH mechanism is used to introduce the masses of the gauge bosons to the SM Lagrangian and that the mixing of the gauge bosons is a direct consequence of it. This concept can be extended to fermion masses by introducing a coupling between the Higgs field, left-handed isospin doublets and right-handed isospin singlets χ_R:

$$-g_F(\bar{\chi}_L\phi\chi_R + \bar{\chi}_R\phi\chi_L), \tag{2.36}$$

with the Yukawa-coupling g_F and adjoint doublets/singlets $\bar{\chi}$. The resulting fermion masses are $m_F = \sqrt{2}(g_F/v)$. This holds for all fermions with positive weak isospin. For the fermions with negative weak isospin the same can be done by using the conjugate Higgs doublet $\phi_c = -\imath\tau^2\phi^*$.

The Higgs boson was discovered in 2012 at the ATLAS detector [33] and the CMS detector [34]. The BEH mechanism predicts no value for the mass of the Higgs boson $m_H = \sqrt{2\lambda v^2}$. The average measured mass is $m_H = 125.09 \pm 0.24$ GeV [32].

2.1.6. Limitations of the Standard Model

Although being the most precise description of elementary particles so far, the SM has still several limitations. The most important ones will be briefly addressed in this section.

Neutrino Masses Neutrino masses are not incorporated in the SM. Although it would be mathematically possible to add corresponding mass terms via the BEH mechanism, the existence of right-handed neutrinos and left-handed antineutrinos was disproved in the Goldhaber experiment [35]. This makes Eq. (2.36) inapplicable. A possible alternative is the Seesaw mechanism [36–38].

Dark Matter According to the standard model of cosmology, the universe consists of 26.8% dark matter, 68.3% dark energy, and only 4.9% matter made of SM particles [39]. Up to now, the SM does not provide any explanation for dark matter nor dark energy. First evidence for dark matter was the unexpected high rotational velocity of stars in the outer areas of galaxies, which can only be explained with a much higher mass density in the galaxy than directly observable [40, 41]. The favoured explanation is that it consists of weakly interacting massive particles

(WIMPS). To explain all findings, they need to be electrically neutral, stable and having a high mass. No SM particles fulfil those requirements. A common candidate are supersymmetric theories [42–44].

Dark Energy The universe is expanding, which expands also the wavelength of light travelling through space. If the distance is long enough, i.e. the light is emitted in another galaxy, this so-called redshift can be measured, which proves the expansion of the universe. The redshift also yields information on the acceleration of the expansion, if multiple lightsources in different distances from earth are studied. Those measurements reveal that the expansion is even accelerating. This is not possible with a universe only containing matter. To explain the findings, the above mentioned portion of 68.3% dark energy is needed [45].

Baryon Asymmetry The universe contains almost no antimatter. This gap between antimatter and matter cannot be sufficiently explained by the CP-violation caused by the complex CKM matrix element.

Gravitation The theory used to describe gravitation is Einstein's theory of general relativity (GRT), which is a classical field theory, not a quantum field theory. Even though multiple attempts were made, the GRT could not be turned into a quantum field theory because the theory is not renormalisable.

Gauge Hierarchy The SM does not explain why the electroweak energy scale is so much smaller than the Planck scale, which is the energy scale where gravity effects become significant. Theories addressing this problem are supersymmetric theories and theories with extra dimensions, e.g. the Randall-Sundrum model [46, 47]. In general, the SM does not explain why the parameters have the values they do have.

2.2. The Top-Quark

The purpose of this thesis is to study the effect of next-to-leading order terms in the MC generator on the direct top-quark decay width measurements. Thus, this section will provide necessary information about the top-quark, the $t\bar{t}$ pair-production and the decay of top-quarks. The MC generator under study includes all processes leading to a dilepton final state $e^+\mu^-$, dominantly from $t\bar{t}$ and tW processes. For this reason, a description of single top production is included in this section.

2.2.1. Top-Quark Properties

The top-quark is the heaviest known elementary particle. After its discovery in 1995 by CDF and DØ, many measurements tried to access its properties. Today's world average top-quark mass [32] is

$$m_t = 173.21 \pm 0.51(\text{stat}) \pm 0.71(\text{syst})\ \text{GeV}. \tag{2.37}$$

This high mass is interesting for various reasons. The Yukawa-coupling introduced in Eq. (2.36) should be approximately equal to one. For this reason, the top-quark is could play an important role in the electroweak symmetry breaking.

Its high mass is also the reason for its short lifetime. The lifetime is the inverse of the decay width Γ_t, the full width at half maximum (FWHM) of the mass distribution. The predicted width at NLO [48] is:

$$\Gamma_t = \frac{G_F m_t^3}{8\pi\sqrt{2}} \left(1 - \frac{m_W^2}{m_t^2}\right)^2 \left(1 + 2\frac{m_W^2}{m_t^2}\right) \left[1 - \frac{2\alpha_s}{3\pi}\left(\frac{2\pi^2}{3} - \frac{5}{2}\right)\right], \tag{2.38}$$

with Fermi's constant G_F. Assuming $\alpha_s(m_Z) = 0.118$ and an approximate value $m_t = 173.3$ GeV, the predicted width is $\Gamma_t = 1.35$ GeV. A recent ATLAS measurement [49] yields a value

$$\Gamma_t = 1.76^{+0.33+0.79}_{-0.33-0.68}\ \text{GeV}. \tag{2.39}$$

The corresponding lifetime is $\tau_t \approx 0.5 \times 10^{-24}$ s. This time scale is especially shorter than the typical hadronisation time $\mathcal{O}(10^{-23}\ \text{s})$ in QCD [50]. That means, the top-quark decays before forming hadrons with other quarks, thus it transfers its properties directly onto its decay products. This makes the top-quark properties directly accessible in measurements, unlike the properties of the other quarks.

Like every other up-type quark, the top-quark has spin $S = 1/2$ and charge $Q = (2/3)e$.

2.2.2. Top-Quark Production

This section will focus on the production of single top-quarks and top-quark pairs at the LHC, a proton-proton collider, starting with the pair production mechanism.

Top-Quark Pair Production At the LHC, top-quark pairs can be produced via two different mechanisms, gluon fusion and quark-antiquark annihilation. The four leading order Feynman diagrams are shown in Fig. 2.4. The contributions of those two mechanisms to the total cross-section are different, though. The number of events generated by each mechanism, is dependent on the centre-of-mass energy $\sqrt{s}$ and the so-called Bjorken-x, the ratio of the parton momentum

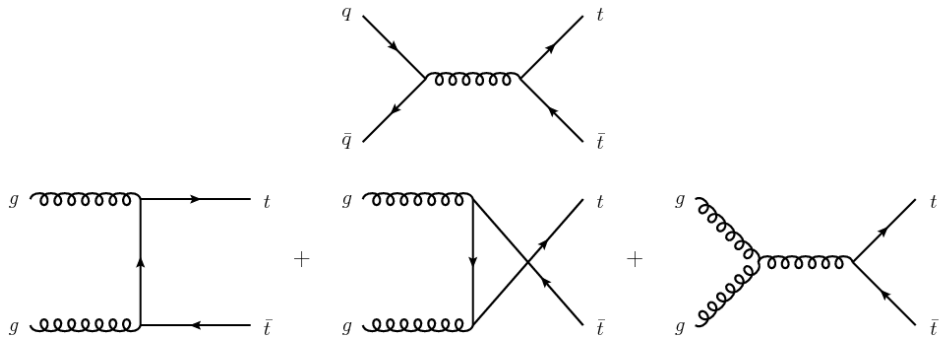

Figure 2.4.: The four leading order diagrams for $t\bar{t}$ production at the LHC. Quark-antiquark annihilation can only happen via one diagram (at the top), while gluon fusion has three different channels (at the bottom).

to the proton momentum. Because of the proton being a particle consisting of three quarks, u, u and d, the so-called valence quarks, and many other strong interacting particles, the effective centre-of-mass energy $\sqrt{\hat{s}}$ in an collision is lower, since only two partons interact and not the whole proton. Due to the different behaviour of the Bjorken-x for quarks and gluons within protons, see Fig. 2.5, one mechanism is preferred at certain energies. The region of higher Bjorken-x is dominated by the valence quarks of the proton, u and d. Gluons are by far dominating at lower x values. The required $\sqrt{\hat{s}}$ needed to produce top-quark pairs is $2m_t \approx 350$ GeV. This corresponds to a Bjorken-x:

$$2x = \frac{350\,\text{GeV}}{13000\,\text{GeV}} \approx 0.027, \tag{2.40}$$

with $\sqrt{s} = 13$ TeV at the LHC and assuming equivalent Bjorken-x for both interacting partons. Due to this low threshold of $2.7\%/2 = 1.35\%$ per parton, the $t\bar{t}$ production is dominated by gluon fusion at the LHC at 13 TeV. About 85% of the top-quark pairs are produced via gluon fusion. At the TEVATRON, a proton-antiproton collider with $\sqrt{s} = 1.96$ TeV in Run II, approximately 85% of all $t\bar{t}$ were produced via quark-antiquark annihilation, as the required Bjorken-x was approximately 9% per parton, hence in the valence quark dominated value range.

The overall production cross-section is energy dependent. The theoretical prediction at NNLO+NNLL (next-to-next-to-leading logarithm) [52] for the TEVATRON $\sqrt{s}$ of 1.96 TeV is $\sigma_{t\bar{t}} = 7.16^{+0.11+0.17}_{-0.20-0.12}$ pb, with the scale uncertainty as the first listed uncertainty and the PDF uncertainty as the second. All TEVATRON measurements combined yield a value $\sigma_{t\bar{t}} = 7.6 \pm 0.41$ pb [53]. For the LHC, the theoretical predictions are $\sigma_{t\bar{t}} = 831.8^{+19.8+35.1}_{-29.2-35.1}$ pb for 13 TeV and $\sigma_{t\bar{t}} = 984.5^{+23.2+41.3}_{-34.7-41.3}$ pb at 14 TeV, the design energy of the LHC. A recent measurement of the 13 TeV cross-section by ATLAS in the mixed dilepton final state yielded $\sigma_{t\bar{t}} = 818 \pm 8(\text{stat.}) \pm 27(\text{syst.}) \pm 19(\text{lumi.}) \pm 12(\text{beam})$ pb [54].

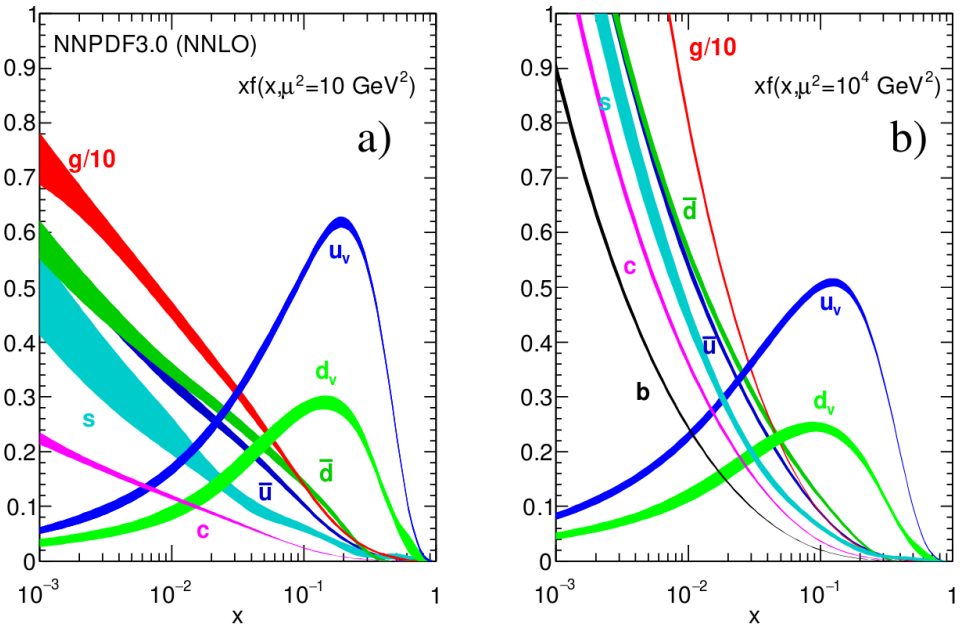

Figure 2.5.: The Bjorken-x distributions for all kind of partons of the proton at the scale a) $\mu^2 = 10\,\text{GeV}^2$ and b) $\mu^2 = 10^4\,\text{GeV}^2$. The PDFs are based on the next-to-next-to-leading (NNLO) order PDF set NNPDF3.0 [51]. In both cases can be seen that the valence quarks are dominating the higher value range, while the gluons dominate the lower value range. The gluon curve is suppressed by a factor of 10 to fit into the picture.

Single Top Production In contrast to strongly produced top-quark pairs, the single top production is an electroweak process. The four LO diagrams are shown in Fig. 2.6, where the t-channel dominates at the LHC with predicted cross-sections of $\sigma_t = 63.89^{+2.91+0.65+0.14}_{-2.52-0.65-0.14}$ pb, $\sigma_t = 84.69^{+3.76+0.82+0.18}_{-3.23-0.82-0.18}$ pb and $\sigma_t = 216.99^{+9.04+1.81+0.39}_{-7.71-1.81-0.39}$ pb for 7, 8 and 13 TeV, respectively, three times as large as s-channel and tW production combined. Those predictions were computed in NLO QCD using the Hathor v2.1 program [55, 56]. The first stated uncertainty accounts for uncertainties in scale, PDFs and α_s [57–61], the second one for mass uncertainties and the last one for beam energy uncertainties. An ATLAS measurement of the t-channel single top production [62] yielded $\sigma_{t,t} = 156 \pm 5(\text{stat}) \pm 27(\text{syst}) \pm 3(\text{lumi})$ pb and $\sigma_{t,\bar{t}} = 91 \pm 4(\text{stat}) \pm 18(\text{syst}) \pm 2(\text{lumi})$ pb for t and $\bar{t}$, respectively.

The tW production has an expected cross-section of $\sigma_{tW} = 71.7 \pm 1.8(\text{scale}) \pm 3.4(\text{PDF})$ pb at 13 TeV, according to NNLO predictions. A recent measurement yielded $\sigma_{tW} = 94^{+10+28+2}_{-10-22-2}$ pb [63] with statistical uncertainty, systematic uncertainty and luminosity uncertainty, respectively. The s-channel is expected to have a cross-section of $\sigma_s = 10.32^{+0.40+0.23+0.01}_{-0.36-0.22-0.01}$ pb at 13 TeV, but no measurement has been published yet. An 8 TeV measurement yielded a value of $\sigma_s = 4.8^{+0.8+1.6}_{-0.8-1.3}$ pb [64], with statistical and systematic uncertainties, compared to an expected

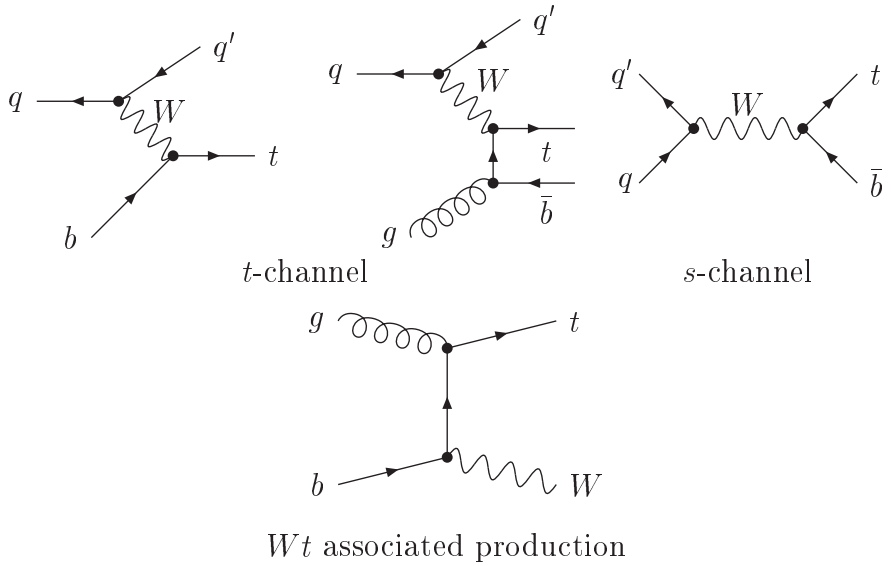

Figure 2.6.: Three different channels for single top production. The t-channel on the top left part of the image, with a quark and possibly an additional b-quark in the final state. In the s-channel in the top right corner of the image, an intermediate W boson decays into a t and a b. The tW associated production has a t and a W in the final state.

value of $\sigma_s = 5.24^{+0.22+0.12+0.01}_{-0.20-0.12-0.01}$ pb. The theoretical values were calculated using the above mentioned Hathor v2.1 program, thus the order and meaning of the uncertainties is the same as above.

2.2.3. Top-Quark Decays

The top-quark, as it is the heaviest quark, can decay into real W bosons. This happens in almost every case. In this decay, the top-quark undergoes a transition within the weak isospin doublets shown in Eq. (2.2). As the down-type quarks are rotated using the CKM matrix, the branching ratio $\mathscr{B}$ is determined by the corresponding squared CKM matrix elements, i.e.

$$\mathscr{B} = \frac{|V_{tq}|^2}{|V_{td}|^2 + |V_{ts}|^2 + |V_{tb}|^2} \tag{2.41}$$

for any down-type quark q. The decay into a b-quark has the highest branching ratio, with an average measured CKM matrix element [32]

$$|V_{tb}| = 1.009 \pm 0.031. \tag{2.42}$$

A recent measurement at CMS found $R = 1.014 \pm 0.003(\text{stat}) \pm 0.032(\text{syst})$ [65], with R being the fraction of decays into b-quarks of all decays into quarks, thus the decays into s-quarks and d-quarks are negligible.

Given this, the decay channels are classified predominantly through the decay products of the W boson. The W boson can decay into quarks, $\mathscr{B}_{\text{had}} = (67.41 \pm 0.27)\% \approx 2/3$, and leptons, $\mathscr{B}_{\ell} = (10.86 \pm 0.09)\% \approx 1/9$ each. When classifying the decay channels, only electrons and muons are counted as leptons, because tauons can also decay into hadrons. In these cases, they would be detected as jets. In a $t\bar{t}$ event, there are two decaying W bosons, resulting in three different classifications.

All-Hadronic Channel In this channel, both W bosons decay hadronically. Using the approximate fractions for decays into quarks mentioned above, the probability P of this channel to occur is

$$P_{\text{all-had}} \approx \frac{2}{3} \cdot \frac{2}{3} \approx \frac{36}{81}. \tag{2.43}$$

The all-hadronic channel has the highest probability to occur, but also the largest background, due to its signature consisting only of jets, even though it includes also two b-jets.

Lepton+Jets Channel In the ℓ+jets channel, one W boson decays hadronically and the other one decays leptonically. The probability for this channel is

$$P_{\ell+\text{jets}} \approx 2 \cdot \frac{2}{3} \cdot \frac{2}{9} \approx \frac{24}{81}. \tag{2.44}$$

This channel has still comparably high statistics, with the benefit of a lepton in the signature. This makes it easier to detect than an all-hadronic event. The transverse momentum of the neutrino can still be reconstructed by using the missing transverse energy $\not{E}_T$.

Dilepton Channel If both W bosons decay into leptons, it is called dilepton channel. The probability of this channel is

$$P_{\text{dil}} \approx \frac{2}{9} \cdot \frac{2}{9} \approx \frac{4}{81}. \tag{2.45}$$

This channel has by far the lowest statistics, but also a very low background, due to its very clear signature of two leptons and two b-jets, which differ from other jets by its production vertex, which is deplaced from the primary vertex, caused by the comparably long lifetime of the b-quark. Thus, they can be tagged. Beside the low statistics, this channel has the disadvantage that the neutrinos' transverse momenta can only be reconstructed in superposition, not individually. The MC generator under study is only available in this channel with an $e^+\mu^-$ final state.

3. The LHC and the ATLAS Experiment

This chapter will introduce the ATLAS detector, which is one of the two multi-purpose detectors at CERN, and the Large Hadron Collider (LHC), the most powerful particle accelerator today.

3.1. The LHC

The LHC [66] is a proton-proton collider with a design centre of mass energy $\sqrt{s}$ of 14 TeV located at CERN (**C**onseil **e**uropéen pour la **r**echerche **n**ucléaire, eng: European Organization for Nuclear Research). It is a synchrotron with an approximate circumference of 27 km, built on average 100 m under the surface. Its construction, reusing the LEP accelerator tunnel, was approved in December 1994. From then on, it took nearly 14 years until the first proton beam test run was successfully performed on the 10th of September, 2008. The first high energy run at $\sqrt{s} = 7$ TeV started in March, 2010. Approximately two years later, a run with an enhanced $\sqrt{s}$ of 8 TeV started in early April, 2012. Currently, the LHC is running at $\sqrt{s} = 13$ TeV, after a successful upgrade finished at the 3rd of June, 2015, officially starting Run II. Other than protons, the LHC can also accelerate ions, like lead, to an energy of 2.56 TeV per nucleon.

The LHC is not constructed as one perfect circle, but it consists of eight arcs connected through eight straight insertions, see Fig. 3.1. The beam is bent within the arcs using 154 dipole magnets per arc, 1232 in total. Moreover, a total of 392 quadrupole magnets are used to focus the beam. Those magnets are superconducting magnets and are operated at a temperature of 1.9 K, making it the coldest known place in the universe. Within the insertion points, the four detectors ATLAS [67], CMS [68], ALICE [69] and LHCb [70] are located.

The LHC is designed to reach a luminosity of $\mathscr{L} = 10^{34}\ \mathrm{cm}^{-2}\mathrm{s}^{-1}$. The luminosity is connected to the number of produced events via the cross-section σ of that process

$$N = \sigma \times \int_t \mathscr{L} \mathrm{dt}. \tag{3.1}$$

Here, the luminosity is integrated over the duration of the data collection period. The integrated luminosity is often stated as a measure of the particle current density. A record of the LHC's integrated luminosity for 2011 to 2018 can be found in Fig. 3.2.

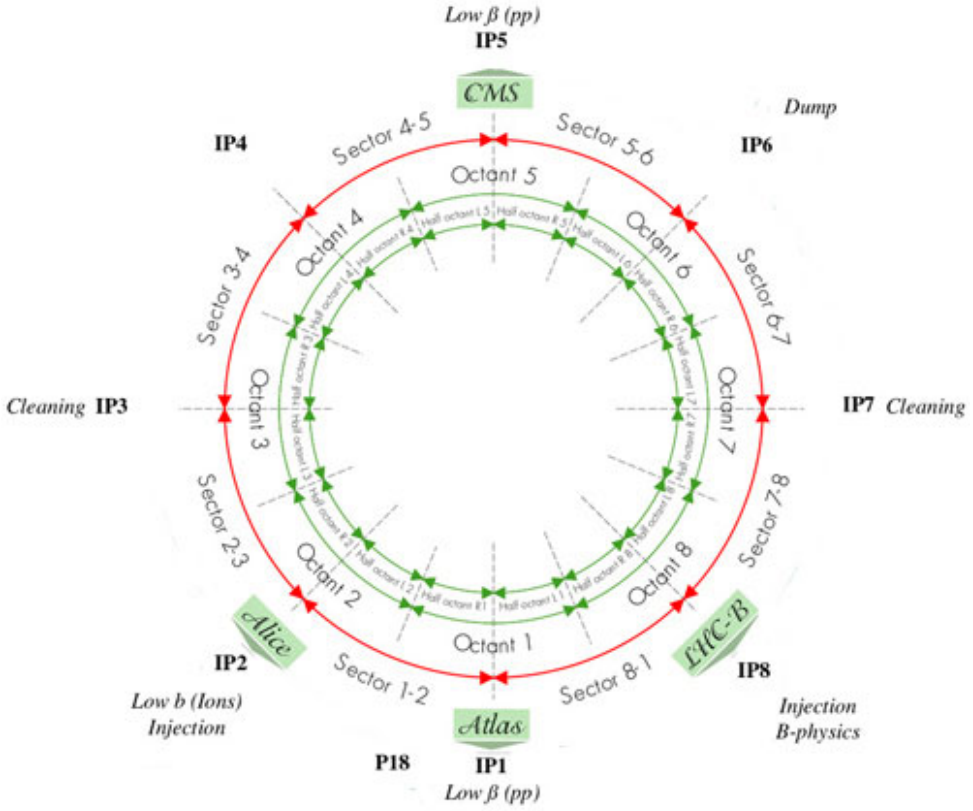

Figure 3.1.: A breakdown of the LHC collider ring. The ring consists of eight arcs and eight straight insertions. At the insertion points (IP), e.g. the experiments or the beam injection are located. The segments between two IPs are called sectors. Each sector is powered independently. © CERN

Protons are not directly inserted into the LHC; they are accelerated in several pre-accelerators, as shown in Fig 3.3. At first, the protons are produced by stripping off the electrons from hydrogen molecules using an electric field. Those protons are injected into the linear accelerator LINAC2, which accelerates them to energies of 50 MeV. After this, the protons are accelerated to 1.4 GeV by the Proton Synchrotron Booster (PSB). Then, the Proton Synchrotron (PS) accelerates them to 25 GeV, before the Super Proton Synchrotron raises the energy to 450 GeV, which is the last step before they get injected into the LHC.

3.2. The ATLAS Experiment

ATLAS [67] is one of the two multi-purpose detectors at the LHC, the other being CMS. As a multi-purpose detector it is designed to measure a wide variety of physics processes. With its 44 m length, the 25 m diameter and an overall weight of 7000 t, ATLAS is the largest detector in volume ever constructed for accelerator-based particle physics. ATLAS is a cylindrical detector,

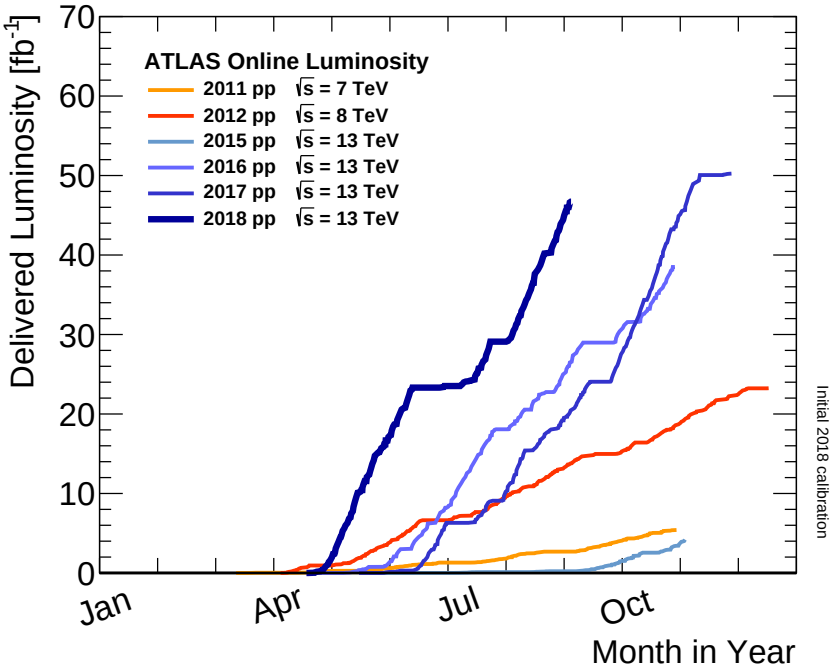

Figure 3.2.: The integrated luminosity delivered by the LHC in the years 2011 to 2018.

i.e. the detector parts are symmetrically wrapped around the beam line. The main components of the ATLAS detector are the *inner detector*, which is located directly around the beam pipe, the *calorimeter*, following the inner detector, the *muon spectrometer*, to detect muons that cannot be sufficiently measured in the other parts of the detector, and the *magnet system*, to bend the trajectories of charged particles. Fig 3.4 shows a drawing of ATLAS, with its main components labelled. Those components will be discussed further in the following.

The *inner detector* consists of three different components, namely the pixel detector, the semiconductor tracker (SCT) and the transition radiation tracker (TRT). The pixel detector consists overall of 92 million pixels to track the particles passing through it. This number includes the pixels of the insertable B-layer [71, 72]. A group of 46080 pixels, corresponding to an area of 10 cm^2, is called a module. The whole pixel detector is divided into three barrels, with 1744 modules each. A barrel consists of one tube stretching along the beam pipe, with 1456 modules on it, and one disk at each side that stretch into the transverse plane, with 288 modules each. The SCT is a silicon microstrip detector, built with 4088 two-sided modules and more than 6 million readout channels. It is divided into 4 cylindrical layers and 18 end-cap disks. The spacing of the readout channels is 80 μm, providing a precision of location measurement of up to 17 μm per layer. The TRT consists of 300000 straws. A straw is a tube with 4 mm in diameter. In its centre, there is a gold-plated tungsten wire with a diameter of 30 μm. The straws are filled with 70% Xe, 27% CO_2 and 3% O_2. The TRT is also divided into a barrel and

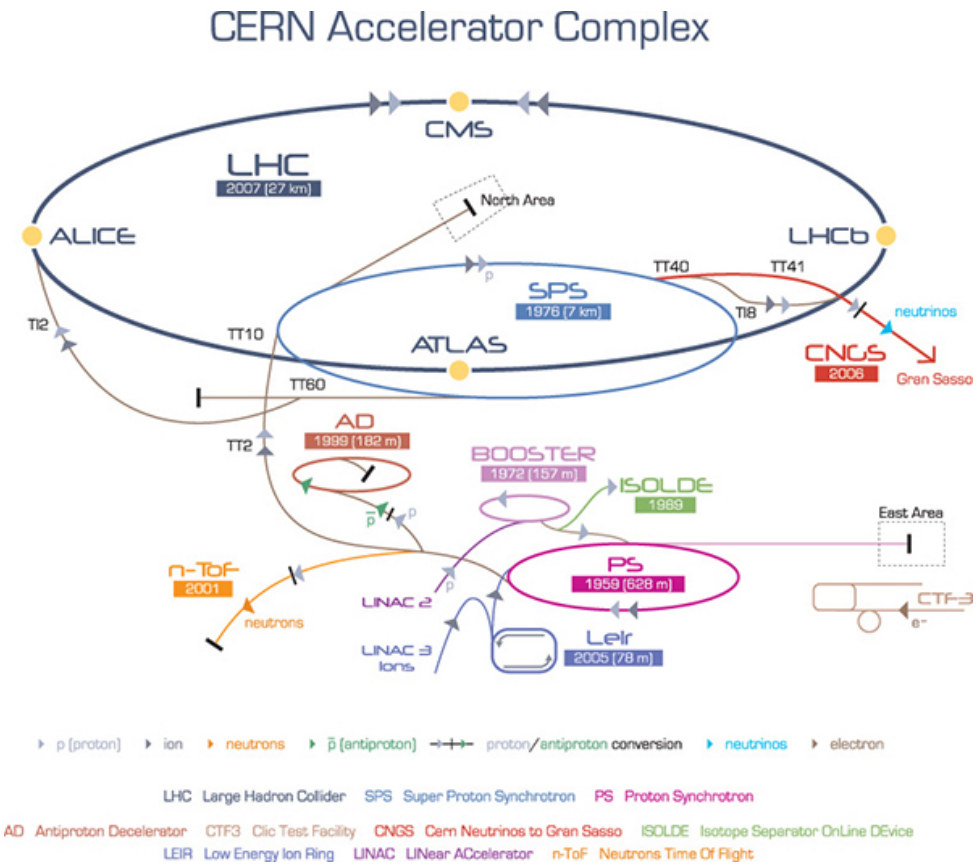

Figure 3.3.: The CERN accelerator complex. Aside from the main accelerator, the LHC, CERN has many other accelerators that are connected to the LHC. From the proton source to the injection into the LHC, the protons are accelerated in the LINAC2, the PS Booster, the PS, and the SPS. © CERN

two end-caps. The barrel region contains 50000 straws with a length of 144 cm each and the end-caps contain overall 250000 straws with a length of 39 cm each. Different types of particles can be discriminated here, as charged particles radiate when they pass the straws. Depending on their mass, the rate of radiation is different. By design the inner detector measures particles within $|\eta| < 2.5$ and with an uncertainty

$$\frac{\sigma_{p_T}}{p_T} = \sqrt{(0.05\%)^2 \times p_T^2 + (1\%)^2}. \tag{3.2}$$

The purpose of the *calorimeter* is to measure the energy of particles passing through it. A *calorimeter* measures the energy deposited in the material by the particle passing through, to infer its former energy. ATLAS has an electromagnetic (EM) calorimeter, to measure the energy of photons and electrons, and a hadronic calorimeter, to measure the energy of hadrons. Both are sampling calorimeters, i.e. they have a passive medium to trigger the radiation showers, e.g. lead, and an active medium to measure the energy. The liquid argon (LAr) *calorimeter*

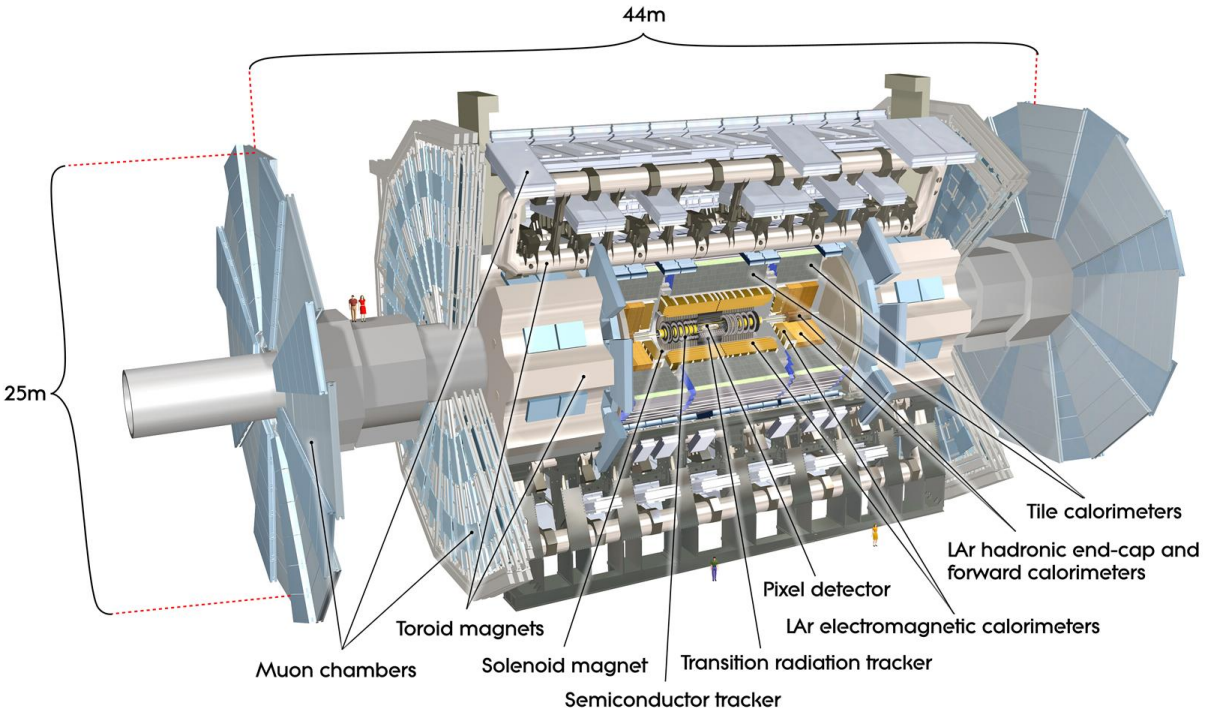

Figure 3.4.: A sketch of the ATLAS detector. Labelled are the main detector components, i.e. the inner detector, the calorimeters, the muon chamber, and the magnet system. Two people are shown, for the better understanding of the dimensions of the detector.
© CERN

has -183 °C cold liquid argon as its active material. The LAr end-caps consist of a forward calorimeter, electromagnetic end-caps and hadronic end-caps. Besides the LAr calorimeter, ATLAS has also a tile *calorimeter* (TileCal). It is a hadronic *calorimeter* with plastic scintillator tiles as its active medium. The resolution is given by

$$\frac{\sigma_E}{E} = \frac{a}{\sqrt{E}} \oplus b, \tag{3.3}$$

where (a,b) is $(10\%, 0.7\%)$ for the EM calorimeter, $(50\%, 3\%)$ for the hadronic calorimeter in the barrel and end-cap region, and $(100\%, 10\%)$ in the forward region, respectively.

According to the Bethe-Bloch formula [73], muons are minimal ionising particles. That means, they can pass the *inner detector* and the *calorimeter* undetected. The *muon spectrometer* is supposed to measure them, by using a collection of 4000 muon chambers. Those chambers make use of four different technologies. Thus, there are thin gap chambers, resistive plate chambers, monitored drift tubes and cathode strip chambers.

The *magnetic system* consists of three different parts, the central solenoid magnet, the barrel toroid and the end-cap toroids. The central solenoid is 5.3 m long, 2.4 m in diameter and 4.5 cm thick, weighing about 5 t. It produces a 2 T strong magnetic field to bend charged particles for the momentum measurement in the inner detector. The barrel toroid is 25.3 m long, 20.1 m in diameter and weighs 830 t. It is made out of eight separate coils, that produce an overall 4 T strong magnetic field. The end-cap toroids have a length of 5 m, a diameter of 10.7 m and a weight of 240 t . It creates a magnetic field of 4 T. Both toroids are operated at 4.7 K.

The high luminosity of the LHC creates a huge number of events per second, more than possibly recordable (60 TB/s). Moreover, only a small number of those events will yield information important for physics analyses. Thus, a *trigger system* is used, to sort out those events. The *trigger system* is divided into two levels. The *level-1* trigger uses information of the *calorimeter* and the muon spectrometer. Out of 40 million bunch crossings per second, only 100000 are accepted and passed to the *level-2* trigger. The number of events per second passing this trigger level is in the order of 1000.

3.2.1. The ATLAS Coordinate System

When protons collide within the LHC, the point of interaction defines the origin of a coordinate system. The z-axis of that system points along the beam direction. In Cartesian coordinates, the x-axis points towards the centre of the LHC ring and the y-axis points upwards. The latter two axes define the transverse plane. Neutrinos cannot be measured with the detectors, they can only be partially reconstructed using the missing transverse energy $\not{E}_T$ and only if there is only one neutrino in the FS. That is the difference between the initial momentum of the interacting particle in the transverse plane and the measured momenta in the transverse plane. As the initial transverse momentum of the partons interacting is known to be approximately zero, the transverse component can be reconstructed, while the longitudinal cannot be reconstructed.

Because of the cylindrical shape of the detectors, the use of cylindrical coordinates is common, using the transverse distance from the beamline r and the azimuthal angle ϕ. By taking the high energy limit of the rapidity y, the pseudo-rapidity η can be defined as

$$y \approx \eta = \frac{1}{2} \ln \left(\frac{|p| + p_L}{|p| - p_L} \right), \tag{3.4}$$

with the longitudinal component of the particle momentum p_L. Using η, the angle θ between the momentum vector of a particle and the z-axis can be calculated

$$\theta = 2 \arctan \left(e^{-\eta} \right). \tag{3.5}$$

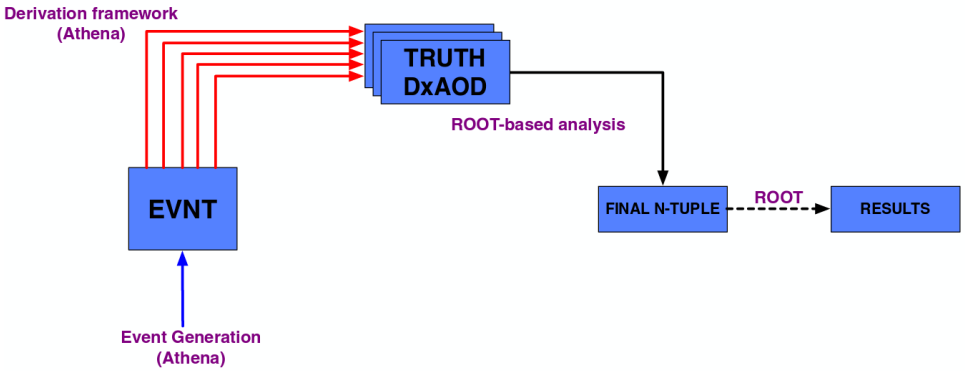

Figure 3.5.: The scheme of this analysis.

This relation between η and the angle θ is the reason why the pseudo-rapidity is preferred over the rapidity; it is much more easily accessible. The distance between two objects in the $\eta - \phi$ plane is defined as

$$\Delta R = \sqrt{\Delta\phi^2 + \Delta\eta^2}. \tag{3.6}$$

3.2.2. Computing in ATLAS

ATLAS disposes of a large collection of offline software, usable for simulations, reconstructions of data, and analyses. Many analysis-groups in ATLAS have their own frameworks and packages for data analysis. To process large amounts of data or to do elaborate simulations the Worldwide LHC Computing Grid [74], or just Grid, is used. The Grid is a global effort of more than 170 computing centres in 42 countries across the world. This makes the storage, distribution, and analysis of the enormous amounts of data produced at the LHC possible. For smaller computing efforts, CERN provides a cluster of computers, called Lxplus, to which every CERN member can connect. Fig. 3.5 shows a simplified version of a typical analysis scheme in ATLAS, which will be the analysis scheme of the analysis presented in this thesis. At first the MC generator produces events in the so-called *EVNT* format, which is then transformed into *TRUTH DxAOD*, as it is more convenient for the following analysis. Both is done with an ATLAS framework called *Athena* [75]. A following analysis based on *ROOT* [76] makes the event selection, reconstructs the observables, and plots them.

4. Monte Carlo Generators in High Energy Physics

The purpose of Monte Carlo (MC) generators is to provide the theoretical predictions of arbitrary observable distributions. Since the generation of events involves the modelling of non-perturbative effects, it is not possible to use purely theoretical predictions. The use of MC generators is very common in high energy physics, for example for designing experiments and detectors. For this reason, the general concept of MC generators is explained in Sec. 4.1. The MC generator used for this study will be presented in Sec. 4.2.

4.1. General Mechanics of Monte Carlo Generators

In this section, the general workflow of MC generators will be discussed. At first, the basic simulation of the underlying hard parton level process of an event will be explained in Sec. 4.1.1. After that, real and virtual radiations are added to the partons in Sec. 4.1.2. Ultimately, common models of hadronisation will be discussed in Sec. 4.1.3.

4.1.1. Simulation of Hard Processes

The differential cross-section $\mathrm{d}\sigma$ of an underlying hard process, e.g. $gg \to t\bar{t}$, can always be described as:

$$\mathrm{d}\sigma \propto |\mathscr{M}|^2 \mathrm{dLIPS}, \tag{4.1}$$

where $\mathscr{M}$ is the matrix element of that process and the Lorentz invariant phase space (LIPS). The phase space covers all degrees of freedom of that process, for example $-1 < \cos\theta < 1$ or $0 < \phi < 2\pi$. The differential cross-sections are also called *event weights*. To calculate the cross-section σ of the process, Eq. 4.1 has to be integrated. Even if the integral can be calculated analytically, the result would be the cross-section, whereas MC generators can generate histograms with entries corresponding to events. The resulting distribution corresponds to the cross-section depending on the corresponding phase space points. For this, the phase space is

sampled, i.e. a random number is generated, which is flatly distributed in the phase space, representing an n-tuple of phase space parameters. Those parameters define an event. The average $\langle \mathrm{d}\sigma \rangle$ of many $\mathrm{d}\sigma$, calculated with the generated parameters and Eq. 4.1, converges to

$$\langle \mathrm{d}\sigma \rangle \to \int \mathrm{d}\sigma = \sigma. \tag{4.2}$$

However, the generated distribution is unphysical, as the random numbers follow a uniform distribution in phase space. There are two approaches to create physical distributions. Depending on the used approach, one distinguishes between *cross-section integrators* and *event generators*. Within a *cross-section integrator*, histograms are filled with the *event weights*. In the large number limit, the resulting distribution approaches the actually predicted one. The individual entries, however, do not correspond to anything physical. It is thus not a proper simulation of a real event.

Event generators use the approach of unweighting the events. This way, each event, corresponding to a certain subset of the phase space, appears as often as the theory predicts it. A common technique for unweighting is the *hit-and-miss* technique. For this technique, the maximum $\mathrm{d}\sigma_{\mathrm{max}}$ of Eq. 4.1 is needed. In some cases it can be calculated analytically, in less simple cases the whole phase space needs to be scanned. A generated event is only accepted if the condition

$$\frac{\mathrm{d}\sigma}{\mathrm{d}\sigma_{\mathrm{max}}} > g \tag{4.3}$$

is satisfied. In this case, g is a uniformly distributed random number in the interval $(0,1)$. This way, the probability of an event to be accepted is linked to its theoretical probability to appear. An event with a maximal *event weight* will always be accepted and an event with $\mathrm{d}\sigma = 0$ will always be rejected. This creates a distribution equal to the distribution predicted by theory and all entries of the histograms correspond to actual events. Therefore, *event generators* can be used for a real simulation of an experiment.

4.1.2. Generation of Parton Showers

There are two main reasons for applying parton shower algorithms to the parton events introduced in Sec. 4.1.1. First, they are needed to reliably estimate the higher-order effects in singular phase space regions, i.e. collinear splitting or soft gluon emission. The problem of adding next-to-leading order (NLO) contributions are singularities caused by the additional terms, which can not be handled by numerical algorithms, thus they have to be dealt with in another way. Secondly, they provide a final state with a large number of partons. This is needed to apply hadronisation algorithms to receive physical results. Hadronisation will be discussed

in Sec. 4.1.3.

A parton shower algorithm starts from the event configuration given in Sec. 4.1.1 and evolves the external lines further, by creating branchings. A branching is a splitting of one parton into two others. Possible branchings are

$$\overline{q} \to \overline{q}g, \qquad g \to gg \quad \text{and} \quad g \to q\overline{q}. \tag{4.4}$$

Other than the partonic event, described in Sec. 4.1.1, a parton shower cannot be rejected. All events that are accepted by the unweighting algorithm are also showered.

A parton shower is modelled as a Markov process. That means, the further development of a state is only dependent on the current state and not on any previous states. For each branching it calculates a new value of the evolution parameter t, the momentum fraction z and the azimuthal angle ϕ. The evolution parameter starts at a high value T and usually corresponds to a value characteristic of the process. In PYTHIA [77, 78], t can for example be the virtuality of the parton, i.e. the difference between its mass and its pole mass. The next value of t is calculated by solving the equation

$$\Delta_i(T,t_0) = \mathscr{R}\Delta_i(t,t_0). \tag{4.5}$$

In this equation, $\mathscr{R}$ is a random number in the interval $[0,1]$, t_0 is an infra-red cut-off parameter, usually around 1 GeV, and

$$\Delta_i(T,t_0) = \exp\left[-\sum_j \int_{t_0}^{T} \frac{\mathrm{d}t}{t} \int_0^1 \mathrm{d}z \mathscr{P}_{ji}(z,t,t_0)\right] \tag{4.6}$$

is the *Sudakov form factor* [79] for the flavour of the particle i. Here, $\mathscr{P}_{ji}$ is the probability distribution function (PDF) for a parton i splitting into a parton j. Although

$$\mathscr{P}_{ji} = \frac{\alpha_S}{2\pi} P_{ji}, \tag{4.7}$$

with the DGLAP splitting function P_{ji} [80–82] could be used, the PDF is often modified to fit the exact implementation of the parton shower algorithm. If the condition $t \leq t_0$ is satisfied, the showering of that parton ends.

In general, Eq. (4.5) cannot be solved analytically. A numerical method to solve it is the *rejection method*. In the first step, an upper bound $\mathscr{P}'_{ji}$ for all $\mathscr{P}_{ji}$, for which Eq. 4.5 can still be solved, is calculated. Using this upper bound, a new value t' is calculated. As the upper bound is used, t' will on average be too high. To correct for this, each t' is only accepted with a probability $\mathscr{P}_{ji}/\mathscr{P}'_{ji}$. If a value is rejected, a new value is calculated with t' instead of T. This will be repeated until the value is accepted or falls below t_0. In case of multiple branching

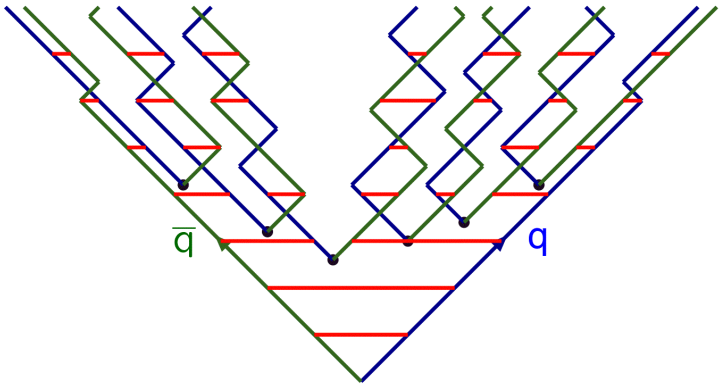

Figure 4.1.: The hadronisation of a pair of quarks according to the string model. Time flows upwards within the picture, the horizontal axis is a measure of distance. The colour strings (horizontal) between the quark q and the antiquark $\bar{q}$ stretches until it breaks (black dot) and an additional quark-antiquark pair is created. In the end, seven hadrons have formed.

options, t' is calculated for all branchings and only the branching with the highest t' is chosen.

The new value of the momentum fraction is calculated by solving

$$\int_0^z \mathrm{d}z' \mathscr{P}_{ji}(z',t,t_0) = \mathscr{R}' \int_0^1 \mathrm{d}z' \mathscr{P}_{ji}(z',t,t_0), \tag{4.8}$$

where $\mathscr{R}'$ is another random number between zero and one. This equation can also be solved by the *rejection method*. There are different ways for determining ϕ. A simple approach is to use a value randomly picked from a uniform distribution. Alternatively, the correct azimuthal correlations between the branchings can be implemented.

It is important, not to pass the calculated value t directly to both new partons as the starting value T. In PYTHIA, for example, this would result in two daughter partons with possible virtualities arbitrarily close to the mother parton's virtuality. This is forbidden, due to energy conservation. In a branching $i \to jk$, the following evolution parameters are restricted by the condition

$$\sqrt{t_j} + \sqrt{t_k} < \sqrt{t_i}. \tag{4.9}$$

4.1.3. Hadronisation

To turn the generated parton final state into a hadronic final state, hadronisation algorithms are used. They typically follow two hadronisation models, the string model [83, 84] of PYTHIA or the cluster model [85, 86], implemented in HERWIG [87, 88]. The key difference between those two models is that the string model turns the partons directly into hadrons, while the cluster model sorts the partons into clusters first and decays them into hadrons after that.

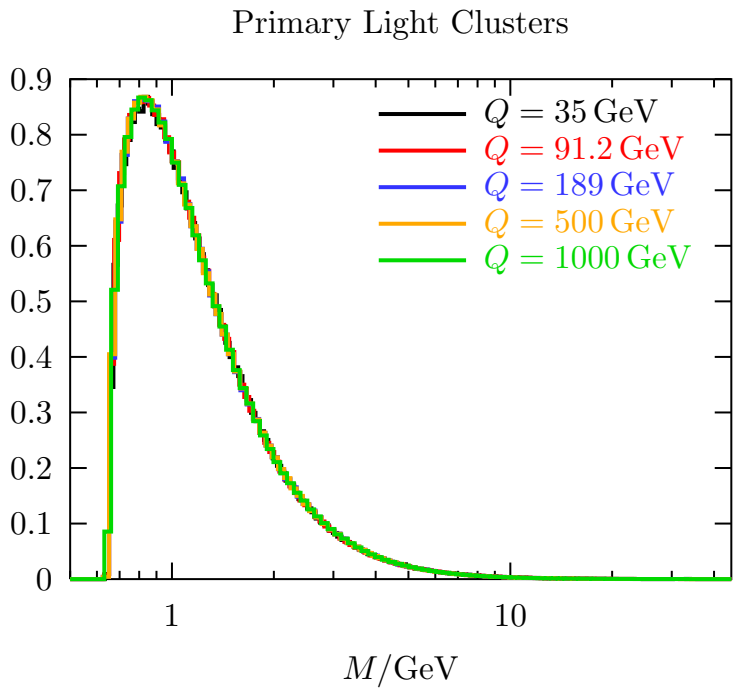

Figure 4.2.: Mass distribution of clusters in HERWIG for different Q and $t_0 \approx 1$ GeV.

String Hadronisation The concept of confined quarks was already introduced in Sec. 2.1.3. It is the basis of the string hadronisation model and thus will be reintroduced in this section, in a bit more detail. A quark-antiquark pair is linearly confined via colour strings [83, 89], linking them to each other. This results in a potential [90]

$$V(r) = \kappa r \tag{4.10}$$

linearly dependent on the distance r between the two quarks. The string constant κ is approximately 0.2 GeV^2, measured in hadron mass spectroscopy [91]. It corresponds to the energy saved in the colour strings per unit of distance. In addition, the potential has also a term proportional to $1/r$ that dominates for close distances, but it is assumed to be negligible for this model. When the quarks diverge, the potential energy saved in the colour strings between them increases and, eventually, the colour strings will break, producing a new pair of quarks. This process is repeated until no quarks have enough energy to hadronise anymore. In Fig. 4.1, the quark and the antiquark are connected via a colour string. The colour string breaks six times until each quark and the neighbouring antiquarks form hadrons.

Cluster Hadronisation The basis of the cluster hadronisation model is the so-called preconfinement [92]. A parton shower at an arbitrary cut-off scale t_0, see Sec. 4.1.2, can always be divided into several colour singlet combinations. Those so-called clusters have a universal

mass distribution, i.e. they are only dependent on t_0, but not on the event momentum transfer Q or the event type. Fig. 4.2 shows a comparison of multiple mass distribution in HERWIG at different Q, which supports the universality of the mass distribution.

At t_0, all gluons within the parton shower are forced to split into a quark-antiquark pair, to be able to form meson clusters. Those clusters can be treated as excited meson states decaying into unexcited meson states, according to the probabilities for each allowed two-body decay.

4.2. The $b\bar{b}4\ell$ Generator

4.2.1. NLO Calculations in MC generators

In this section, the NLO computations within a MC generator are explained, following the example of a hard $2 \to n$ scattering. Starting from momentum conservation, the equation

$$\underbrace{x_\oplus P_\oplus}_{p_\oplus} + \underbrace{x_\ominus P_\ominus}_{p_\ominus} = \sum_i^n p_i \tag{4.11}$$

must hold, where p_i are the momenta of the n outgoing particles, $P_\oplus$ and $P_\ominus$ are the momenta of the incoming hadrons, and $x_\oplus$ and $x_\ominus$ are the Bjorken-x of the interacting partons from the corresponding hadrons. The latter can be summarised as the momenta of the interacting partons $p_\oplus$ and $p_\ominus$. The phase space of this process is

$$\Phi_n = \{x_\oplus, x_\ominus, p_1, \ldots, p_n\}, \tag{4.12}$$

with the differential

$$\mathrm{d}\Phi_n = \mathrm{d}x_\oplus \mathrm{d}x_\ominus \mathrm{d}\varphi_n(p_\oplus + p_\ominus, p_1, \ldots, p_n). \tag{4.13}$$

Using the luminosity $\mathscr{L}(x_\oplus, x_\ominus)$ depending on the energy of the interacting particles, the cross-section σ_{LO} at LO can be calculated as

$$\sigma_{\mathrm{LO}} = \int \mathrm{d}\Phi_n \mathscr{L} \mathscr{B}(\Phi_n), \tag{4.14}$$

with the squared matrix element of all considerable processes $\mathscr{B}$. The letter $\mathscr{B}$ is chosen in reference to the Born approximation [93], which is why it is called the Born term.

In NLO calculations, a real term $\mathscr{R}$ and a virtual term $\mathscr{V}_b$ are added to the Born term. The index b means *bare* and indicates that the virtual term still includes infra-red divergences. The real term describes the scattering as a $2 \to n+1$ process, including a real radiation, with phase

space

$$\Phi_{n+1} = \{\Phi_n, p_{n+1}\}. \tag{4.15}$$

The virtual term includes loop diagrams. These three terms are the main components of the NLO cross-section. Specifically in hadronic interactions, remnant terms $\mathscr{G}_{\oplus,b}$ and $\mathscr{G}_{\ominus,b}$ must be added, accounting for collinear partons with a fraction of momentum of $(1-z)$ in the initial state (ISC). Therefore, the cross-section at NLO is

$$\begin{aligned}\sigma_{\text{NLO}} = &\int \mathrm{d}\Phi_n \mathscr{L}\left[\mathscr{B}(\Phi_n) + \mathscr{V}(\Phi_n)\right] + \int \mathrm{d}\Phi_{n+1}\mathscr{L}\mathscr{R}(\Phi_{n+1}) \\ &+ \int \mathrm{d}\Phi_{n,\oplus}\mathscr{L}\mathscr{G}_{\oplus,b}(\Phi_{n,\oplus}) + \int \mathrm{d}\Phi_{n,\ominus}\mathscr{L}\mathscr{G}_{\ominus,b}(\Phi_{n,\ominus}).\end{aligned} \tag{4.16}$$

The phase space $\Phi_{n,\oplus} = \{x_\oplus, x_\ominus, z, p_1, \ldots, p_n\}$ is defined with the condition

$$z p_\oplus + p_\ominus = \sum_i^n p_i. \tag{4.17}$$

$\Phi_{n,\ominus}$ is defined analogously. The expectation value $\langle O \rangle$ of any observable O without infra-red divergences, can then be calculated as

$$\begin{aligned}\langle O \rangle = &\int \mathrm{d}\Phi_n \mathscr{L} O_n(\Phi_n)\left[\mathscr{B}(\Phi_n) + \mathscr{V}(\Phi_n)\right] + \int \mathrm{d}\Phi_{n+1}\mathscr{L}O_{n+1}(\Phi_{n+1})\mathscr{R}(\Phi_{n+1}) \\ &+ \int \mathrm{d}\Phi_{n,\oplus}\mathscr{L}O_n(\Phi_{n,\oplus})\mathscr{G}_{\oplus,b}(\Phi_{n,\oplus}) + \int \mathrm{d}\Phi_{n,\ominus}\mathscr{L}O_n(\Phi_{n,\ominus})\mathscr{G}_{\ominus,b}(\Phi_{n,\ominus}).\end{aligned} \tag{4.18}$$

As the integrals still contain divergences, they cannot be calculated numerically. To remove the divergences, a subtraction method [94] can be applied.

Basic Formulation of Subtraction techniques

All subtraction methods use so-called *counter* terms $\mathscr{C}^{(\alpha)}$. There is one *counter* term for each singular region α, i.e. two partons becoming collinear or a soft radiation. For all singular regions a *mapping* $M^{(\alpha)}$ is defined. The *mapping* transforms Φ_{n+1} into a singular configuration

$$\tilde{\Phi}^{(\alpha)}_{n+1} = M^{(\alpha)}(\Phi_{n+1}). \tag{4.19}$$

Singular regions can be divided into three different cases. In case α corresponds to a soft radiation, $\tilde{\Phi}^{(\alpha)}_{n+1}$ includes a final state (FS) parton with a momentum equal to zero. If α corresponds to collinear partons in the final state (FSC), the *mapping* will produce two massless partons in the FS, with parallel trajectories. In case of ISC, the mapped IS includes a massless parton parallel to one incoming parton. At the singular point, the singular configuration is equal to Φ_{n+1}.

All singular configurations have an underlying Born configuration $\bar{\Phi}_n^{(\alpha)}$, including only n partons in the final state. To obtain the underlying Born configuration of a soft radiation, the parton with momentum equal to zero is deleted, as it does not contribute to the event kinematics. In case of FSC, the two parallel partons are merged to an effective parton with a momentum that is the sum of the collinear partons' momenta. If the singular region is a ISC, the massless collinear parton is removed and the IS partons' momentum is set to the value after the radiation. This way, the underlying Born configuration consists only of resolvable partons, whereas the singular configurations include unresolvable partons as well. Using this, *emission factorisation* can be applied to the original phase space:

$$\Phi_{n+1} = \{\bar{\Phi}_n^{(\alpha)}, \Phi_{\text{rad}}^{(\alpha)}\} \quad \text{and} \quad \mathrm{d}\Phi_{n+1} = \mathrm{d}\bar{\Phi}_n^{(\alpha)} \mathrm{d}\Phi_{\text{rad}}^{(\alpha)}. \tag{4.20}$$

This can be applied to the real term of the NLO expectation value of O

$$\begin{aligned} \int \mathrm{d}\Phi_{n+1} \mathscr{L} O_{n+1}(\Phi_{n+1}) \mathscr{R}(\Phi_{n+1}) &= \sum_\alpha \int \mathrm{d}\Phi_{n+1} \left[\tilde{\mathscr{L}} O_n(\bar{\Phi}_n) \mathscr{C}(\Phi_{n+1})\right]_\alpha \\ &+ \int \mathrm{d}\Phi_{n+1} \left(\mathscr{L} O_{n+1}(\Phi_{n+1}) \mathscr{R}(\Phi_{n+1}) - \sum_\alpha \left[\tilde{\mathscr{L}} O_n(\bar{\Phi}_n) \mathscr{C}(\Phi_{n+1})\right]_\alpha \right), \end{aligned} \tag{4.21}$$

where an effective zero was added. An α in the index of brackets denotes that α is the implicit index of all variables in that bracket, to which it is applicable. Also, the *counter* terms depending on Φ_{n+1} can be transformed to

$$\bar{\mathscr{C}}(\bar{\Phi}_n) = \int \mathrm{d}\Phi_{rad} \mathscr{C}(\Phi_{n+1}) \tag{4.22}$$

and

$$\bar{\mathscr{C}}(\bar{\Phi}_n, z) = \int \mathrm{d}\Phi_{rad} \mathscr{C}(\Phi_{n+1}) z \delta\left(z - \frac{\bar{x}_\oplus}{\tilde{x}_\oplus}\right) \tag{4.23}$$

for soft radiation, FSC (Eq. (4.22)) and ISC (Eq. (4.23)), respectively. Although Eq. (4.23) is shown for $x_\oplus$, it can also be shown with $x_\ominus$ depending on the singular region. Those two cases must be differentiated, because of the different underlying Born configurations. In case of soft radiations and FSC, x is the same in the singular configuration and the Born configuration. But in case of ISC, x is different in those two configurations. As a consequence, $\bar{\mathscr{L}} \neq \tilde{\mathscr{L}}$ generally holds in that case. However, it will prove important that the luminosity can be factored out of the integral over $\mathrm{d}\Phi_{rad}$, which would not be possible if Eq. 4.22 were applied to ISC singular regions. Thus, the delta distribution is used. The argument of $\bar{\mathscr{C}}$ in Eq. (4.23) defines a new phase space, if z is included into the set of parameters of $\bar{\Phi}_n$. This new phase space can be

identified with $\Phi_{n,\oplus}$, introduced in Eq. 4.16. It follows that

$$\mathrm{d}\Phi_{n,\oplus} = \mathrm{d}\bar{\Phi}_n \frac{\mathrm{d}z}{z}. \tag{4.24}$$

Furthermore, the *bare* remnant terms in Eq. 4.16 can be contracted with the *counter* terms defined in Eq. (4.23), resulting in infra-red safe remnant terms and an additive divergent term. However, the sum of the divergent terms, resulting from both *bare* remnant terms, and the *counter* terms defined in Eq. (4.22) cancel with the divergences of the *bare* virtual term. Taking that into account, Eq. (4.18) becomes

$$\begin{aligned}\langle O\rangle = &\int \mathrm{d}\Phi_n O_n(\Phi_n)\left[B(\Phi_n)+V(\Phi_n)\right] \\ &+ \int \mathrm{d}\Phi_{n+1}\left(O_{n+1}(\Phi_{n+1})R(\Phi_{n+1}) - \sum_\alpha \left[O_n(\bar{\Phi}_n)C(\Phi_{n+1})\right]_\alpha\right) \\ &+ \int \mathrm{d}\Phi_{n,\oplus} O_n(\bar{\Phi}_n) G_\oplus(\Phi_{n,\oplus}) + \int \mathrm{d}\Phi_{n,\ominus} O_n(\bar{\Phi}_n) G_\ominus(\Phi_{n,\ominus})\end{aligned} \tag{4.25}$$

In this equation, the variables R, C, G, B and V are the products of the luminosity and the corresponding scripted letter. In conclusion, this expression of $\langle O\rangle$ is finite and can be numerically integrated.

4.2.2. The POWHEG Method and Framework

The POWHEG (Positive Weight Hardest Emission Generator) method [95] was proposed as an alternative to MC@NLO [96] to implement an NLO parton shower generator. MC@NLO produces also events with negative weights, i.e. cross-section differentials. POWHEG was supposed to avoid that. The POWHEG method starts by introducing a new function

$$\begin{aligned}\bar{B}(\Phi_n) = B(\Phi_n) + V(\Phi_n) + \int \mathrm{d}\Phi_{\mathrm{rad}}[R(\Phi_{n+1}) - C(\Phi_{n+1})] \\ + \int \frac{\mathrm{d}z}{z}[G_\oplus(\Phi_{n,\oplus}) + G_\ominus(\Phi_{n,\ominus})]\end{aligned} \tag{4.26}$$

summarising parts of Eq. (4.25) using Eq. (4.20) and Eq. (4.24). Additionally, flavour structures f_b are introduced to record the flavours of all IS and FS partons. Two flavour structures differing only in the order of the appearing flavours in the FS count as equal. They will be used to further differentiate the cross-section contributions. This is necessary, as different events have different flavour structures. In addition, the real term of the cross-section is split into multiple parts according to the number of different singular regions α. Each part of the real term is then only

singular in one singular region α_r. This way,

$$R = \sum_{\alpha_r} R^{\alpha_r} \tag{4.27}$$

holds. The *counter* terms are separated analogously. Using this, Eq. (4.26) can be rewritten as

$$\begin{aligned}\bar{B}^{f_b}(\Phi_n) = [B(\Phi_n) + V(\Phi_n)]_{f_b} + \sum_{\alpha_r} \int [\mathrm{d}\Phi_{\mathrm{rad}}[R(\Phi_{n+1}) - C(\Phi_{n+1})]]_{\alpha_r} \\ + \sum_{\alpha_\oplus} \int \frac{\mathrm{d}z}{z} G_\oplus(\Phi_{n,\oplus}) + \sum_{\alpha_\ominus} \int \frac{\mathrm{d}z}{z} G_\ominus(\Phi_{n,\ominus}),\end{aligned} \tag{4.28}$$

where $\alpha_\oplus$ and $\alpha_\ominus$ are running over the singular regions for the remnant terms. In consequence, Eq. (4.25) can now be written as

$$\begin{aligned}\langle O \rangle = \sum_{f_b} \int \mathrm{d}\Phi_n O_n(\Phi_n) \bar{B}^{f_b}(\Phi_n) \\ + \sum_{\alpha_r} \left[\int \mathrm{d}\bar{\Phi}_n \mathrm{d}\Phi_{\mathrm{rad}} R(\Phi_{n+1}) (O_{n+1}(\Phi_{n+1}) - O_n(\bar{\Phi}_n)) \right]_{\alpha_r}.\end{aligned} \tag{4.29}$$

The *Sudakov form factor*, introduced in Sec. 4.1.2, is

$$\Delta^{f_b}(\Phi_n, p_T) = \exp\left(-\sum_{\alpha_r} \int \frac{[\mathrm{d}\Phi_{\mathrm{rad}} R(\Phi_{n+1}) \theta(p_T(\Phi_{n+1}) - p_T)]_{\alpha_r}}{B^{f_b}(\Phi_n)} \right). \tag{4.30}$$

Thus, the formula for the POWHEG *event weight* can be written as

$$\begin{aligned}\mathrm{d}\sigma = \sum_{f_b} \bar{B}^{f_b}(\Phi_n) \mathrm{d}\Phi_n \Bigg(\Delta^{f_b}(\Phi_n, p_T^{\min}) \\ + \sum_{\alpha_r} \frac{\left[\mathrm{d}\Phi_{\mathrm{rad}} R(\Phi_{n+1}) \theta(p_T(\Phi_{n+1}) - p_T^{\min}) \Delta^{f_b}(\Phi_n, p_T(\Phi_{n+1})) \right]_{\alpha_r}}{B^{f_b}(\Phi_n)} \Bigg)\end{aligned} \tag{4.31}$$

The POWHEG method uses a p_T ordered algorithm, thus the evolution parameter and the cut-off parameter defined in Sec. 4.1.2 are p_T and $p_T^{\min}$, respectively.

4.2.3. The POWHEG-BOX-RES Framework

The POWHEG-BOX [97, 98] was developed as a framework that implements the POWHEG method. Within POWHEG-BOX, the resulting FS partons from POWHEG can be interfaced to shower MC programs, such as PYTHIA, via the *Les Houches Event* (LHE) interface [99].

To generate events, a new function is defined, called $\tilde{B}$. $\tilde{B}$ depends on the radiation phase

space Φ_{rad} that is parametrised as

$$X_{\text{rad}} = \{X^1_{\text{rad}}, X^2_{\text{rad}}, X^3_{\text{rad}}\}. \tag{4.32}$$

Furthermore, z is parametrised by X^1_{rad} between zero and one. Applying this parametrisation to Eq. (4.28) yields

$$\begin{aligned}\tilde{B}^{f_b}(\Phi_n, X_{\text{rad}}) = [B(\Phi_n) + V(\Phi_n)]_{f_b} + \sum_{\alpha_r} \left[\left| \frac{\partial \Phi_{\text{rad}}}{\partial X_{\text{rad}}} \right| [R(\Phi_{n+1}) - C(\Phi_{n+1})] \right]_{\alpha_r} \\ + \sum_{\alpha_\oplus} \frac{1}{z} \left| \frac{\partial z}{\partial X^1_{\text{rad}}} \right| G_\oplus(\Phi_{n,\oplus}) + \sum_{\alpha_\ominus} \frac{1}{z} \left| \frac{\partial z}{\partial X^1_{\text{rad}}} \right| G_\ominus(\Phi_{n,\ominus}),\end{aligned} \tag{4.33}$$

and

$$\tilde{B}(\Phi_n, X_{\text{rad}}) = \sum_{f_b} \tilde{B}^{f_b}(\Phi_n, X_{\text{rad}}). \tag{4.34}$$

$\tilde{B}$ can then be integrated over the full phase space to get the Born level cross-section. It is also the subject to the unweighting via the *hit-and-miss* technique described in Sec. 4.1.1.

The POWHEG-BOX-RES framework is the latest extension of POWHEG-BOX. Its name originates from the so-called *resonance aware* subtraction method [100], used in this framework.

Resonance Aware Subtraction When mapping the singular regions to the underlying Born configuration, many frameworks can be used. A commonly used framework is the Catani-Seymour [101] framework. Assuming a singular region, where a b-quark emits a gluon collinearly, the momentum $\bar{p}_b$ of the merged parton is

$$\bar{p}_b = p_b + p_g - p_\oplus \frac{(p_b + p_g)^2}{2(p_b + p_g)p_\oplus}, \tag{4.35}$$

with the momentum of the initial state parton. This is done to preserve the mass of the b-quark. The initial state particle's momentum is thus

$$\bar{p}_\oplus = p_\oplus - p_\oplus \frac{(p_b + p_g)^2}{2(p_b + p_g)p_\oplus}. \tag{4.36}$$

Hence, the mass of the resonance connecting the radiating b-quark and the initial state particle must have changed. This change in its virtuality, i.e. the difference between its mass and its pole mass, is approximately

$$\Delta m \approx \frac{m^2_{bg}}{E_{bg}}. \tag{4.37}$$

This does not pose a problem as long as

$$m_{bg}^2 \ll \Gamma_{\text{res}} E_{bg} \tag{4.38}$$

holds, where Γ_{res} is the width of the resonance. But many generators assume $\Gamma_{\text{res}} \ll 1$, because in this case the cross-section can be factorised into production and decay terms. Aside from this problem, the matching of partons corresponding to a singular region has to be revised. In Eq. (4.30), the *Sudakov form factor* contains the ratio R/B. If two collinear partons are merged that do not come from the same resonance decay, B might be far off-shell, while R will still be on-shell. In consequence, the ratio will be very large. This violates the collinear approximation done within the *mapping* in Eq. 4.19.

The *resonance aware* subtraction method solves this problem by defining a *mapping* that conserves the masses of intermediate resonances. It also demands all collinear partons that are being merged to originate from the same resonance decay. This way, the ratio R/B should always be close to one.

The amplitudes for all tree and one-loop diagrams are based on OpenLoops [102] combined with COLLIER [103] or OpenLoops with CutTools [104] and OneLOop [105].

4.2.4. Implementation of the $b\bar{b}4\ell$ Process

The $b\bar{b}4\ell$ generator [106] is implemented in the POWHEG-BOX-RES framework. It generates events based on all Feynman diagrams with a final state (FS) $\ell^+ \nu_\ell l^- \bar{\nu}_l b\bar{b}$ in proton-proton collisions at NLO QCD. Furthermore, it uses the so-called four flavour number scheme (4FNS), which treats the b-quark as a massive particle and thus makes new phase space regions accessible, i.e. gluon splitting into two b-quarks. It also implements exact spin correlations for the first time, exact off-shell $t\bar{t}$ effects, as well as tW and non-resonant effects. A multiple radiation scheme is also implemented, where the hardest radiation of all decaying resonances in the event can be generated by POWHEG with matrix elements. In the single radiation scheme, only one hardest emission is generated that way and all remaining radiations are generated by the parton shower generator. Thus, it is clearly the most precise implementation of theoretical predictions currently available.

In this thesis, this generator will be compared to the standard generator in ATLAS namely the *hvq* generator [107] implemented in POWHEG-BOX. Also, the *ttb_NLO_dec* generator [108] implemented in POWHEG-BOX-V2, the second extension of POWHEG-BOX, will be briefly introduced in this section. It is another generator with NLO precision in decay. Their technical properties can be found in Tab. 4.1.

The *hvq* generator includes only NLO matrix elements in the production of $t\bar{t}$. On the other

generator	*hvq*	*ttb_NLO_dec*	$b\bar{b}4\ell$
framework	POWHEG-BOX	POWHEG-BOX-V2	POWHEG-BOX-RES
NLO matrix elements	$t\bar{t}$	$t(\to \ell^+\nu_\ell b)\,\bar{t}(\to l^-\bar{\nu}_l\bar{b})$	$\ell^+\nu_\ell\, l^-\,\bar{\nu}_l\, b\,\bar{b}$
decay accuracy	LO+PS	NLO+PS	NLO+PS
NLO radiation	single	multiple	multiple
spin correlations	approx.	exact	exact
off-shell $t\bar{t}$ effects	BW smearing	LO $b\bar{b}4\ell$ reweighting	exact
tW & non-resonant effects	no	LO $b\bar{b}4\ell$ reweighting	exact
b-quark massive	yes	yes	yes

Table 4.1.: The characteristics of the three MC generators used in this thesis, namely *hvq*, *ttb_NLO_dec* and $b\bar{b}4\ell$.

hand, *ttb_NLO_dec* also includes NLO matrix elements in the decay, but it only generates $t\bar{t}$ events that decay into a dilepton FS. Within *ttb_NLO_dec*, interference between $t\bar{t}$ and tW diagrams is only approximated, while *hvq* does not include them at all. The *ttb_NLO_dec* generator can also generate the hardest emissions using the multiple radiation scheme, which is not implemented in *hvq*. Moreover, *hvq* uses only approximate spin correlations, while both NLO generators include them exactly. Furthermore, only $b\bar{b}4\ell$ includes exact off-shell $t\bar{t}$ effects. All three generators are able to use the 4FNS.

In conclusion, $b\bar{b}4\ell$ implements many features that are missing in *hvq*, one of the standard generators in ATLAS, and constitutes significant improvements to *ttb_NLO_dec*, which in turn was introduced as an improvement to *hvq*.

5. The Impact of the $b\bar{b}4\ell$ Generator on a Direct Top-Quark Decay Width Measurement

The $b\bar{b}4\ell$ generator matches full NLO matrix elements to parton shower and implements exact spin-correlations for the first time, exact off-shell $t\bar{t}$ effects, and exact tW interference effects. It is thus the most precise theoretical prediction of the $pp \to \ell^+ \nu_\ell l^- \bar{\nu}_l b\bar{b}$ process. The purpose of this thesis is to study the impact of NLO effects on various $t\bar{t}$ related measurements, using the $b\bar{b}4\ell$ generator. It can be set up in ATLAS by following the instructions in App. A.1. In general, the event generation is divided into three stages:

- Integration: computation of the cross-sections
- POWHEG generation: generation of partonic events
- Showering: showering of the partonic events, done here with PYTHIA

5.1. Tuning and Validation of the $b\bar{b}4\ell$ Generator

In general, POWHEG offers two different running modes. It can either be run on a single core or it can be run on multiple cores. The job is divided into a number of sub-jobs corresponding to the number of cores used. In this mode, all sub-jobs can be processed in parallel. The first step of the validation of the generator was to try to run it on the local machines. Due to the characteristics of the available machine, only the single-core mode was used, instead of the multi-core mode. All three stages of the event generation were run together. The production time was dominated by the time needed for the integration stage, as it is a very CPU intensive task. To solve the problem of long integration times, POWHEG-BOX has a mechanism to reuse already existing integration files, so-called grids. Grids produced in single-core mode can only be reused in another single-core mode generation, while grids produced in a multi-core mode run, can be reused only in other multi-core mode generations. In Athena, the check for existing

grids is turned on by default. Therefore, if the grids are present in the working directory, they will be automatically reused.

When running $b\bar{b}4\ell$ on the Worldwide LHC Computing Grid (WLCG), the usage of OpenLoops is the biggest problem, as POWHEG-BOX-RES uses its own version of OpenLoops. This version is not distributed on the WLCG sites, leading to a crash of the program. Therefore, the integration can not be performed on the WLCG, nor can the grids be reused there. This makes it impossible to run the generator on the WLCG in the usual way. Multiple attempts were made to solve this problem.

The current solution is to use so-called supercomputing-sites, which also provide the required OpenLoops version. So far, two suitable supercomputing-sites could be found:

- `ANALY_MPPMU`
- `ANALY_INFN_LECCE`

A more detailed description of the problems and the attempts to resolve them can be found in App. A.2

A common problem in combining matrix element generated processes with parton shower generated processes, is the overlap in their phase space. If a process has a certain final state (FS), a corresponding NLO process can have an additional gluon in the FS. But this gluon can also be created by the parton shower. To prevent double counting those phase space regions, a userhook for PYTHIA was provided. This is done by *vetoing* certain emissions. It is combined with an additional userhook that performs a veto for all radiations generated by PYTHIA which are harder than the radiations generated by POWHEG. The userhook cannot be used on the local machines, because of a missing library (`luuid`) that could not be installed. Thus, from this point on, all work was performed on Lxplus, described in Sec. 3.2.2. The first version of the userhook contained a bug that could be solved. More information on the userhook can be found in App. A.3.

With this setup, the first large $b\bar{b}4\ell$ sample in ATLAS could be produced on the WLCG.

General Validation The first productions of $b\bar{b}4\ell$ contained some errors. In the first production, the distribution of *event weights* was uniform. This is not expected as the negative weights should also have been stored and the POWHEG output also had negatively weighted events. Thus, PYTHIA was omitting the POWHEG weights and set all of them to one. This problem could be fixed by changing the method in which the weights are stored. Another issue was due to the computation of the cross-sections. The upper bound calculated during the *hit-and-miss* technique, was exceeded in more than 80% of the cases, leading to a very high cross-section.

The computed value was

$$\sigma_{b\bar{b}4\ell} \approx 40 \text{ pb}. \tag{5.1}$$

The expected cross-section for this process is approximately 9.5 pb. This problem appears only in the single-core mode. As a cross-check, other single-core grids were produced on Lxplus and the WLCG, all with similar results. All those problems and the attempts made to solve them are described in App. A.4 for the first production and App. A.5 for the second production. It has not been noticed before, because the single-core mode had not been validated before the release. However, integration files produced in multi-core mode by the author of the generator[1] showed better results. Thus, it was decided to produce a new set of integration files, running POWHEG in multi-core mode.

5.1.1. Production and Validation of the First Multi-Core Sample

The setup for this production is in detail described in App. A.6. To improve the quality of the grids, the parameter `ncall1` had to be tuned. This parameter gives the number of iterations that are used to create the 23-dimensional grid of the MC integration. The integration grid must be iterated upon because a so-called importance sampling (IS) [109] is used.

The idea of IS is to increase the efficiency and reduce the variation of the MC integration by concentrating the sampling points in more important regions, i.e. peak-regions, which contribute the most to the integral. To do that, the original integrand $f(x)$ is transformed:

$$I = \int_a^b \mathrm{d}x f(x) \tag{5.2}$$

$$= \int_0^1 \mathrm{d}y J(y) f(x(y)) \tag{5.3}$$

$$\approx \frac{1}{M} \sum_y J(y) f(x(y)) \equiv \hat{I}. \tag{5.4}$$

Here, $\hat{I}$ is the MC estimate of the integral I derived from M sampling points. $\hat{I}$ is also a random number with mean I and

$$\mathrm{Var}(\hat{I}) = \sigma_{\hat{I}}^2 = \frac{1}{M} \left(\int_0^1 \mathrm{d}y J^2(y) f^2(x(y)) - I^2 \right) \tag{5.5}$$

$$= \frac{1}{M} \left(\int_a^b \mathrm{d}x J(y(x)) f^2(x) - I^2 \right). \tag{5.6}$$

[1] In the following often referred to as "author"

Following Eq. (5.6), it can be proven that $\sigma_{\hat{I}}$ becomes minimal if

$$J(y(x)) = \frac{\int_a^b \mathrm{d}x|f(x)|}{|f(x)|}. \tag{5.7}$$

Thus,

$$\frac{1}{J} = \frac{\mathrm{d}y}{\mathrm{d}x} \propto |f(x)|. \tag{5.8}$$

That means, when the standard deviation is minimised, the derivation of y with respect to x is proportional to the absolute value of the integrand. Thus the regions in x-space, where $|f(x)|$ is large, are enlarged in y-space, leading to a higher density of sampling points in these important regions, if the y-space is uniformly sampled.

After each call specified by `ncall1` the integration grid is further optimised, i.e. the variance is minimised. The spacing between two lines of the grid can be used to derive the transformation function. Ideally, the constructed grid should correspond to an equidistant grid after the transformation and, consequently, the cumulative function of the number of sampling points should be linear, starting at 0 and ending at 1. Fig. 5.1 shows the transformed grids and cumulative functions of all 23 integration parameters. These grids were given by the author as a reference. It can be seen that most of the grids are approximately equidistant. The integration parameters 1-4 and 8 are linear only in the central region, while parameter 21 is approximately linear after 0.4, but has a very steep slope before that. The IS did not work well for parameter 5. However, these cases were studied by the author, who claims that they do not pose a problem for the convergence of the integral. Fig. 5.2 shows the integration grids produced with the default settings in ATLAS of 150k calls. Compared to the reference grids in Fig. 5.1, it does not reach their precision. Even the grids that were almost ideally equidistant in the reference, show clear inhomogeneities. It can be concluded that the number of calls has to be increased. In Fig. 5.3, the grids for 1M calls can be seen. Even though it shows clear improvements compared to the grids created with the default settings, the inhomogeneities are still clearly visible. Thus, it was decided to increase `ncall1` to 5M. The corresponding plots can be found in Fig. 5.4. They are almost indistinguishable from the reference grids. Hence this setting was adopted for all following integrations.

The multi-core production ran without any violations of the upper bound, yielding a cross-section of

$$\sigma_{b\bar{b}4\ell} = (7.94 \pm 0.02)\ \text{pb}. \tag{5.9}$$

This value seems acceptable, since it is close to the expectation value.

Even though the grids could be produced in multi-core mode, there was no validated way of reusing them. Thus, before the event generation, the integration stage always had to be repeated.

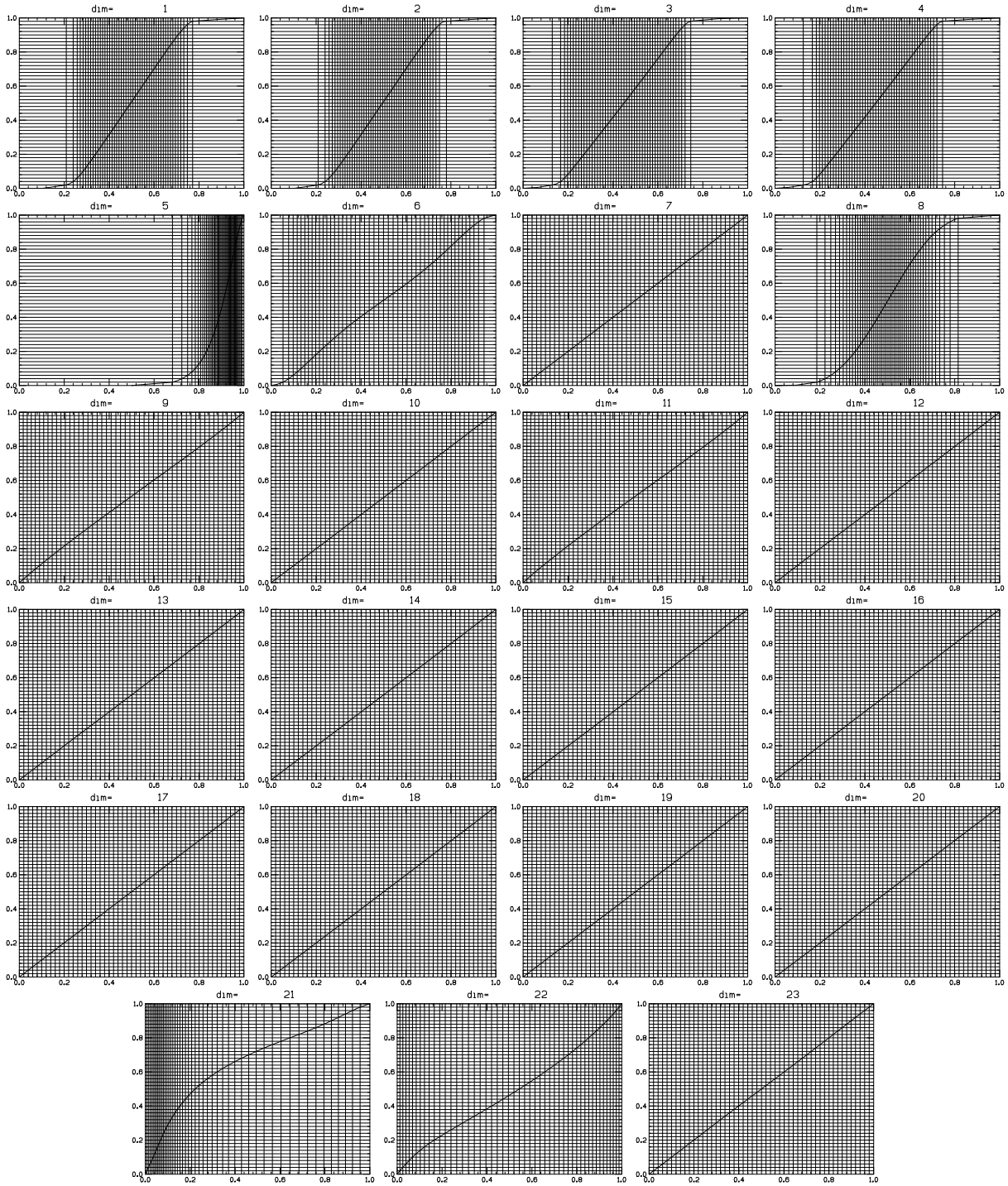

Figure 5.1.: The integration grids for all 23 integration parameters. These grids were produced by the author and were taken as a reference.

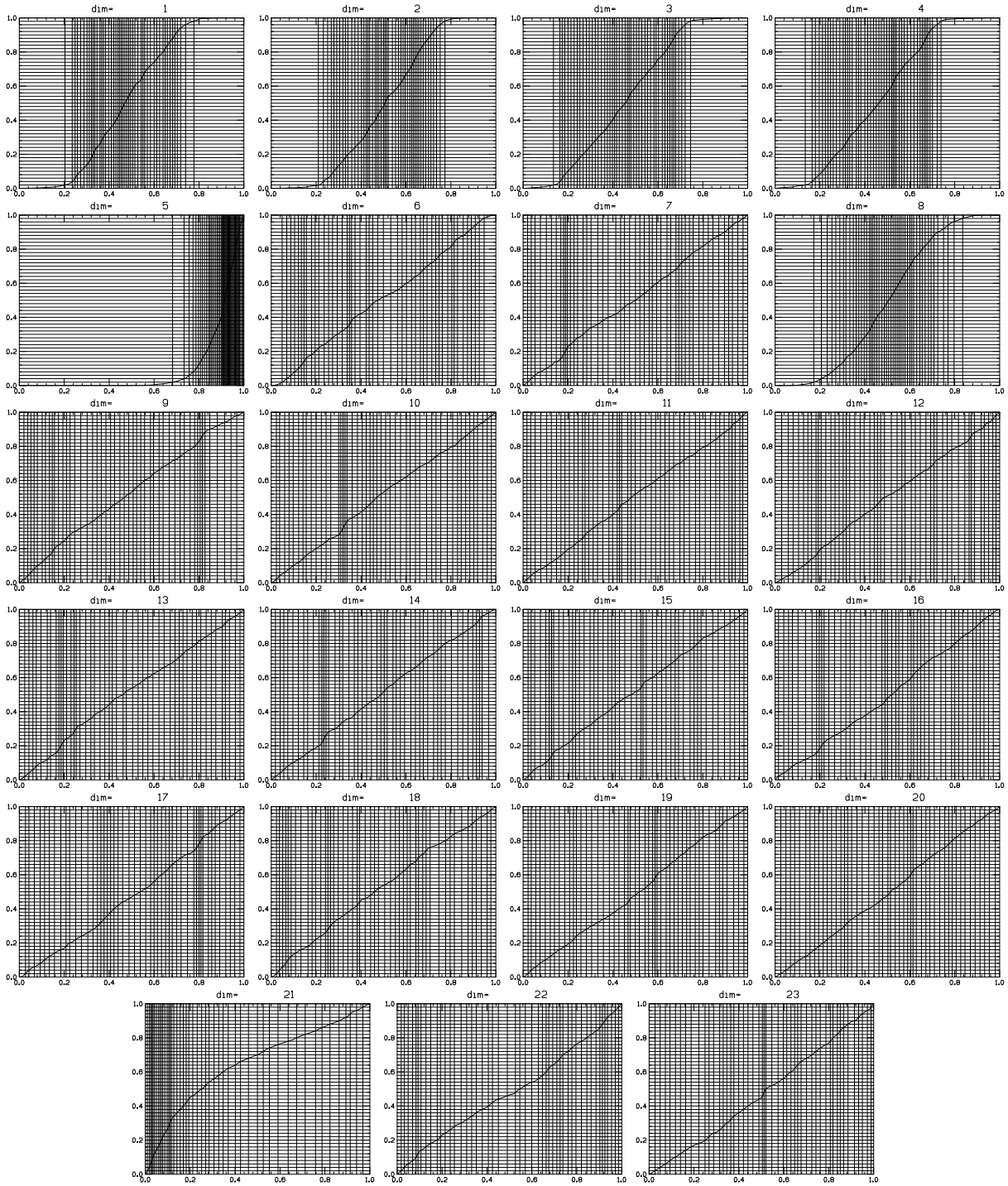

Figure 5.2.: The integration grids for all 23 integration parameters, if produced with the default settings in ATLAS. The number of calls is 150k.

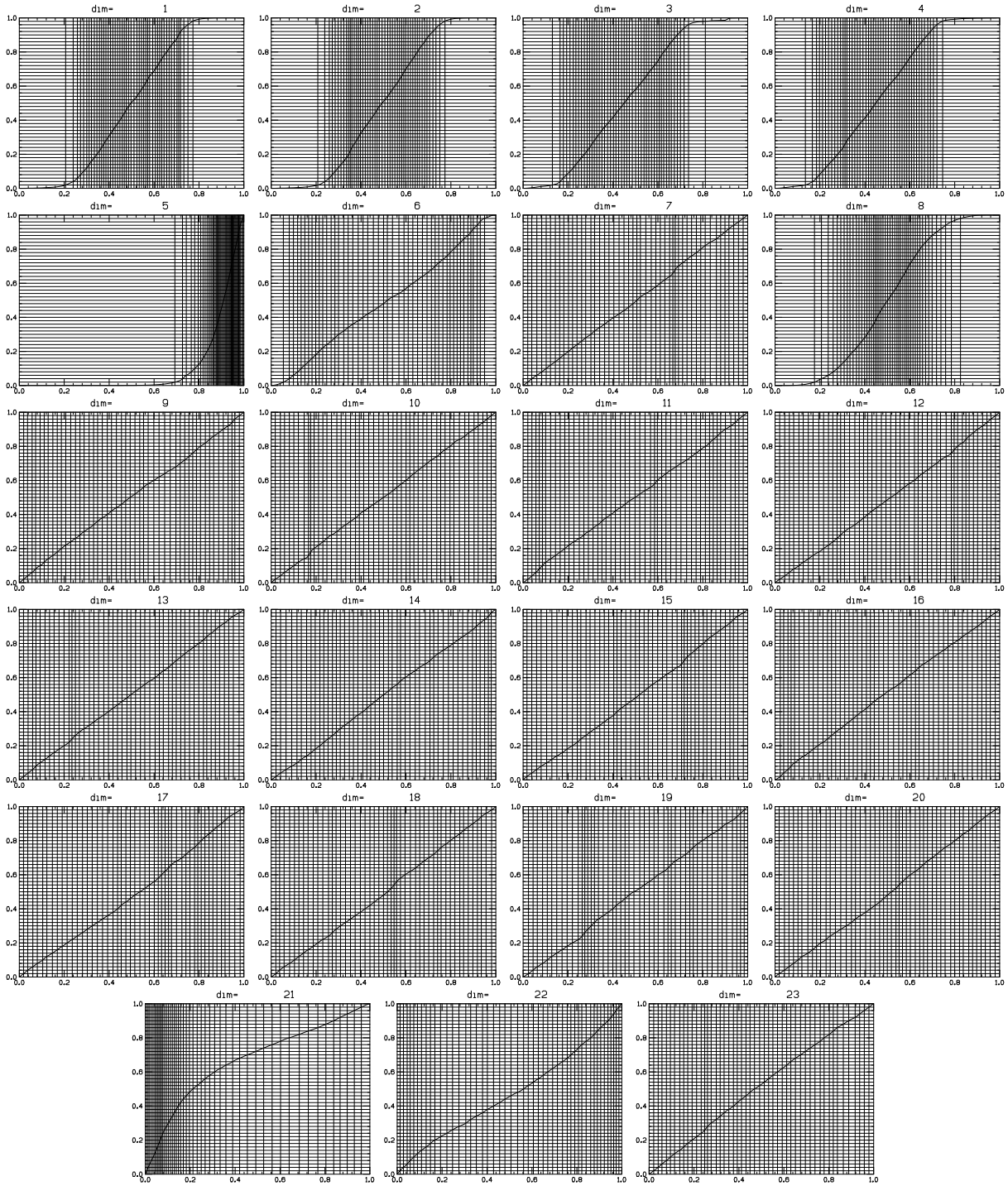

Figure 5.3.: The integration grids for all 23 integration parameters, if produced with `ncall1`=1M.

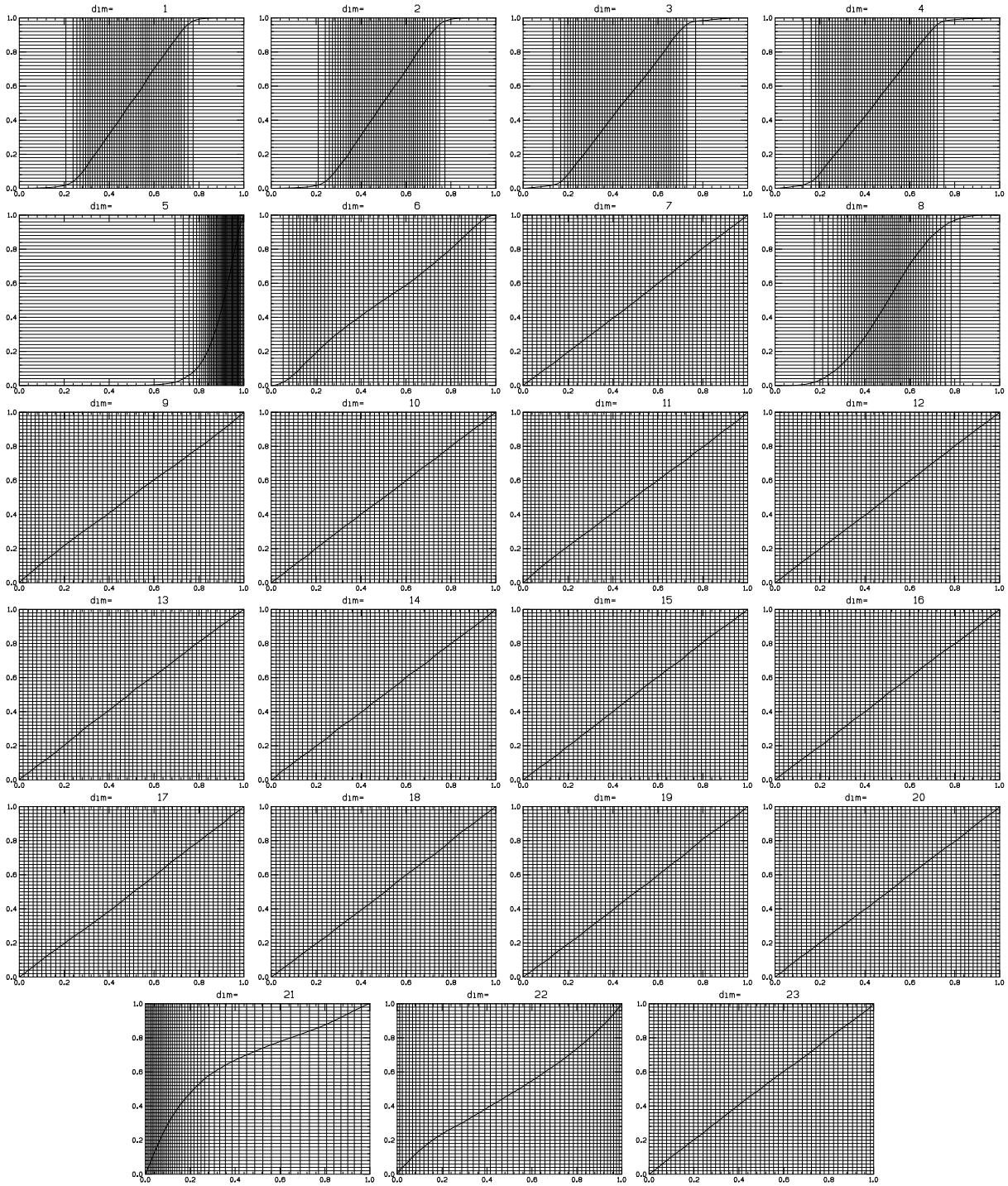

Figure 5.4.: The integration grids for all 23 integration parameters produced with 5M calls. This setup was adopted for all further integrations.

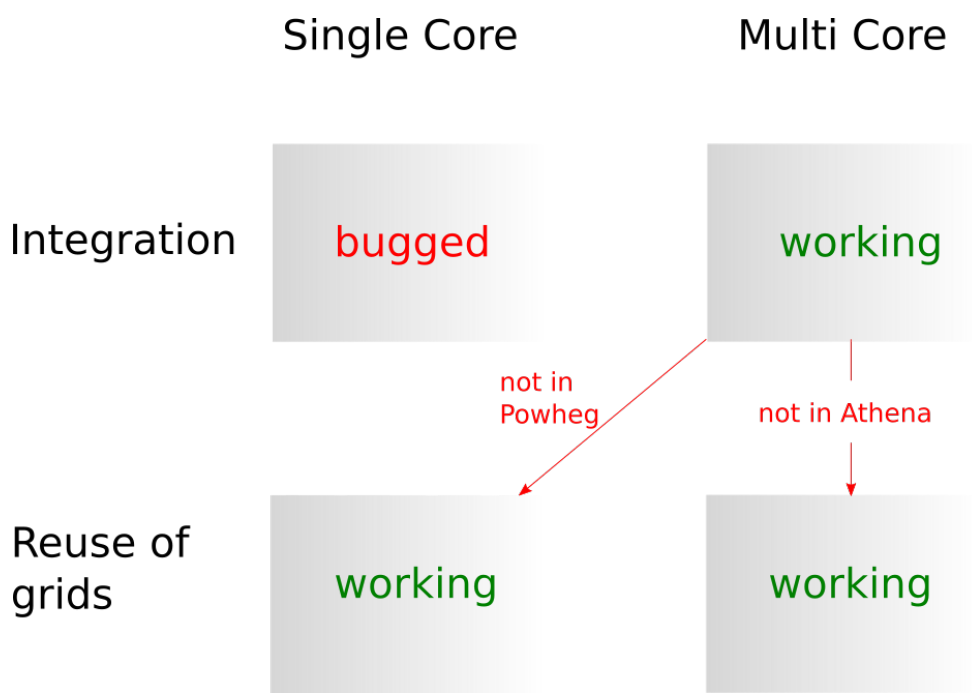

Figure 5.5.: Before the validation started, grids could not be reused in a validated way. Either because of POWHEG itself or because of the ATLAS framework.

Fig. 5.5 provides a small overview of the available options of reusing integration files before this validation was started. As mentioned in App. 5.1, the single-core grids are invalid and should not be used. Because multi-core grids are split into multiple files, corresponding to the number of used cores, they have to be merged by POWHEG to be used. This is not implemented in the single-core mode of POWHEG, but only in the multi-core mode. The multi-core mode, however, did not accept any grids as input at the time this problem was discovered. This made the reuse of integration files within ATLAS impossible.

A new version of PowhegControl was released that solved this problem. It implements the check for existing grids in Athena's multi-core mode. Additionally, when Athena is set up in single-core mode, it is forced to run POWHEG in its multi-core mode with one parallel process. This feature allows the reuse of multi-core integration files in single-core mode and consequently the use of the WLCG to generate events.

Since this version of PowhegControl was still in validation at that time, the first multi-core sample was produced without it. Without the new PowhegControl version, the only way to produce a sample with 1M events is to run the integration stage together with the generation stages on Lxplus. To do that, the production was split into 10 jobs, with 100k events each. Eight cores were used to produce the samples. All jobs were initialised with different random seeds, to ensure the independence of the samples. The weighted average of the computed cross-

section is

$$\sigma_{b\bar{b}4\ell} = (8.347 \pm 0.005)\ \text{pb}, \tag{5.10}$$

where the weight

$$w_i = \frac{1}{\Delta\sigma_i^2}, \tag{5.11}$$

with the computed uncertainty $\Delta\sigma_i$ on the i-th computed cross-section, is used. The *upper bound violations* were in no case higher than 0.32%.

A problem found in this production was missing *Zbb* events. They should be present in the sample as they can also decay into the $\ell^+ \nu_\ell l^- \bar{\nu}_l b\bar{b}$ final state, when the Z decays into a W^+W^--pair. Also, the produced log-files showed that the process itself was taken into account during the calculation of the cross-section.

5.1.2. Validation of Recent Samples

The attempt made to solve the problem of the missing *Zbb* events was to set the parameter `width_t` to -1. This parameter sets the value of the top-quark decay width that is used during the calculations in $b\bar{b}4\ell$. The ATLAS default setting is `width_t`=1.32, similar to the value expected by NLO calculations. However, usually this parameter is not set, i.e. `width_t`=-1. This way, the width is calculated by the generator using the other parameters given to it. This keeps the width value consistent with the theory. Even though the value calculated differs only slightly from 1.32, the explicit calculation of the width can also trigger other parts of the code, which could affect the production of *Zbb* events.

And indeed, a production where the top-quark width was calculated by the generator actually contained such *Zbb* events. The total number of *Zbb* events was 4 in approximately 2.5M, corresponding to a rate of 1.6×10^{-6}. However, the log-files show that the *Zbb* cross-section contributes with 1.4×10^{-4}. This discrepancy remains to be understood.

However, the new production made another problem of the ATLAS framework evident. The distribution of the event weights of the sample produced in the ATLAS framework was compared to the weights in a sample produced by the author, see Fig. 5.6. Throughout this chapter, "Atlas" will denote the sample produced within the ATLAS framework and "TJ" will denote the sample produced by the author of the generator. It can be seen that both samples have completely different weight distributions. While the weights in the author's sample have a continuous distribution with peaks at approximately ± 12.5, the sample produced within ATLAS shows only these peaks, with the addition of a few upper bound violations having a higher absolute value. The reason lies within the integration stage. To save computing time, an option called `for_reweighting` was introduced. If activated, the integration skips all virtual contributions to

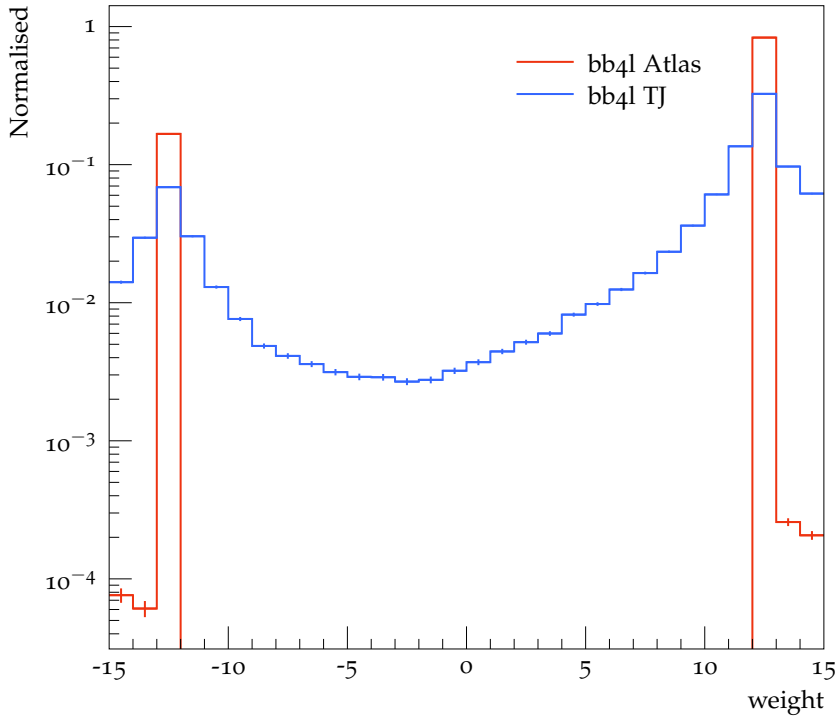

Figure 5.6.: A comparison of the weights in the sample produced in ATLAS and the weights in the sample produced by the author (TJ). While the weights should form a continuous distribution, they are mostly distributed as ±const, with the exception of a few upper bound violations that have higher absolute values.

the cross-section and calculates it only by using the Born and real contributions. To account for this, a reweighting is performed at the end of the integration incorporating the virtual corrections into the calculated event weights. This is also the reason, why the weights form a continuous distribution and nothing like ±const, as it is usual for unweighted events.

The ATLAS framework, however, does not recognise this option as a trigger for reweighting. Consequently, the virtual contributions are skipped during the integration, but this is not accounted for by a reweighting after the integration, resulting in a false weight distribution. This issue was reported and is, as of writing this thesis, still open[2]. However, a workaround was found. There are already other options that trigger the reweighting. If they are used, the reweighting would also apply the virtual corrections to the nominal weight. Thus, the currently used sample was produced with additional variations of the renormalisation (μ_R, $2\mu_R$, $\frac{\mu_R}{2}$) and factorisation scales (μ_F, $2\mu_F$, $\frac{\mu_F}{2}$) to trigger the reweighting step.

[2]For newest developments: `https://its.cern.ch/jira/browse/AGENE-1591`

5.1.3. Comparison with a Reference Sample

The latest production was compared in detail to a reference sample made by the author of $b\bar{b}4\ell$. It is expected to agree with the POWHEG and PYTHIA settings used in ATLAS. The userhook is used in the same version in both samples. However, there is already a newer version of the userhook available outside of ATLAS, which changes the criteria for vetoing events. Distributions for both userhook versions will be shown. The comparison was made with the Rivet framework [110]. Within this analysis, good leptons or jets are those which have $p_T >$ 25 GeV and $|\eta| < 2.5$. Leptons are dressed with all photons within a $\Delta R = 0.1$ cone around their momentum axis. The jets are reconstructed using the anti-k_T clustering algorithm [111] implemented in the FastJet package [112], with b-jets defined as jets containing B hadrons. The analysis code was taken from the ATLAS repository[3] of Rivet-analyses. As $b\bar{b}4\ell$ in ATLAS can currently only produce $\mu^- e^+$-FS, only the $e\mu$ event selection is used, as following:

1. Exactly one good muon.
2. Exactly one good electron.
3. No muon with 15 GeV $< p_T <$ 25 GeV and $|\eta| < 2.5$.
4. No electron with 15 GeV $< p_T <$ 25 GeV and $|\eta| < 2.5$.
5. Opposite signed electron and muon.
6. MET $>$ 20 GeV.
7. At least one good b-jet.
8. At least two good jets.

The η and p_T distributions for the leading and subleading leptons can be found in Fig. 5.7 and Fig. 5.8, respectively. More distributions can be found in App. C.1. The baseline of the ratio plots in all figures of this section is the sample produced in ATLAS. Its uncertainty is given as a yellow band and as error-bars for the samples produced by the author. The η distributions mostly agree with each other, while the p_T distributions show larger differences. Most of the deviations are below 5% and if there are larger deviations they are mostly in areas where the statistics are low, leading to large uncertainties. Some larger deviations that are not covered by the uncertainty band appear in areas with higher statistics as well. This is not unexpected, though, as the uncertainties have only a confidence level of 1σ. Remarkably, the sample with

[3] `https://gitlab.cern.ch/atlasphys-top/reco/RivetRoutines/tree/master/MC_TTbar_TruthSel`

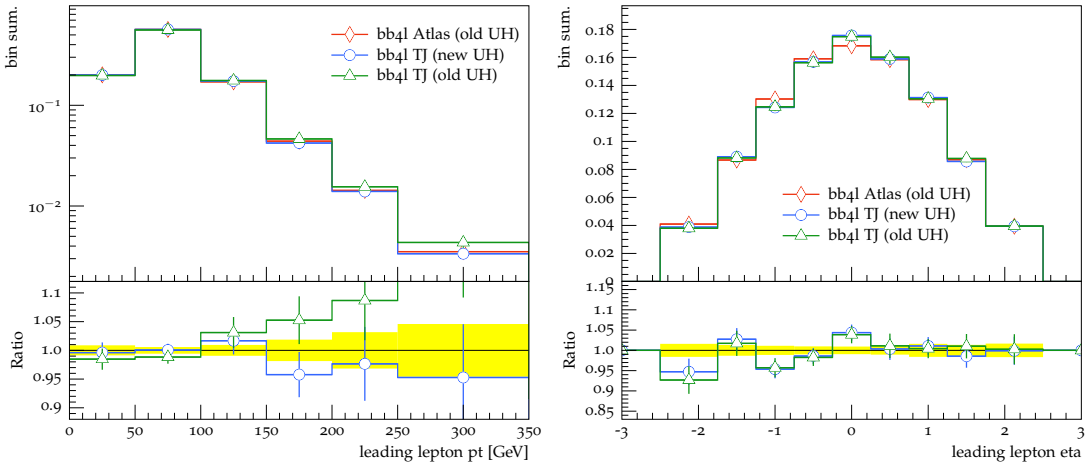

Figure 5.7.: The p_T distribution (left) and the η distribution (right) of the leading lepton. Statistical uncertainties of the ATLAS sample are given as a yellow band.

the new userhook version agrees better with the sample produced in ATLAS in some regions, most noteworthy in the high-p_T region of Fig. 5.7. In that plot, the sample with the matching version of the userhook seems to be systematically shifted towards higher p_T values.

Fig. 5.9 and Fig. 5.10 show the p_T and the η distributions of all jets and b-jets, respectively. The η distributions agree well with each other. With the exception of one outlier in the rightmost bin of the η distribution of all b-jets, all deviations are covered by the statistical uncertainty. However, the p_T distributions show larger differences. While deviations in the p_T distribution of the b-jets are still mostly covered by their statistical uncertainty, the corresponding distribution for all jets shows significant differences. Up to 150 GeV, these differences are still small in scale, i.e. less than 3%. After this threshold, the differences increase drastically. Similar to the lepton distributions, the sample with the matching userhook version seems to be shifted to high p_T values, even more than the sample with the new userhook.

Large differences can also be seen in the multiplicities of jets and b-jets, see Fig. 5.11. Similar to the p_T distribution of all jets, both distributions agree well for low multiplicities. However, the reference samples contain significantly more events with multiplicities larger than four, than the sample produced within ATLAS, regardless of the version of the userhook. The b-jet multiplicity shows a different picture. All samples agree well for events with exactly two b-jets. However, the sample with the new userhook predicts significantly fewer events with higher multiplicities than the sample produced in ATLAS, while the sample with the matching userhook version agrees well up to multiplicities of four. Only then, it shows significant upward deviations compared to the two other samples.

It has become clear that there are still fundamental differences between samples produced in the ATLAS framework and outside of it. However, it is not clear from where these differences

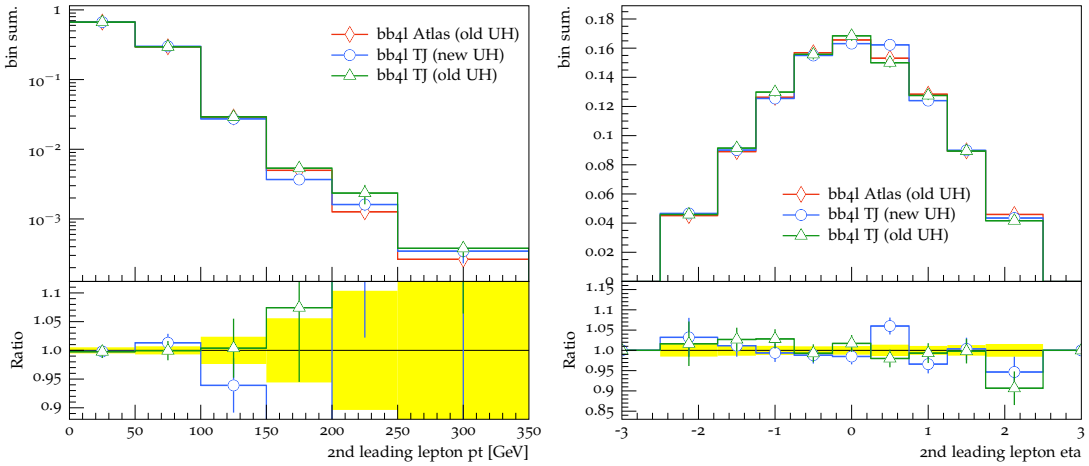

Figure 5.8.: The p_T distribution (left) and the η distribution (right) of the subleading lepton. Statistical uncertainties of the ATLAS sample are given as a yellow band.

originate. The POWHEG and PYTHIA settings were assimilated during previous validation steps. Additionally, samples were provided with different versions of the userhook, including the version currently used in ATLAS. Also, many bugs in the ATLAS framework affecting $b\bar{b}4\ell$ were discovered and solved. In conclusion, the differences have to originate from yet undiscovered bugs in the framework or from the details of the implementation of POWHEG-BOX-RES. In every case, this will need to be studied in more detail even after the scope of this thesis.

5.2. Applying the $b\bar{b}4\ell$ Generator to Different $t\bar{t}$-Measurements

In this section, the state of the analysis is presented, focusing on quantities at particle level. While the generator parton level consists only of the partons and is thus unphysical, the particle level uses the objects after hadronisation, see Sec. 4.1.3. Thus, radiation is added and quarks are showered into jets.

The event selection used is similar to the event selection described in Sec. 5.1.3, namely:

1. Exactly one good muon.
2. Exactly one good electron.
3. No muon with 15 GeV $< p_T <$ 25 GeV and $|\eta| < 2.5$.
4. No electron with 15 GeV $< p_T <$ 25 GeV and $|\eta| < 2.5$.
5. Opposite signed electron and muon.

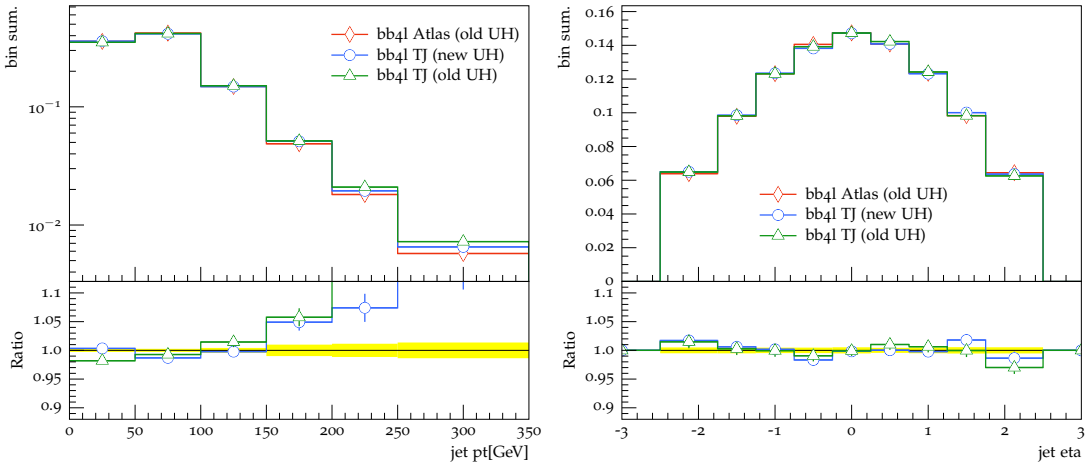

Figure 5.9.: The p_T distribution (left) and the η distribution (right) of all jets. Statistical uncertainties of the ATLAS sample are given as a yellow band.

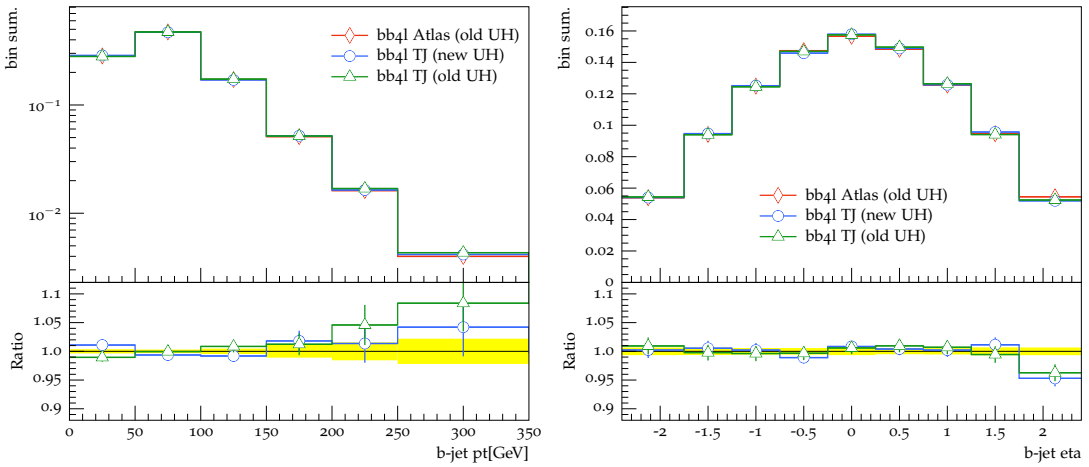

Figure 5.10.: The p_T distribution (left) and the η distribution (right) of all b-jets. Statistical uncertainties of the ATLAS sample are given as a yellow band.

6. MET > 20 GeV.

7. Exactly two good b-jets.

8. $e^+\mu^-$ FS

The last selection criterion is due to the technical restrictions of $b\bar{b}4\ell$, as it can only produce this FS, currently. For the same reason, all events containing $W \to \tau\nu_\tau$ are vetoed in the standard samples used in the comparisons presented here. The difference of $b\bar{b}4\ell$ and the standard generators will be discussed in the following sections, namely Sec. 5.2.1 for a direct top-quark decay width measurement, Sec. 5.2.2 for spin-correlation measurements and Sec. 5.2.3 for single top measurements, especially in the $t\bar{t}$ and tW interference region. The plots presented in the fol-

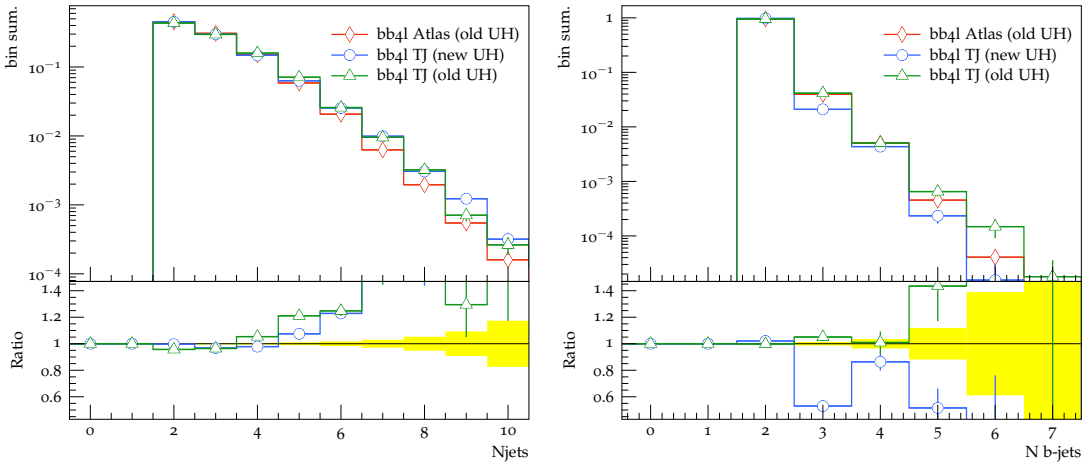

Figure 5.11.: The multiplicities of jets (left) and b-jets (right). Statistical uncertainties of the ATLAS sample are given as a yellow band.

lowing compare multiple generators. They include all three setups of $b\bar{b}4\ell$ seen in Sec. 5.1.3. Additionally, two samples typically used within ATLAS are included, which combine an $hvq\ t\bar{t}$ sample and tW samples, either applying *diagram removal* (DR) or *diagram subtraction* (DS) [113]. These techniques were introduced to solve a problem arising when tW events are produced at NLO QCD, since NLO tW diagrams are essentially LO $t\bar{t}$ diagrams. To be able to have valid separate samples for tW and $t\bar{t}$, this overlap has to be removed. To do this the total amplitude of the process is written as

$$\mathscr{M}_{\text{tot}} = \mathscr{M}_{\text{sr}} + \mathscr{M}_{\text{dr}}, \tag{5.12}$$

where sr denotes singly-resonant diagrams and dr doubly-resonant diagrams, i.e. $t\bar{t}$ diagrams. The absolute square is then

$$|\mathscr{M}_{\text{tot}}|^2 = |\mathscr{M}_{\text{sr}}|^2 + |\mathscr{M}_{\text{dr}}|^2 + 2\Re(\mathscr{M}^*_{\text{sr}}\mathscr{M}_{\text{dr}}). \tag{5.13}$$

DR takes only the first term on the right-hand-side and sets everything else to zero, thus neglecting not only the $t\bar{t}$ diagrams but also the interference effects. DS includes the interference term and neglects only the $t\bar{t}$ diagrams. Tab. 5.1 summarises the ATLAS samples used.

All distributions are scaled to their predicted event yield at an integrated luminosity of 120 fb^{-1}.

5.2.1. The Impact on a Direct Top-Quark Width Measurement

An important observable used in direct top-quark width measurements is m_{lb}. When the top-quark decays into a b-quark and a W boson, which in turn decays leptonically, m_{lb} is the in-

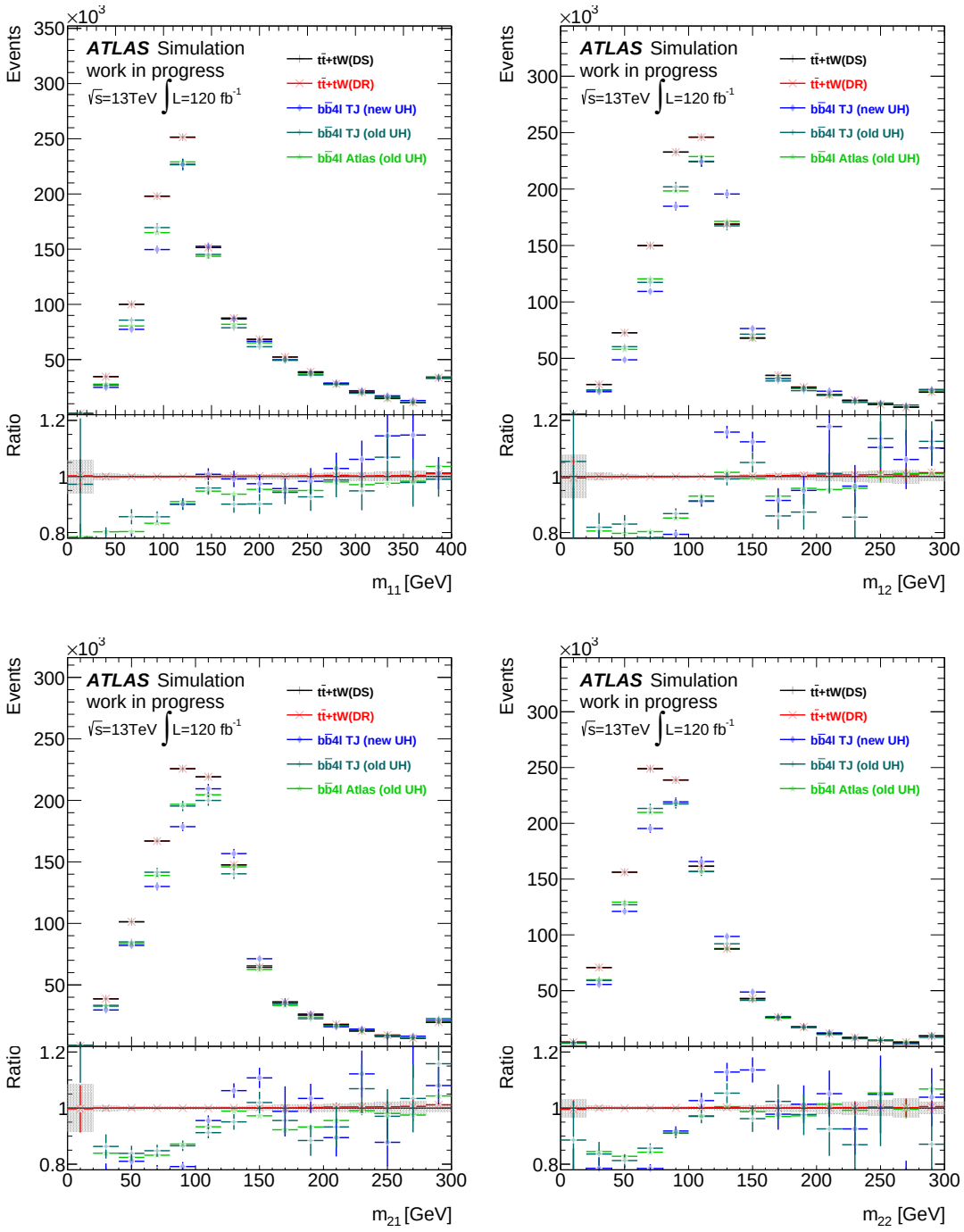

Figure 5.12.: Different m_{lb} distributions. The first index denotes the lepton that was taken for calculating m_{lb}, either the leading lepton (1) the subleading lepton (2). Analogously, the second index gives the assigned b-jet. Statistical uncertainties for $t\bar{t}+tW$ (DS) are given as a grey band.

Process	DSID
$t\bar{t}$	410472
tW (DR)	410646
	410647
tW (DS)	410654
	410655

Table 5.1.: The DSIDs of the ATLAS samples used.

variant mass of the combined lepton and b-quark system. This observable is very sensitive to the decay width and has the advantage that it is less sensitive to jet related uncertainties, like the jet energy scale or jet energy resolution. Both uncertainties were among the largest systematic uncertainties in the recent ATLAS measurement [49]. On particle level, the information of the origin of a jet is not readily available anymore. Thus, different combinations of b-jets and leptons were tried. Fig. 5.12 shows five different variations of m_{lb}. The first four variations pair leptons and b-jets according to their p_T relative to the other leptons and b-jets in the event. The first index denotes the lepton that was chosen, i.e. 1 for the leading lepton and 2 for the subleading lepton, and the second index denotes the selected b-jet, analogously.

It can be observed in all these distributions that the differences between the two *hvq* samples are small. The deviations become visible in the ratio plot only for high masses. Thus, it can be concluded that by applying the described event selection, the interference effects between $t\bar{t}$ and tW diagrams are negligible. However, it is expected that the tW contribution becomes more significant for values larger than

$$M_{lb}^2 = m_t^2 - m_W^2 \approx 153\ \text{GeV}, \tag{5.14}$$

as it is the kinematic limit for the correct pairing in $t\bar{t}$ events at LO.

It can also be seen that the total event yields predicted by $b\bar{b}4\ell$ and *hvq* are different. While $b\bar{b}4\ell$ agrees with *hvq* within the statistical uncertainties in the region of approximately 120 GeV and more, $b\bar{b}4\ell$ systematically predicts a lower event yield at lower values. It should be noted that the two samples with the old userhook version seem to agree better with *hvq* than the sample with the newest userhook version. For further, more precise comparisons a larger reference sample would be useful.

The differences in the distributions predicted by $b\bar{b}4\ell$ and *hvq* can be divided into a shape difference and a normalisation difference, i.e. a difference in the calculated cross-section. The shape difference is expected, as $b\bar{b}4\ell$ uses a resonance aware showering, see Sec. 4.2. That means, it preserves the virtuality of the resonances, while *hvq* does not, leading to a different shape of the mass distribution of the top-quark and thus m_{lb}. Also, the hardest radiation of

decaying resonances is described differently. In $b\bar{b}4\ell$, the hardest radiation of each decaying resonances is described by matrix elements, while *hvq* generates only the hardest radiation of all these resonances that way. Any other radiation is generated by the parton shower. These two aspects will be the main reason for the observed shape differences. In further studies, the individual contribution of these two sources can be studied by reconstructing the full top-quark mass instead of m_{lb} to see the shape difference more clearly. Additionally, the multiple radiation scheme can be controlled with the `allrad` option. Turning it off, will make $b\bar{b}4\ell$ use the single radiation scheme that is also used by *hvq*. The difference of normalisation has to originate in the integration stage. However, the cross-checks made to ensure the quality of the integration yielded positive results. The integration grids shown in Fig 5.4 were found to be positive and the number of upper bound violations is low, which can also be seen in Fig. 5.6. Additionally, upper bound violations would rather increase the calculated cross-section instead of decreasing it. Thus, the normalisation difference will be attributed to the additional precision included in the $b\bar{b}4\ell$ calculations, as summarised in Tab. 4.1.

It should be noted that the region most important for the direct width measurement shows the largest differences, possibly yielding a significant impact on the result of any such measurement.

5.2.2. The Impact on Spin-Correlation Measurements

As mentioned in Sec. 2.2, the top-quark decays before it hadronises. This means that the spins of the top-quarks are not decorrelated by hadronisation effects and remain correlated until they decay. Consequently, the spin-correlation is transferred directly to the decay products of the top-quark. Commonly, $\Delta\phi$ [114] is used to measure the correlation. In Fig. 5.13, the $\Delta\phi$ distributions of the leading and subleading b-jets, $\Delta\phi_b$, and leading and subleading leptons, $\Delta\phi_{\text{lep}}$ are shown. Almost no differences between the two $t\bar{t}+tW$ samples can be observed, implying that the interference effects between the two processes play a minor role in the differences that can be observed. Looking at $\Delta\phi_{\text{lep}}$, it can be seen that all three $b\bar{b}4\ell$ samples agree well with each other but deviate significantly from the $t\bar{t}+tW$ samples. They show a less steep slope, starting approximately 5% below $t\bar{t}+tW$ and ending approximately at 10% below the *hvq* samples. Since the $t\bar{t}+tW$ samples do not show these differences, they can be attributed to the implementation of the spin-correlation in the generators. While *hvq* describes the spin-correlation only in an approximative way, $b\bar{b}4\ell$ implements exact spin-correlations, see Sec. 4.2. Comparisons between data and the *hvq* samples [115] show a similar trend, thus it might well be that $b\bar{b}4\ell$ describes the data better with respect to this distribution. Looking at the $\Delta\phi_b$ distribution, a similar behaviour of $b\bar{b}4\ell$ can be observed; indeed, it is even stronger, starting approximately 5% above the $t\bar{t}+tW$ samples and ending approximately 15% below it. However, there a difference between the reference $b\bar{b}4\ell$ samples made by the author and the sample produced within

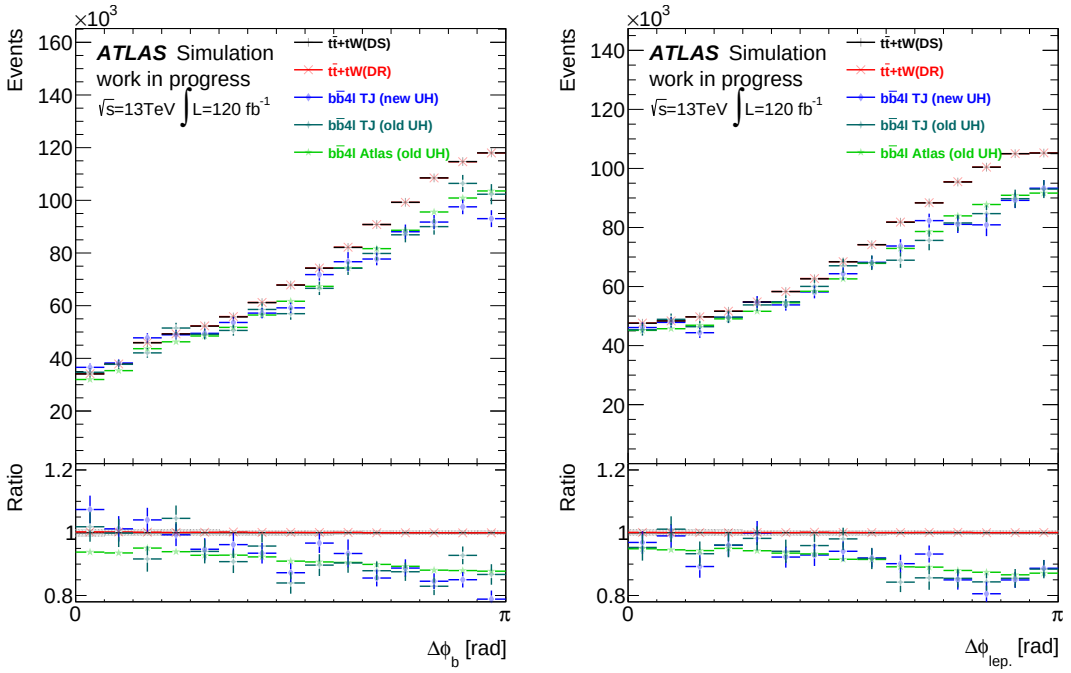

Figure 5.13.: $\Delta\phi$ between the two b-jets (left) and the two leptons (right). Statistical uncertainties for $t\bar{t}+tW$ (DS) are given as a grey band.

ATLAS can be observed, i.e. the slope of the latter is much closer to the slope of the *hvq* samples. This difference can also not be attributed to the userhook version, as the reference samples agree well. Because it implements the spin-correlation exactly instead of just an approximation like *hvq*, $b\bar{b}4\ell$ is predestined to be utilised in spin-correlation measurements and measurements sensitive to it.

5.2.3. The Impact on Single Top Measurements

A recently published study from the ATLAS collaboration probed for the first time the interference effects of $t\bar{t}$ and tW diagrams [116]. It also used a $b\bar{b}4\ell$ sample produced during this validation. It should be noted that the sample used in that study still lacks the virtual corrections in the event weight and operates with a preset top width. The observable under study is

$$\text{minimax} - m_{lb} = \min(\max(m_{11}, m_{22}), \max(m_{12}, m_{21})). \tag{5.15}$$

It uses the same nomenclature as described in Sec. 5.2.1. Since the $t\bar{t}$ contribution to m_{lb} drastically declines after approximately 153 GeV, see Eq. (5.14), the interference terms become more important after this threshold.

Looking at Fig 5.14, in which the reconstructed minimax-m_{lb} distribution is shown, the dif-

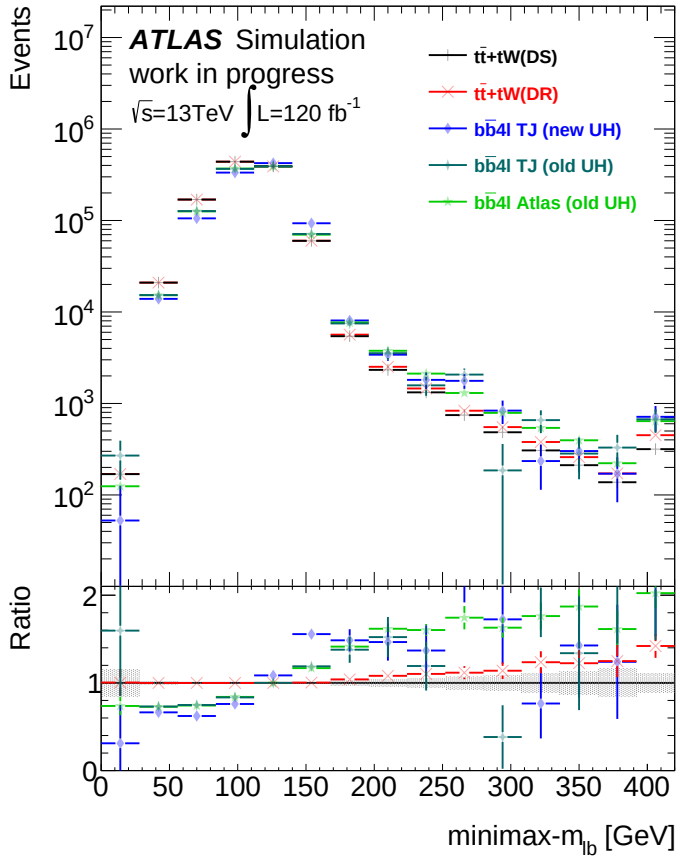

Figure 5.14.: The plot shows minimax-m_{lb}, calculated according to Eq. (5.15). Statistical uncertainties for $t\bar{t}+tW$ (DS) are given as a grey band.

ferences between DS and DR become clear. As expected, there is no visible difference between these two models below the 153 GeV threshold. Above this threshold, the sample including the tW (DR) sample predicts significantly more events. This trend increases with the value of minimax-m_{lb}. In the last bin, summarising all values larger than 390 GeV, the difference is already 40%. All three $b\bar{b}4\ell$ samples seem to agree well with each other, although the reference samples ($b\bar{b}4\ell$ TJ) suffer from a lack of statistics. However, the $b\bar{b}4\ell$ samples do not agree with the *hvq* samples. In the low minimax-m_{lb} range, the same behaviour is observed as already discussed in Sec. 5.2.1, i.e. a systematically lower event yield in the $b\bar{b}4\ell$ sample in that range. For higher values than that, $b\bar{b}4\ell$ predicts systematically higher values than both of the *hvq* samples, although definitive statements would require higher statistics in the reference samples. This is however not expected. Since tW (DS) includes the interference terms, its predictions should be closer to the result of $b\bar{b}4\ell$. However, the predictions of $b\bar{b}4\ell$ seem to be even higher than the predictions made by $t\bar{t}+tW$ (DR). Also, in [116], it was found that the $b\bar{b}4\ell$ predictions

lie between the predictions of $t\bar{t}+tW$ (DR) and $t\bar{t}+tW$ (DS) in the high minimax-m_{lb} region, which meets the expectation. However, there are a few differences in the treatment of the $b\bar{b}4\ell$ sample, which was reweighted in that analysis, and the event selection, which in this analysis is not specifically tailored for this observable.

Generally speaking, this generator is expected to become the generator of choice for all measurements sensitive to the interference effects of $t\bar{t}$ and tW diagrams, as it has the most precise description of it. It can also be used to verify models to describe the interference effects, such as DR and DS.

6. Conclusion

The $b\bar{b}4\ell$ Monte Carlo (MC) generator produces events with an $\ell^+ \nu_\ell l^- \bar{\nu}_l b\bar{b}$ final state (FS) incorporating all possible Feynman diagrams leading to this FS at NLO QCD. For the first time, spin-correlations, off-shell $t\bar{t}$ effects, and tW interference effects are implemented exactly. Additionally, it is able to use the four flavour number scheme and it can generate the hardest radiation of each decaying resonances using matrix elements, instead of just the hardest radiation of all decaying resonances, like *hvq*, the standard MC generator in ATLAS. Thus, $b\bar{b}4\ell$ features the most precise implementation of the theoretical predictions for this process so far, which makes it very important to validate the generator for its use in ATLAS.

During the validation many bugs were found and solved, including a false handling of event weights in PYTHIA, many problems with the generation of integration files and their reusability, caused by the ATLAS framework and $b\bar{b}4\ell$ itself, and further bugs in the ATLAS framework. Despite the number of solved bugs, it is currently not possible to reproduce the samples produced by the author of the generator outside of ATLAS. The largest remaining differences can be found in the jet kinematics and multiplicities, as seen in Fig. 5.9 and Fig. 5.11.

When compared to *hvq*, significant differences are revealed. Looking at different variations of m_{lb}, the invariant mass of the b-jet and the corresponding lepton from a leptonically decaying W, see Fig. 5.12, the largest differences are in the low m_{lb} range. This is also the range important for direct top-quark decay width measurements, as it contains the majority of the events. Thus, it is well possible that the NLO effects implemented in $b\bar{b}4\ell$ can have a significant impact on this measurement. The fact that $b\bar{b}4\ell$ implements spin-correlations exactly, causes significant differences in $\Delta\phi$ distributions, see Fig. 5.13, which are the observables sensitive to the spin-correlation. The less steep slope of the curve is a behaviour also observed in data. Hence, $b\bar{b}4\ell$ could potentially help to improve spin-correlation measurements. Its exact implementation of tW interference effects becomes visible in the distribution of minimax-m_{lb}, see Fig. 5.14. However, the predictions made by $t\bar{t}+tW$ (DS) and $t\bar{t}+tW$ (DR) could not be reproduced with $b\bar{b}4\ell$ to the expected extent.

The implementation of $b\bar{b}4\ell$ in ATLAS remains flawed and will require more work in validating the exact implementation of $b\bar{b}4\ell$, POWHEG-BOX-RES, the framework in which $b\bar{b}4\ell$ is implemented, and possibly the combination of the userhook. The combination of the two user-

hooks necessary for $b\bar{b}4\ell$, which can be combined in multiple ways, can also affect the resulting distributions.

To measure the impact of the use of $b\bar{b}4\ell$ on the presented types of analyses in more detail, some essential features of it can be turned off individually, e.g. the impact of the multiple radiation scheme can be measured by switching to the single radiation scheme. Depending on the observable, these distributions can be used to study the impact of other features. For example, the shape of a top mass distribution reconstructed from a sample produced with the single radiation scheme should be dominantly changed by the effects of the resonance aware showering. This should be done as soon as $b\bar{b}4\ell$ is fully validated in ATLAS.

A. Running $b\bar{b}4\ell$

A.1. Setup of POWHEG on-the-Fly

POWHEG-BOX processes can be accessed in ATLAS through the so-called POWHEG on-the-fly (OTF) interface. To run POWHEG OTF, two packages have to be installed:

- Powheg
- PowhegControl: the ATLAS implementation of POWHEG-BOX

The working directory will be `TestArea` for these instructions. It will be assumed that the ATLAS environment and version 19.2.5.26.4,MCProd of Athena are set up. Package versions are denoted by six digits following the name of the package. Copying the packages from the central repository is called *check-out* and can be done by using the *python* script

```
$ pkgco.py Powheg
```

for the Powheg package. After that it has to be compiled by:

```
$ cd TestArea/External/Powheg/cmt
$ cmt config
$ make
```

The same has to be done for `PowhegControl`. As PowhegControl is not an external package but an internal implementation of POWHEG-BOX, it is saved in the `Generators` directory. After that is done, the environmental variable

```
$ export POWHEGPATH=/afs/cern.ch/atlas/offline/external/powhegbox/
    ↪ ATLASOTF-00-03-10
```

has to be set, in this example for `Powheg-00-03-10`, if that was not the case yet.

To run a generator, a clean directory has to be created. The JO have to be placed in this directory. A collection of example JO are already provided by the PowhegControl package and can be copied into the clean directory. The JO used in this analysis can be found in App. B.1. Finally, the event generation can be started by

```
$ Generate_tf --ecmEnergy=13000 --runNumber=999999 --firstEvent=1 --
   ↪ randomSeed=1 --jobConfig=JO.py --outputEVNTFile=output.root
```

The flags `ecmEnergy` and `runNumber` have to be set to the values needed for the analysis.

A.2. Running $b\bar{b}4\ell$ on the Grid

To run the event generation on the grid, pAthena is used. To reuse the grids in a production on the grid, they have to be compressed to a *tar* file. This file can be uploaded to the grid together with the job using the `extFile` flag. For POWHEG to reuse the grids within the file, POWHEG's `inputGenConfFile` flag has to be set, by specifying the name of the file.

The POWHEG-BOX-RES uses its own version of OpenLoops, which is not distributed on the grid sites. This will cause a crash of the program, when it tries to open the `proclib` folder contained in the POWHEG-BOX-RES version 1.3.1x, but not in the distributed version 1.3.1. However, this is necessary to perform the integration stage or reuse existing grids, which makes it impossible to run the generator on the grid in the standard way.

The following attempts were made to solve this problem. Compiling the locally present version 1.3.1x of OpenLoops and uploading it to the grid together with the job, did not work. The uploaded package was ignored. Another attempt was to change the OpenLoops path (`OLPATH`) of POWHEG-BOX-RES. In the current implementation it is given as

```
$ OLPATH=$(PWD)/../OpenLoopsStuff/OpenLoops
```

linking POWHEG-BOX-RES against an OpenLoops version with a path relative to the current working directory ($PWD). As it is not compiled directly on the grid, it might cause problems relating the path to the current working directory. Changing it to

```
$ OLPATH=../OpenLoopsStuff/OpenLoops
```

was supposed to exclude this possibility. However, it did not resolve the problem.

The supercomputing-sites have the resources to provide multiple versions of certain programs and keeping all libraries and links up to date, including the needed OpenLoops version 1.3.1x. So far, two suitable supercomputing-sites could be found:

- `ANALY_MPPMU`
- `ANALY_INFN_LECCE`

Grid sites can be specified in pAthena by using the `site` flag.

A.3. The PYTHIA Userhook

The provided userhook can be found in the package `Pythia8_i-00-14-04` and upwards. That package can be *checked-out* as demonstrated in App. A.1. The use of it is initialised in the JO, see App. B.1, by including the line `genSeq.Pythia8.UserHook += ['PowhegBB4L']`. The userhook cannot be used on the available machines, because of a missing library (`luuid`) that could not be installed.

However, as soon as it called a certain function for a particle that is not a top-quark, i.e. PDG Id does not equal six, it threw an exception, leading to a crash of the program. It was implemented like this for debugging purposes and not changed until then. This problem was solved by returning zero, whenever the particle is not a top-quark. Also, the veto did not work, because of default settings that had to be changed by the authors. For this, a set of new JO were provided in a *tar* file, replacing the JO included by the JO.py script in App. B.1. They can be used by setting the `evgenJobOpts` flag of Athena to the name of the file. The relevant JO can be found by following the link in the appendix.

In general, the userhook version implemented in ATLAS is outdated. A newer version is available outside of ATLAS.

A.4. Validation of the First Production

The first production had a total sample size of 955000 events. Although one million events were attempted, efficiency problems of PYTHIA lead to some failed jobs. Those fails can be limited by increasing the ratio of POWHEG generated events to PYTHIA showered events. The default ratio is 1.1, which was changed to three. All produced *EVNT* files, were transformed into the *DxAOD* format by using Athena. A production of that size, including the transformation into the *DxAOD* format, takes approximately one week. It was found that all events in this production had uniform weights of one, although they are expected to include negative weights as well. Looking at the LHE output of POWHEG, it generated also events with negative weights. This means, the problem has to be in PYTHIA. When run with a single MC weight, the default option, they are stored as unnamed `double` values in vectors. If multiple shower weights are enabled, however, it creates a named map, seemingly leading to a different behaviour, since the weights were all present in the final output. In case of multiple weights, the first one corresponds to the nominal weight. This problem was fixed in `Pythia8_i-00-14-07`.

Thus, a second production with fixed weights became necessary.

A.5. Validation of the Second Production

The second production contained 920000 events. Because of large and unexpected deviations of the $b\bar{b}4\ell$ generated distributions from the *hvq* generated ones, it was tried to disable the multiple radiation scheme. This results in hardest emissions from the b-quark generated by matrix elements only in a fraction of all events and at maximum one b-quark per event. The remaining hardest generations would be described by the parton shower, as it is in *hvq*. The resulting $b\bar{b}4\ell$ distributions were indeed closer to the *hvq* distributions, but the difference could not explain the deviations seen.

Another problem apparent in that production was the integration stage. The number of *upper bound violations* was 4507 in 5500 events produced with POWHEG, corresponding to a fraction of approximately 82%. An *upper bound violation* can appear in the unweighting of the events. As described in Sec. 4.2.3, the $\tilde{B}$ function is used to unweight the events via the *hit-and-miss* technique. For that, an upper bound of $\tilde{B}$, $\tilde{B}^{\max}$ has to be calculated. When the computed $\tilde{B}$ for the generated event is larger than this upper bound, an *upper bound violation* is triggered. Because of the computation being numerical and thus not exact, this can happen even in a valid sample, but the number of *upper bound violations* should be less than 1%. Due to the large number of violations, the calculated cross-section for the process was

$$\sigma_{b\bar{b}4\ell} = (39.44 \pm 0.08)\ \text{pb}. \tag{A.1}$$

The expected cross-section for this process is approximately

$$\sigma^{\text{exp.}}_{b\bar{b}4\ell} = 818\ \text{pb} \times 0.108^2 \approx 9.5\ \text{pb}, \tag{A.2}$$

with the $t\bar{t}$ inclusive cross section of 818 pb taken from [54] and the branching ratio of 10.8% [32] for W decaying into leptons. The reason for this amount of *upper bound violations* appears to be a bug in the single-core mode of the generator.

A.6. Production and Validation of the Multi-Core Sample

Outside Athena, the multi-core mode of POWHEG is enabled by setting the `manyseeds` flag to one. It will then ask for line numbers of a file called `pwgseeds.dat` that needs to be prepared beforehand. Each line of that file contains a number, which can be used as a *random seed* to initialise the generation. In Athena, this is not possible. Instead the environmental variable `ATHENA_PROC_NUMBER` has to be set to the number of cores that should be used for POWHEG. Then, Athena will automatically run POWHEG in multi-core mode, creating the `pwgseeds.dat`

file itself. The multi-core grids were produced on Lxplus with eight cores within approximately one day.

During the integration, parameters reflecting the quality of the integration grids are calculated and written to so-called *top* files. Plotting these files, allows to check the quality. If the quality is not sufficient, certain integration parameters, here `ncall1`, can be tuned. By setting `ncall1` to 5M, the same quality as in the reference plots is achieved. This integration ran without any upper bound violations. The computed cross-section is

$$\sigma_{b\bar{b}4\ell} = (7.94 \pm 0.02)\ \text{pb}. \tag{A.3}$$

In general, multi-core grids can be reused by POWHEG in another multi-core run. To do this, the flag `parallelstage` has to be set to four. The integration stage is divided into four different stages within POWHEG, the last one including the internal merging of the grids.

B. Additional Material

Tab. B.1 gives an overview of available materials, such as plots and code used for the validation.

Material	Link or Public Directory
Rivet-routines	`https://gitlab.cern.ch/maniemey/Rivet-code`
Eventsaver	`https://gitlab.cern.ch/maniemey/anatop`
Plotting	`https://gitlab.cern.ch/maniemey/Evt_ana_v00`
JobOptions	`https://gitlab.cern.ch/maniemey/JobOptions`
AnalysisTop output	/work1/marcel.niemeyer/Public/AnalysisTop-Outputs

Table B.1.: Locations of additional material, such as the code used for the validation and plots. Plots can be found in the same gitlab repository as the code that was used to create them.

B.1. JobOptions for MC Generation

The JO used to generate the MC events. Additional options in POWHEG, e.g. the number of produced events *nEvents*, can be set via *PowhegConfig* variables. The number of events is set to 1.5 times the default amount in this example, because event generations can crash during the showering with PYTHIA, if the number of events generated is too low. Also, these JO include the Pythia Userhook *PowhegBB4L*.

```
evgenConfig.generators += ["Powheg", "Pythia8"]
evgenConfig.description = 'Powheg␣WWbb␣production,␣including␣interference
    ↪ ␣between␣ttbar␣and␣Wt.␣␣A14␣NNPDF23␣tune'
evgenConfig.keywords += [ 'SM', 'top', 'WW', 'lepton']
evgenConfig.contact = [ 'Ben␣Nachman␣<bnachman@cern.ch>' 'James␣Monk␣<
    ↪ jmonk@cern.ch>']

# ------------------------------------------------------------
# Load ATLAS defaults for the Powheg bblvlv process
```

```
# --------------------------------------------------------------
include("PowhegControl/PowhegControl_bblvlv_Common.py")

# --------------------------------------------------------------
# Generate events
# --------------------------------------------------------------
PowhegConfig.bornktmin=0
PowhegConfig.btildeborn=1
PowhegConfig.btildecoll=1
PowhegConfig.btildereal=1
PowhegConfig.btildevirt=1
PowhegConfig.btlscalect=0
PowhegConfig.btlscalereal=0
PowhegConfig.novirtual=0
PowhegConfig.ptsqmin=0.8
PowhegConfig.nEvents*=1.5
PowhegConfig.allrad=1
PowhegConfig.ncall1=5000000
PowhegConfig.width_t=-1
PowhegConfig.parallelstage=4
PowhegConfig.mu_F = [1.0, 0.5, 0.5, 0.5, 2.0, 2.0, 2.0]
PowhegConfig.mu_R = [1.0, 0.5, 1.0, 2.0, 0.5, 1.0, 2.0]
PowhegConfig.generate()


include('MC15JobOptions/Pythia8_A14_NNPDF23LO_EvtGen_Common.py')
include('MC15JobOptions/Pythia8_Powheg_Main31.py')

genSeq.Pythia8.UserHooks += ['PowhegBB4L']

genSeq.Pythia8.Commands += [ "Powheg:pTHard␣=␣0",
                             "Powheg:NFinal␣=␣2",
                             "Powheg:bb4l:onlyDistance1␣=␣1"]
```

C. Comparison with a Reference Sample

C.1. Lepton Distributions

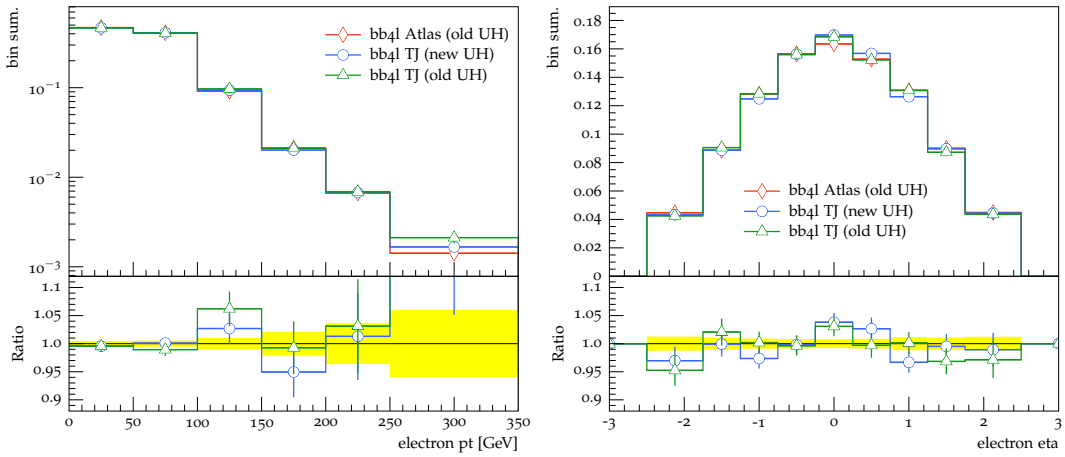

Figure C.1.: The p_T and η distributions of all electrons. Statistical uncertainties of the ATLAS sample are given as a yellow band.

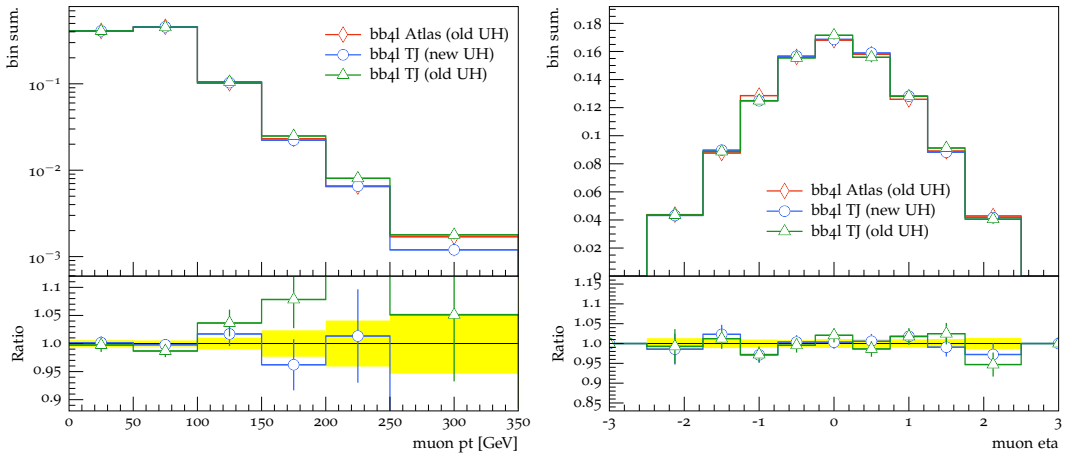

Figure C.2.: The p_T and η distributions of all muons. Statistical uncertainties of the ATLAS sample are given as a yellow band.

C.2. Jet Distributions

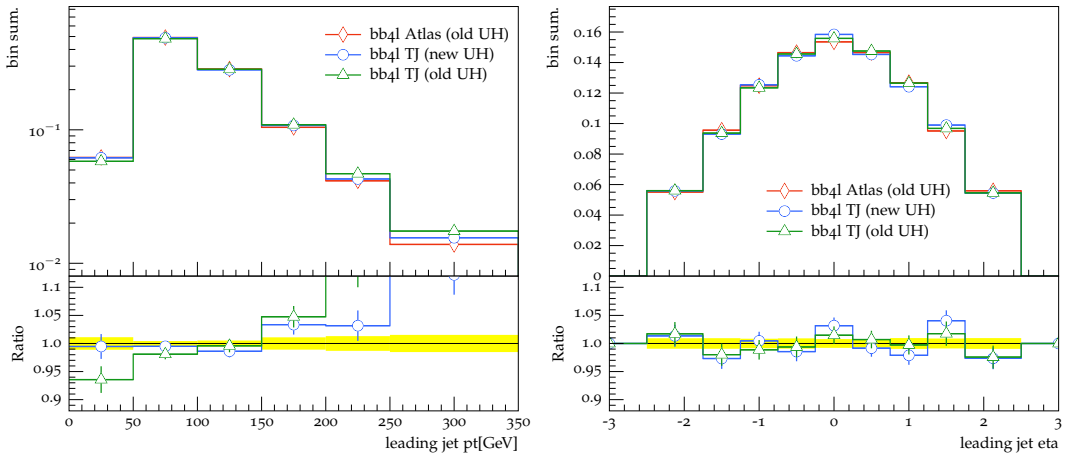

Figure C.3.: The p_T and η distributions of the leading jets. Statistical uncertainties of the ATLAS sample are given as a yellow band.

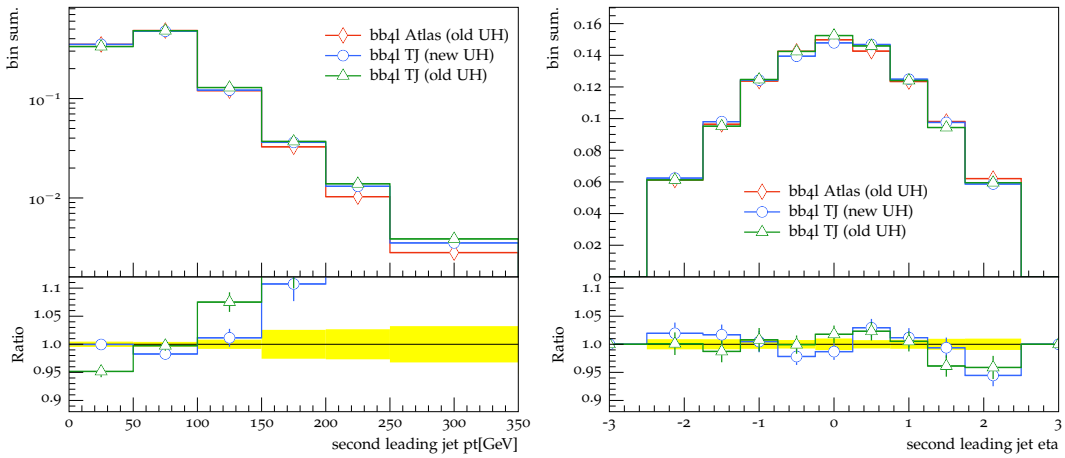

Figure C.4.: The p_T and η distributions of the subleading jets. Statistical uncertainties of the ATLAS sample are given as a yellow band.

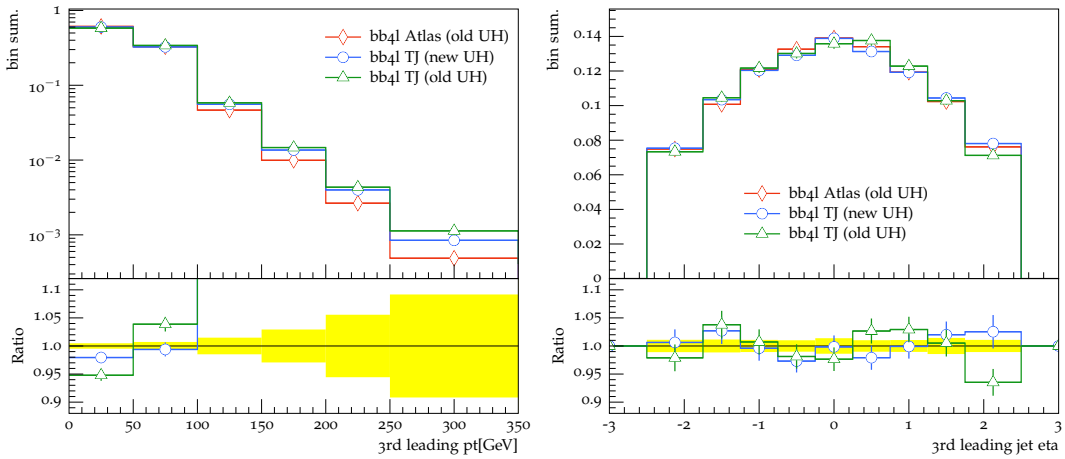

Figure C.5.: The p_T and η distributions of the 3rd-leading jets. Statistical uncertainties of the ATLAS sample are given as a yellow band.

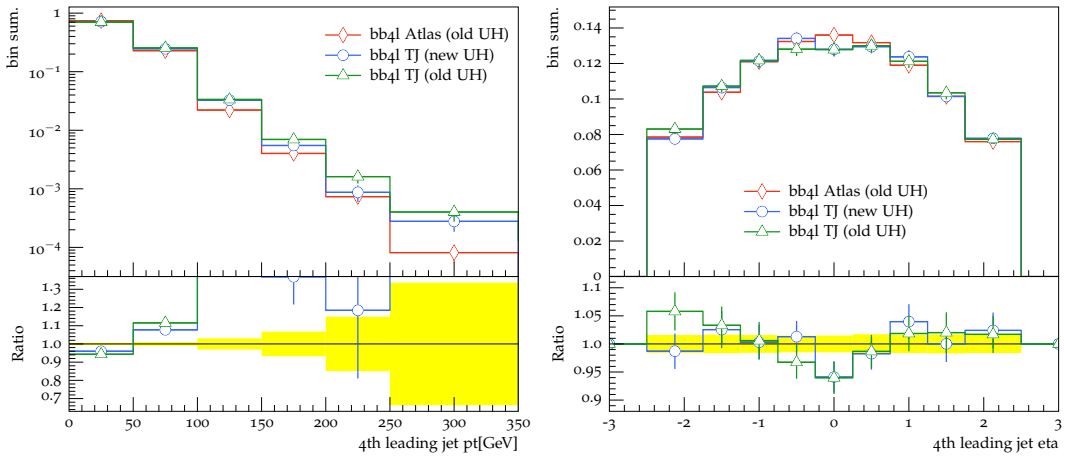

Figure C.6.: The p_T and η distributions of the 4th-leading jets. Statistical uncertainties of the ATLAS sample are given as a yellow band.

C.3. *b*-Jet Distributions

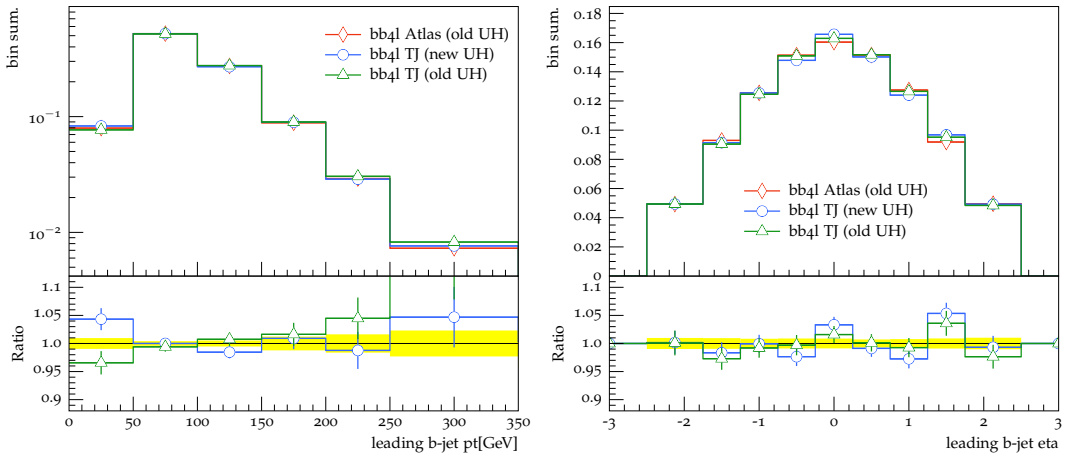

Figure C.7.: The p_T and η distributions of the leading b-jets. Statistical uncertainties of the ATLAS sample are given as a yellow band.

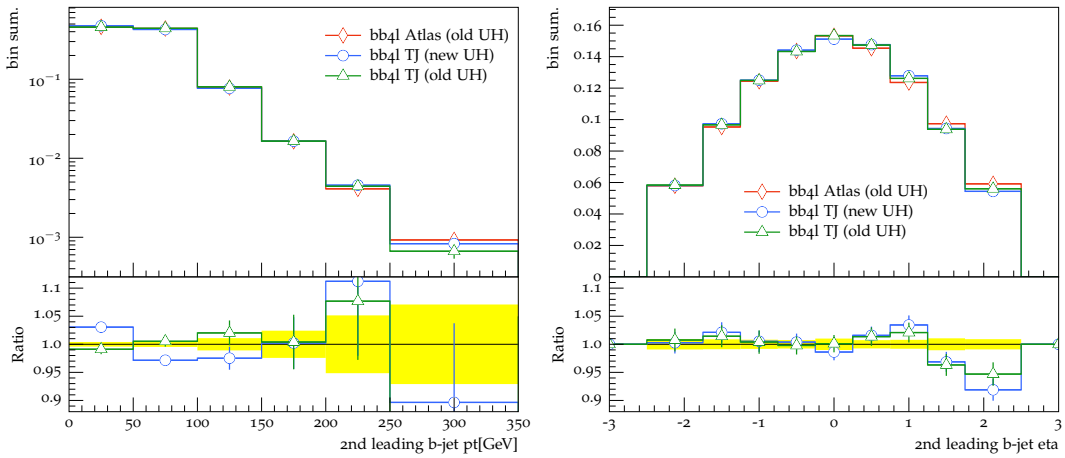

Figure C.8.: The p_T and η distributions of the subleading b-jets. Statistical uncertainties of the ATLAS sample are given as a yellow band.

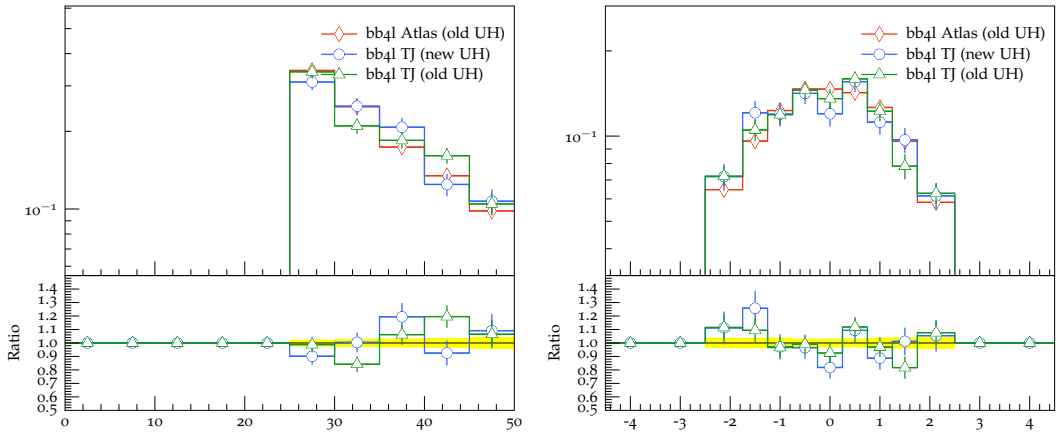

Figure C.9.: The p_T and η distributions of the 3rd-leading b-jets. Statistical uncertainties of the ATLAS sample are given as a yellow band.

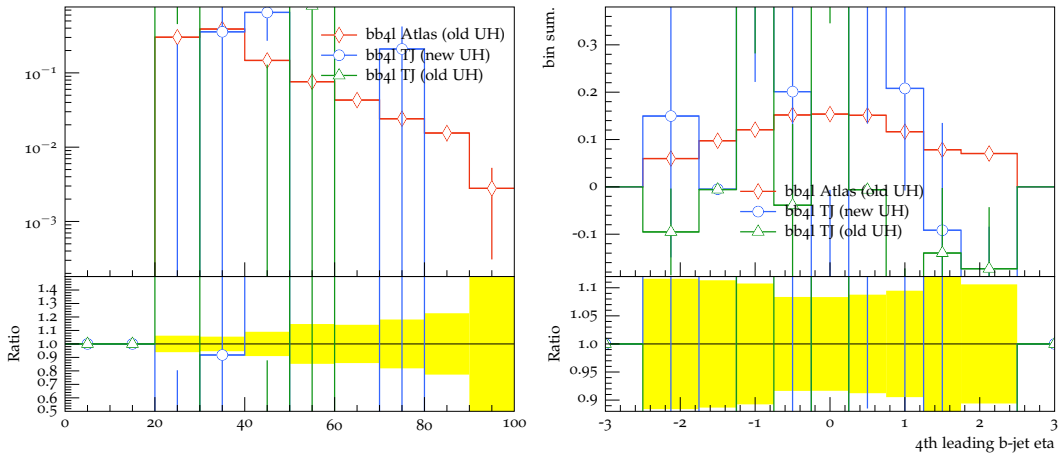

Figure C.10.: The p_T and η distributions of the 4th-leading b-jets. Statistical uncertainties of the ATLAS sample are given as a yellow band.

Bibliography

[1] H. D. Politzer, *Reliable Perturbative Results for Strong Interactions?*, Phys. Rev. Lett. **30** (1973) 1346–1349.

[2] D. J. Gross and F. Wilczek, *Asymptotically Free Gauge Theories. 1*, Phys. Rev. **D8** (1973) 3633–3652.

[3] H. D. Politzer, *Asymptotic Freedom: An Approach to Strong Interactions*, Phys. Rept. **14** (1974) 129–180.

[4] S. L. Glashow, *Partial Symmetries of Weak Interactions*, Nucl. Phys. **22** (1961) 579–588.

[5] S. Weinberg, *A Model of Leptons*, Phys. Rev. Lett. **19** (1967) 1264–1266.

[6] A. Salam, *Weak and Electromagnetic Interactions*, ed. Nobel Symposium No. 8 (Almqvist & Wiksell, Stockholm, 1968).

[7] P. W. Higgs, *Broken Symmetries, Massless Particles and Gauge Fields*, Phys. Lett. **12** (1964) 132–133.

[8] F. Englert and R. Brout, *Broken Symmetry and the Mass of Gauge Vector Mesons*, Phys. Rev. Lett. **13** (1964) 321–322.

[9] J. Joyce, *Finnegans Wake*. Faber and Faber, London, 1939.

[10] N. Cabbibo, *Unitary Symmetry and Leptonic Decays*, Phys. Rev. Lett. **10** (1963) 531–532.

[11] M. Kobayashi and T. Maskawa, *CP Violation in the Renormalizable Theory of Weak Interaction*, Prog. Theor. Phys. **49** (1973) 652–657.

[12] L. Wolfenstein, *Parametrization of the Kobayashi-Maskawa Matrix*, Phys. Rev. Lett. **51** (1983) 1945–1947.

[13] M. Gell-Mann, *A schematic model of baryons and mesons*, Phys. Lett. **8** (1964) 214–215.

[14] G. Zweig, *An SU(3) model for strong interaction symmetry and its breaking*, Developments in the Quark Theory of Hadrons **1** (1961) 22–101.

[15] S. L. Glashow, J. Iliopoulos, and L. Maiani, *Weak Interactions with Lepton-Hadron Symmetry*, Phys. Rev. **D2** (1970) 1285–1292.

[16] J. E. Augustin et al., *Discovery of a Narrow Resonance in e^+e^- Annihilation*, Phys. Rev. Lett. **33** (1974) 1406–1408.

[17] J. J. Aubert et al., *Experimental Observation of a Heavy Particle J*, Phys. Rev. Lett. **33** (1974) 1404–1406.

[18] L. M. Lederman, *The Upsilon Particle*, Scientific American **239** (1978) 72–81.

[19] DØ Collaboration, S. Abachi et al., *Observation of the Top Quark*, Phys. Rev. Lett. **74** (1995) 2632–2637.

[20] CDF Collaboration, F. Abe et al., *Observation of Top Quark Production in $p\bar{p}$ Collisions with the Collider Detector at Fermilab*, Phys. Rev. Lett. **74** (1995) 2626–2631.

[21] B. Pontecorvo, *Inverse beta processes and nonconservation of lepton charge*, Sov. Phys. JETP **7** (1958) 172–173, [Zh. Eksp. Teor. Fiz.34,247(1957)].

[22] Z. Maki, M. Nakagawa, and S. Sakata, *Remarks on the Unified Model of Elementary Particles*, Prog. Theor. Phys. **28** (1962) 870–880.

[23] J. J. Thomson, *Cathode rays*, Phil. Mag. Ser.5 **44** (1897) 293–316.

[24] W. Pauli, *Dear radioactive ladies and gentlemen*, Phys. Today **31N9** (1978) 27.

[25] C. L. Cowan et al., *Detection of the free neutrino: A Confirmation*, Science **124** (1956) 103–104.

[26] C. D. Anderson and S. H. Neddermeyer, *Cloud Chamber Observations of Cosmic Rays at 4300 Meters Elevation and Near Sea-Level*, Phys. Rev. **50** (1936) 263–271.

[27] G. Danby et al., *Observation of High-Energy Neutrino Reactions and the Existence of Two Kinds of Neutrinos*, Phys. Rev. Lett. **9** (1962) 36–44.

[28] M. L. Perl et al., *Evidence for Anomalous Lepton Production in e^+ - e^- Annihilation*, Phys. Rev. Lett. **35** (1975) 1489–1492.

[29] DONUT Collaboration, K. Kodama et al., *Observation of tau neutrino interactions*, Phys. Lett. **B504** (2001) 218–224.

[30] LHCb Collaboration, *Amplitude analysis of $B^+ \to J/\psi\phi K^+$ decays*, Phys. Rev. **D95** (2017) 012002.

[31] LHCb Collaboration, *Observation of $J/\psi p$ Resonances Consistent with Pentaquark States in $\Lambda_b^0 \to J/\psi K^- p$ Decays*, Phys. Rev. Lett. **115** (2015) 072001.

[32] Particle Data Group Collaboration, M. Tanabashi et al., *Review of Particle Physics*, Phys. Rev. **D98** (2018) 030001.

[33] ATLAS Collaboration, *Observation of a new particle in the search for the Standard Model Higgs boson with the ATLAS detector at the LHC*, Phys. Lett. **B716** (2012) 1–29.

[34] CMS Collaboration, *Observation of a new boson at a mass of 125 GeV with the CMS experiment at the LHC*, Phys. Lett. **B716** (2012) 30–61.

[35] M. Goldhaber, L. Grodzins, and A. W. Sunyar, *Helicity of Neutrinos*, Phys. Rev. **109** (1958) 1015–1017.

[36] M. Gell-Mann, P. Ramond, and R. Slansky, *Complex Spinors and Unified Theories*, Conf. Proc. **C790927** (1979) 315–321.

[37] T. Yanagida, *HORIZONTAL SYMMETRY AND MASSES OF NEUTRINOS*, Conf. Proc. **C7902131** (1979) 95–99.

[38] R. N. Mohapatra and G. Senjanovic, *Neutrino Mass and Spontaneous Parity Violation*, Phys. Rev. Lett. **44** (1980) 912–915.

[39] Planck Collaboration, P. A. R. Ade et al., *Planck 2013 results. I. Overview of products and scientific results*, Astron. Astrophys. **571** (2014) A1.

[40] K. C. Freeman, *On the disks of spiral and SO Galaxies*, Astrophys. J. **160** (1970) 811.

[41] R. N. Whitehurst and M. S. Roberts, *High-Velocity Neutral Hydrogen in the Central Region of the Andromeda Galaxy*, Astrophys. J. **175** (1972) 347.

[42] J. Gervais and B. Sakita, *Field Theory Interpretation of Supergauges in Dual Models*, Nucl. Phys. **B34** (1971) 632–639.

[43] Y. A. Golfand and E. P. Likhtman, *Extension of the Algebra of Poincare Group Generators and Violation of p Invariance*, JETP Lett. **13** (1971) 323–326, [Pisma Zh. Eksp. Teor. Fiz.13,452(1971)].

[44] D. V. Volkov and V. P. Akulov, *Possible universal neutrino interaction*, JETP Lett. **16** (1972) 438–440, [Pisma Zh. Eksp. Teor. Fiz.16,621(1972)].

[45] Supernova Search Team Collaboration, A. G. Riess et al., *Observational evidence from supernovae for an accelerating universe and a cosmological constant*, Astron. J. **116** (1998) 1009–1038.

[46] L. Randall and R. Sundrum, *A Large mass hierarchy from a small extra dimension*, Phys. Rev. Lett. **83** (1999) 3370–3373.

[47] L. Randall and R. Sundrum, *An Alternative to compactification*, Phys. Rev. Lett. **83** (1999) 4690–4693.

[48] M. Jezabek and J. H. Kuhn, *QCD Corrections to Semileptonic Decays of Heavy Quarks*, Nucl. Phys. **B314** (1989) 1–6.

[49] ATLAS Collaboration, *Direct top-quark decay width measurement in the $t\bar{t}$ lepton+jets channel at $\sqrt{s}$=8 TeV with the ATLAS experiment*, Eur. Phys. J. **C78** (2018) 129.

[50] I. I. Y. Bigi et al., *Production and Decay Properties of Ultraheavy Quarks*, Phys. Lett. **B181** (1986) 157–163.

[51] N. Collaboration, *Parton distributions for the LHC Run II*, JHEP **04** (2015) 040.

[52] M. Czakon, P. Fiedler, and A. Mitov, *Total Top-Quark Pair-Production Cross Section at Hadron Colliders Through $O(\pm\frac{4}{S})$*, Phys. Rev. Lett. **110** (2013) 252004.

[53] CDF, D0 Collaboration, T. A. Aaltonen et al., *Combination of measurements of the top-quark pair production cross section from the Tevatron Collider*, Phys. Rev. **D89** (2014) 072001.

[54] ATLAS Collaboration, *Measurement of the $t\bar{t}$ production cross-section using $e\mu$ events with b-tagged jets in pp collisions at $\sqrt{s} = 13$ TeV with the ATLAS detector*, Phys. Lett. **B761** (2016) 136–157.

[55] M. Aliev et al., *HATHOR: HAdronic Top and Heavy quarks crOss section calculatoR*, Comput. Phys. Commun. **182** (2011) 1034–1046.

[56] P. Kant et al., *HatHor for single top-quark production: Updated predictions and uncertainty estimates for single top-quark production in hadronic collisions*, Comput. Phys. Commun. **191** (2015) 74–89.

[57] M. Botje et al., *The PDF4LHC Working Group Interim Recommendations*, `arXiv:1101.0538 [hep-ph]`.

[58] A. D. Martin et al., *Uncertainties on alpha(S) in global PDF analyses and implications for predicted hadronic cross sections*, Eur. Phys. J. **C64** (2009) 653–680.

[59] H. Lai et al., *New parton distributions for collider physics*, Phys. Rev. **D82** (2010) 074024.

[60] R. D. Ball et al., *Parton distributions with LHC data*, Nucl. Phys. **B867** (2013) 244–289.

[61] A. D. Martin et al., *Parton distributions for the LHC*, Eur. Phys. J. **C63** (2009) 189–285.

[62] ATLAS Collaboration, *Measurement of the inclusive cross-sections of single top-quark and top-antiquark t-channel production in pp collisions at $\sqrt{s} = 13$ TeV with the ATLAS detector*, JHEP **04** (2017) 086.

[63] ATLAS Collaboration, *Measurement of the cross-section for producing a W boson in association with a single top quark in pp collisions at $\sqrt{s} = 13$ TeV with ATLAS*, JHEP **01** (2018) 063.

[64] ATLAS Collaboration, *Evidence for single top-quark production in the s-channel in proton–proton collisions at $\sqrt{s} = 8$ TeV with the ATLAS detector using the Matrix Element Method*, Phys. Lett. **B756** (2016) 228–246.

[65] CMS Collaboration, *Measurement of the ratio $\mathscr{B}(t \to Wb)/\mathscr{B}(t \to Wq)$ in pp collisions at $\sqrt{s}$ = 8 TeV*, Phys. Lett. **B736** (2014) 33–57.

[66] L. Evans and P. Bryant, *LHC Machine*, JINST **3** (2008) S08001.

[67] ATLAS Collaboration, *The ATLAS Experiment at the CERN Large Hadron Collider*, JINST **3** (2008) S08003.

[68] CMS Collaboration, *The CMS Experiment at the CERN LHC*, JINST **3** (2008) S08004.

[69] ALICE Collaboration, *The ALICE experiment at the CERN LHC*, JINST **3** (2008) S08002.

[70] LHCb Collaboration, *The LHCb Detector at the LHC*, JINST **3** (2008) S08005.

[71] ATLAS Collaboration, *ATLAS Insertable B-Layer Technical Design Report*, Tech. Rep. CERN-LHCC-2010-013. ATLAS-TDR-19, Sep, 2010.

[72] ATLAS IBL Collaboration, *Production and Integration of the ATLAS Insertable B-Layer*, JINST **13** (2018) T05008.

[73] H. Bethe, *Theory of the Passage of Fast Corpuscular Rays Through Matter*, Annalen Phys. **5** (1930) 325–400.

[74] I. Bird et al., *LHC computing Grid: Technical Design Report*. Technical Design Report LCG. CERN, Geneva, 2005.

[75] ATLAS Collaboration Collaboration,, *ATLAS computing: technical design report*. Technical Design Report ATLAS. CERN, Geneva, 2005.

[76] R. Brun and F. Rademakers, *ROOT: An object oriented data analysis framework*, Nucl. Instrum. Meth. **A389** (1997) 81–86.

[77] T. Sjostrand, S. Mrenna, and P. Z. Skands, *PYTHIA 6.4 Physics and Manual*, JHEP **05** (2006) 026.

[78] T. Sjostrand, S. Mrenna, and P. Z. Skands, *A Brief Introduction to PYTHIA 8.1*, Comput. Phys. Commun. **178** (2008) 852–867.

[79] V. V. Sudakov, *Vertex parts at very high-energies in quantum electrodynamics*, Sov. Phys. JETP **3** (1956) 65–71, [Zh. Eksp. Teor. Fiz.30,87(1956)].

[80] G. Altarelli and G. Parisi, *Asymptotic Freedom in Parton Language*, Nucl. Phys. **B126** (1977) 298–318.

[81] V. N. Gribov and L. N. Lipatov, *Deep inelastic e p scattering in perturbation theory*, Sov. J. Nucl. Phys. **15** (1972) 438–450, [Yad. Fiz.15,781(1972)].

[82] Y. L. Dokshitzer, *Calculation of the Structure Functions for Deep Inelastic Scattering and e^+ e^- Annihilation by Perturbation Theory in Quantum Chromodynamics.*, Sov. Phys. JETP **46** (1977) 641–653, [Zh. Eksp. Teor. Fiz.73,1216(1977)].

[83] B. Andersson, et al., *Parton Fragmentation and String Dynamics*, Phys. Rept. **97** (1983) 31–145.

[84] B. Andersson, *The Lund model*, Camb. Monogr. Part. Phys. Nucl. Phys. Cosmol. **7** (1997) 1–471.

[85] G. C. Fox and S. Wolfram, *A Model for Parton Showers in QCD*, Nucl. Phys. **B168** (1980) 285–295.

[86] R. D. Field and S. Wolfram, *A QCD Model for e^+ e^- Annihilation*, Nucl. Phys. **B213** (1983) 65–84.

[87] G. Marchesini et al., *HERWIG: A Monte Carlo event generator for simulating hadron emission reactions with interfering gluons. Version 5.1 - April 1991*, Comput. Phys. Commun. **67** (1992) 465–508.

[88] G. Corcella et al., *HERWIG 6: An Event generator for hadron emission reactions with interfering gluons (including supersymmetric processes)*, JHEP **01** (2001) 010.

[89] T. Sjostrand, *Jet Fragmentation of Nearby Partons*, Nucl. Phys. **B248** (1984) 469–502.

[90] E. Eichten et al., *Charmonium: The model*, Phys. Rev. D **17** (1978) 3090–3117.

[91] E. Eichten et al., *Charmonium: Comparison with experiment*, Phys. Rev. D **21** (1980) 203–233.

[92] D. Amati and G. Veneziano, *Preconfinement as a Property of Perturbative QCD*, Phys. Lett. **83B** (1979) 87–92.

[93] M. Born, *Quantenmechanik der Stoßvorgänge*, Zeitschrift für Physik **38** (1926) 803–827.

[94] R. K. Ellis, D. A. Ross, and A. E. Terrano, *The Perturbative Calculation of Jet Structure in e^+ e^- Annihilation*, Nucl. Phys. **B178** (1981) 421–456.

[95] S. Frixione, P. Nason, and C. Oleari, *Matching NLO QCD computations with Parton Shower simulations: the POWHEG method*, JHEP **11** (2007) 070.

[96] S. Frixione and B. R. Webber, *Matching NLO QCD computations and parton shower simulations*, JHEP **06** (2002) 029.

[97] S. Alioli et al., *A general framework for implementing NLO calculations in shower Monte Carlo programs: the POWHEG BOX*, JHEP **06** (2010) 043.

[98] P. Nason, *A New method for combining NLO QCD with shower Monte Carlo algorithms*, JHEP **11** (2004) 040.

[99] E. Boos et al., *Generic user process interface for event generators*, in *Physics at TeV colliders. Proceedings, Euro Summer School, Les Houches, France, May 21-June 1, 2001*.

[100] T. Jezo and P. Nason, *On the Treatment of Resonances in Next-to-Leading Order Calculations Matched to a Parton Shower*, JHEP **12** (2015) 065.

[101] S. Catani and M. H. Seymour, *A General algorithm for calculating jet cross-sections in NLO QCD*, Nucl. Phys. **B485** (1997) 291–419, [Erratum: Nucl. Phys.B510,503(1998)].

[102] F. Cascioli, P. Maierhofer, and S. Pozzorini, *Scattering Amplitudes with Open Loops*, Phys. Rev. Lett. **108** (2012) 111601.

[103] A. Denner, S. Dittmaier, and L. Hofer, *Collier: a fortran-based Complex One-Loop LIbrary in Extended Regularizations*, Comput. Phys. Commun. **212** (2017) 220–238.

[104] G. Ossola, C. G. Papadopoulos, and R. Pittau, *CutTools: A Program implementing the OPP reduction method to compute one-loop amplitudes*, JHEP **03** (2008) 042.

[105] A. van Hameren, *OneLOop: For the evaluation of one-loop scalar functions*, Comput. Phys. Commun. **182** (2011) 2427–2438.

[106] T. Jezo et al., *An NLO+PS generator for $t\bar{t}$ and Wt production and decay including non-resonant and interference effects*, Eur. Phys. J. **C76** (2016) 691.

[107] S. Frixione, P. Nason, and G. Ridolfi, *A Positive-weight next-to-leading-order Monte Carlo for heavy flavour hadroproduction*, JHEP **09** (2007) 126.

[108] J. M. Campbell et al., *Top-Pair Production and Decay at NLO Matched with Parton Showers*, JHEP **04** (2015) 114.

[109] H. Kahn and T. E. Harris, *Estimation of particle transmission by random sampling.*, Nat. Bur. Stand. Appl. Math. Ser. **12** (1951) 27–30.

[110] A. Buckley et al., *Rivet user manual*, Comput. Phys. Commun. **184** (2013) 2803–2819.

[111] M. Cacciari, G. P. Salam, and G. Soyez, *The Anti-k(t) jet clustering algorithm*, JHEP **04** (2008) 063.

[112] M. Cacciari, G. P. Salam, and G. Soyez, *FastJet User Manual*, Eur. Phys. J. **C72** (2012) 1896.

[113] S. Frixione et al., *Single-top hadroproduction in association with a W boson*, JHEP **07** (2008) 029.

[114] G. Mahlon and S. J. Parke, *Spin Correlation Effects in Top Quark Pair Production at the LHC*, Phys. Rev. **D81** (2010) 074024.

[115] ATLAS Collaboration, *Measurements of top-quark pair spin correlations in the $e\mu$ channel at $\sqrt{s} = 13$ TeV using pp collisions in the ATLAS detector*, Tech. Rep. ATLAS-CONF-2018-027, CERN, Geneva, Jul, 2018.

[116] ATLAS Collaboration, *Probing the quantum interference between singly and doubly resonant top-quark production in pp collisions at $\sqrt{s} = 13$ TeV with the ATLAS detector*, `arXiv:1806.04667 [hep-ex]`.

Acknowledgements

First of all, I want to thank Prof. Dr. Arnulf Quadt for giving me the chance to write my master's thesis in his group and for being my first referee. If it wasn't for him, I wouldn't have had the chance to work on this very exciting topic for a full year and to get to know all the people from all over the world, who were involved in this. Even though this project did not entirely worked out as it was planned in the beginning, I learned many new things and gained valuable experiences. I also want to thank Prof. Dr. Stan Lai for agreeing to be my second referee.

I also want to thank Dr. Royer Ticse-Torres for working with me on a day-to-day basis and answering all the questions I had during the past year, as well as proofreading this thesis. Moreover, I want to thank Tomas Dado, Dr. Clara Nellist and Dr. Thomas Peiffer for proofreading this thesis.

Finally, I want to thank everyone from the II. institute of physics, especially the local top-group, and everyone else in ATLAS, who was involved in this project during the last year, for all their advice and help.

Erklärung nach §17(9) der Prüfungsordnung für den Bachelor-Studiengang Physik und den Master-Studiengang Physik an der Universität Göttingen:

Hiermit erkläre ich, dass ich diese Abschlussarbeit selbständig verfasst habe, keine anderen als die angegebenen Quellen und Hilfsmittel benutzt habe und alle Stellen, die wörtlich oder sinngemäß aus veröffentlichten Schriften entnommen wurden, als solche kenntlich gemacht habe.
Darüberhinaus erkläre ich, dass diese Abschlussarbeit nicht, auch nicht auszugsweise, im Rahmen einer nichtbestandenen Prüfung an dieser oder einer anderen Hochschule eingereicht wurde.

Göttingen, den 28. November 2018

(Marcel Niemeyer)